Effects of Lower Drying-Storage Temperatures on the DBTT of High-Burnup PWR Cladding

Fuel Cycle Research & Development

Prepared for
U.S. Department of Energy
Used Fuel Disposition Campaign

M.C. Billone, T.A. Burtseva, and
M.A. Martin-Rengel

Argonne National Laboratory

August 28, 2015
FCRD-UFD-2015-000008
ANL-15/21

About Argonne National Laboratory
Argonne is a U.S. Department of Energy laboratory managed by UChicago Argonne, LLC under contract DE-AC02-06CH11357. The Laboratory's main facility is outside Chicago, at 9700 South Cass Avenue, Argonne, Illinois 60439. For information about Argonne and its pioneering science and technology programs, see www.anl.gov.

DOCUMENT AVAILABILITY

Online Access: U.S. Department of Energy (DOE) reports produced after 1991 and a growing number of pre-1991 documents are available free via DOE's SciTech Connect (http://www.osti.gov/scitech/)

Reports not in digital format may be purchased by the public from the National Technical Information Service (NTIS):
U.S. Department of Commerce
National Technical Information Service
5301 Shawnee Road
Alexandria, VA 22312
www.ntis.gov
Phone: (800) 553-NTIS (6847) or (703) 605-6000
Fax: (703) 605-6900
Email: **orders@ntis.gov**

Reports not in digital format are available to DOE and DOE contractors from the Office of Scientific and Technical Information (OSTI):
U.S. Department of Energy
Office of Scientific and Technical Information
P.O. Box 62
Oak Ridge, TN 37831-0062
www.osti.gov
Phone: (865) 576-8401
Fax: (865) 576-5728
Email: **reports@osti.gov**

Disclaimer
This report was prepared as an account of work sponsored by an agency of the United States Government. Neither the United States Government nor any agency thereof, nor UChicago Argonne, LLC, nor any of their employees or officers, makes any warranty, express or implied, or assumes any legal liability or responsibility for the accuracy, completeness, or usefulness of any information, apparatus, product, or process disclosed, or represents that its use would not infringe privately owned rights. Reference herein to any specific commercial product, process, or service by trade name, trademark, manufacturer, or otherwise, does not necessarily constitute or imply its endorsement, recommendation, or favoring by the United States Government or any agency thereof. The views and opinions of document authors expressed herein do not necessarily state or reflect those of the United States Government or any agency thereof, Argonne National Laboratory, or UChicago Argonne, LLC.

Reviewed by:

Signature on file

Hanchung Tsai
(Argonne National Laboratory)
Technical Reviewer

Submitted by:

billone

Digitally signed by billone
DN: cn=billone
Date: 2015.09.10 10:40:23 -05'00'

Michael C. Billone
(Argonne National Laboratory)
Work Package Manager

Page intentionally blank

Executive Summary

The purpose of this research effort is to determine the effects of canister and/or cask drying and storage on radial hydride precipitation in, and potential embrittlement of, high-burnup (HBU) pressurized water reactor (PWR) cladding alloys during cooling for a range of peak drying-storage temperatures and hoop stresses. Extensive precipitation of radial hydrides could lower the failure hoop stresses and strains, relative to limits established for as-irradiated cladding from discharged fuel rods stored in pools, at temperatures below the ductile-to-brittle transition temperature (DBTT).

The HBU PWR cladding alloys have a wide range of hydrogen contents and varying hydride morphology after in-reactor service. Radial hydrides are a potential embrittlement mechanism for HBU cladding subjected to hoop-stress loading, which may occur during post-storage cask transport. Ring compression tests (RCTs), which simulate pinch-type loading at grid spacers, are used to determine cladding ductility as a function of RCT temperature and the DBTT. Previous tests were conducted with pressurized and sealed cladding rodlets heated to 400°C (the NRC ISG-11, Rev. 3, limit for all fuel burnups under normal conditions of storage and short-term loading operations) and cooled slowly at 5°C/h. Following this drying-storage simulation, the DBTT was determined as a function of the peak hoop stress at 400°C for HBU PWR cladding alloys: M5®, ZIRLO™, and Zircaloy-4 (Zry-4). The results of previous tests indicated that radial-hydride-induced embrittlement was insignificant (i.e., DBTT <25°C) for peak hoop stresses ≤90 MPa even with temperature cycling, but it was potentially significant for hoop stresses ≥110 MPa. Baseline properties tests with as-irradiated cladding from HBU fuel rods also indicated that Zry-4 with >600 wppm hydrogen could be embrittled due to high concentrations of circumferential hydrides extending from the outer surface into >50% of the cladding wall. For a range of RCT displacement rates (0.05 mm/s to 50 mm/s) and test temperatures (20°C to 90°C), offset strains were 1.7±0.5% (5 data points), which are lower than the 2% offset-strain ductility limit.

Six RCT tests with as-irradiated HBU Zry-4 were conducted during the current work at 20°C to 120°C. Two tests were intentionally interrupted after load drops of about 23%, the permanent changes in diameters were measured directly, and metallographic examination was used to confirm relatively benign cracking extending through <50% of the cladding wall. The corresponding permanent strains were 2.1% and 2.7%, which are greater than the 1% permanent-strain ductility limit. These data allowed re-interpretation of all 11 load-displacement curves to give 2.8±0.7% offset strain, which imply ductility for the range of conditions tested. Load-displacement curves and images of crack progression indicated relatively benign cracking of circumferential hydrides followed by plastic flow and failure of Zry-4 between the circumferential hydrides.

On the basis of current best-estimate thermal calculations, it appears that cladding temperatures may not exceed 350°C during vacuum drying and storage. For cladding alloys with high hydrogen content (350 to 650 wppm), the dissolved hydrogen available to precipitate as radial hydrides decreases by 80 wppm with a decrease in peak temperature from 400°C to 350°C. Also, there would be decreases in the temperature, internal pressure, and hoop stress at which radial-hydride precipitation would initiate. A 3-cycle drying test was conducted in Fiscal Year 2014 at 350°C peak temperature with HBU ZIRLO™ and at a peak hoop stress of 93 MPa, (equivalent to ≈100 MPa at 400°C). Metallographic examination conducted for the 3-cycle rodlet subjected to intermediate cooling from 350°C to 250°C revealed significant radial hydride precipitation. RCTs conducted during the current work confirmed expectations that such radial hydrides would increase the DBTT to about 120°C. Thus, these test conditions resulted in a significantly higher DBTT than obtained for 1- and 3-cycle tests conducted at peak conditions of about ≈90 MPa at 400°C.

Two factors were considered to rationalize the results obtained from the 3-cycle test at 350°C/93-MPa peak conditions: the slightly higher peak hoop stress and the possible increase in radial-hydride precipitation due to cycling. The test was repeated using 1-cycle heating-cooling and the same peak conditions. Following cooling, radial hydrides were observed to be as long as observed in the sample subjected to 3-cycle cooling, and the RCT ductility values were comparable within data scatter. The eight ductility data points from the two tests were combined to determine a DBTT of 125±5°C vs. 23°C for peak drying-storage conditions of 90 MPa at 400°C. These results indicate: (a) the DBTT for HBU ZIRLO™ exhibits a high sensitivity to the peak drying-storage hoop stress; (b) the DBTT was insensitive to the 50°C decrease in peak drying-storage temperature; and (c) the data scatter observed indicates the need for repeat testing including load-interrupt tests to determine the DBTT with more certainty.

Although these test results are useful and interesting, they cannot be used directly to determine whether or not fuel rods will maintain integrity during normal conditions of post-storage transport. This requires an integrated effort, which is in progress within the UFD Campaign, to determine the: (a) distribution of rod internal pressures for discharged HBU fuel rods; (b) temperature history for the plenum region where most of the gas resides; (c) distribution of fuel rods with peak hoop stress values <90 MPa and ≥90 MPa during drying and storage; (d) conversion of RCT loads and displacements to hoop failure stresses and strains; and (e) axial and hoop loads during normal conditions of transport.

CONTENTS

FIGURES

TABLES

ACRONYMS, UNITS AND SYMBOLS

ACRONYMS

ANL	Argonne National Laboratory (Argonne)
CWSRA	cold-worked, stress-relief annealed
DBTT	ductile-to-brittle transition temperature
DOE	U.S. Department of Energy
EPRI	Electric Power Research Institute
ESCP	Extended Storage Collaboration Program
HBU	high burnup
ID	inner diameter surface
ISG	Interim Staff Guidance
NRC	Nuclear Regulatory Commission
OD	outer diameter surface
PWR	pressurized water reactor
RCT	ring compression test
RHCF	radial hydride continuity factor (in %)
RHT	radial-hydride treatment
RT	room temperature
RXA	recrystallized-annealed
TMT	thermo-mechanical treatment
Zry-2	Zircaloy-2
Zry-4	Zircaloy-4

UNITS

°C	degree Celsius
GWd/MTU	giga-watt-days per metric tonne of uranium
h	hour
kN	kilo-Newton
m	meter
mm	millimeter
µm	micron
MPa	mega-Pascal
N	Newton
s	second
wppm	weight parts per million

SYMBOLS

C_H	hydrogen content in weight parts per million (wppm)
C_{HD}	dissolved hydrogen in wppm
C_{HP}	amount of dissolved hydrogen needed to initiate hydride precipitation (in wppm)
D_{mi}	inner diameter of cladding alloy
D_{mo}	outer diameter of cladding alloy
D_o	cladding outer diameter (includes outer-surface corrosion layer if present)
d_p	permanent displacement (pre-test diameter minus post-test diameter in loading direction)
d_p/D_{mo}	RCT permanent strain (%)
δ	controlled and measured RCT displacement at the 12 o'clock sample position
δ_{max}	maximum RCT displacement at the 12 o'clock sample position
Δp	pressure difference across cladding wall ($p_i - p_o$)
ΔP	load drop from crack initiation load (P_i) to minimum load for ductility measure (P_d)
δ_p	RCT offset displacement at 12 o'clock position relative to static support at 6 o'clock
δ_p/D_{mo}	RCT offset strain (%)
ΔT	temperature drop per drying cycle
ΔT_{PD}	difference between hydride precipitation (T_P) and dissolution (T_D) temperatures
$(\varepsilon_\theta)_{max}$	maximum hoop strain
h_m	cladding metal wall thickness
h_{ox}	thickness of outer surface corrosion (oxide) layer
K_{LC}	calculated linearized loading slope (also known as loading stiffness) for RCT samples
K_{LM}	measured linearized loading slope
K_U	calculated linearized unloading slope
K_{UM}	measured linearized unloading slope
L	length of RCT samples
M_{max}	maximum RCT bending moment
P	measured RCT load at the 12 o'clock sample orientation
p_i	internal gas pressure
P_d	minimum load for ductility determination
P_i	peak load at crack initiation
P_{max}	maximum RCT load
p_o	external gas pressure
R_{mi}	inner radius of cladding alloy
σ_θ	hoop stress
T	temperature
T_{max}	maximum hold temperature for RHT
T_D	hydrogen dissolution temperature
T_h	hold temperature for RHT
T_P	hydrogen precipitation temperature

1. INTRODUCTION

Structural analyses of high-burnup (HBU) fuel rods require cladding mechanical properties and failure limits to assess fuel behavior during long-term dry-cask storage, post-storage retrieval and transportation, and post-transport retrieval. License applications for transport casks containing HBU fuel assemblies have used properties and failure limits for as-irradiated cladding [1]. The Zircaloy-4 (Zry-4) properties and limits in Ref. 1 were based primarily on axial-tensile and pressurized tube tests. Isotropic correlations were developed for stress vs. strain and failure limits. However, pre-storage drying-transfer operations and early stage storage subject cladding to higher tensile hoop stresses induced by higher temperatures and pressures relative to in-reactor operation and pool storage. Under these conditions, radial hydrides may precipitate during slow cooling and may introduce an embrittlement mechanism if the cladding temperature decreases below a critical point, which is defined as the ductile-to-brittle transition temperature (DBTT). If embrittlement is predicted to occur in response to hoop-stress loading, then cladding failure criteria would have to be revised to account for this effect.

In Interim Staff Guidance-11, Revision 3 (ISG-11, Rev. 3), the Nuclear Regulatory Commission (NRC) recommends a peak cladding temperature limit of 400°C for all fuel burnups under normal conditions of storage and short-term loading operations (e.g., drying, backfilling with inert gas, and transferring the cask to the storage pad) [2]. During loading operations, repeated thermal cycling (repeated heat-up/cool-down cycles) may occur but should be limited to fewer than 10 cycles, with cladding temperature variations that are less than 65°C each, according to ISG-11, Rev. 3 (see Fig. 1 at the end of this section for justification of <65°C per cycle). One concern for HBU fuel cladding is the possible precipitation of radial hydrides, which could embrittle cladding in response to tensile hoop stresses caused by internal pressure loading and “pinch-type” loading during transport. Limits established in ISG-11, Rev. 3, relied on data available before 2002, which were primarily for low-burnup and non-irradiated/pre-hydrided Zry-4. At the time ISG-11, Rev. 3, was issued (2003), NRC recognized that data for HBU fuel cladding alloys were needed to determine the extent of radial-hydride embrittlement under conditions relevant to drying-transfer operations and storage. One concern was, and still is, whether or not HBU fuel will maintain cladding integrity and be readily retrievable after more than 20 years of storage, at which time the peak cladding temperatures would be ≈200°C or less.

Argonne National Laboratory has developed a test protocol for studying HBU cladding embrittlement that has been used to generate data for NRC. Experimentally, the protocol involves two steps: (a) radial-hydride treatment (RHT), during which HBU cladding is exposed to simulated drying-storage temperature and hoop stress conditions, including slow cooling with decreasing stress, followed by (b) ring compression testing, in which rings sectioned from RHT HBU cladding are compressed to determine strength and ductility as a function of the test temperature. The ring compression test (RCT) is used as a ductility screening test, and the RCT loading simulates the pinch-type loading on HBU cladding that occurs during normal cask transport and possible drop accidents. The protocol was used to generate DBTT data for HBU ZIRLO™ and Zry-4 [3, 4] (both efforts sponsored by NRC) and HBU M5® [sponsored by the U.S. Department of Energy (DOE)] [5]. Under DOE-sponsored research, Argonne has also generated baseline characterization data and data for the strength and ductility of as-irradiated Zry-4, ZIRLO™, and M5®. These data are important not only for determining the potentially degrading effects of drying and early stage storage, but also for serving as reference properties for future evaluations of the effects of drying storage on these cladding alloys [6–8]. Reference 9 includes Argonne data generated through September 30, 2013, including additional DOE-sponsored test results for HBU ZIRLO™ and M5® following cooling from 400°C and lower hoop stress levels (80 to 90 MPa). Reference 10 contains refined interpretations of previously generated data, as well as new test results for HBU ZIRLO™ subjected to 3-cycle drying at peak drying-storage conditions of 93 MPa and 350°C.

In addition to the Argonne data sets for PWR cladding alloys, Aomi et al. [11] have generated data for Zircaloy-2 (Zry-2) and Zry-4 using test methods similar to the ones developed by Argonne. However, RHT samples were cooled under constant stress (vs. decreasing stress, as used by Argonne), and RCTs were conducted only at room temperature (RT) and at a very slow displacement rate (0.033 mm/s vs. 5 mm/s used by Argonne). Their results are both revealing and relevant in evaluating the effects of hydrogen content (C_H) and thermo-mechanical treatment (TMT) on the susceptibility of cladding alloys to radial-hydride formation. Argonne and Aomi et al. test results indicate that susceptibility to radial-hydride precipitation during cooling is dependent on cladding alloy, TMT, total C_H, C_H below the hydride rim, and peak RHT temperature and hoop stress. The combination of recrystallized-annealed (RXA) microstructure and low C_H (above the inner liner for Zry-2) makes Zry-2 and M5® more susceptible to precipitation of long radial hydrides during cooling. For cold-worked, stress-relief-annealed (CWSRA) alloys, ZIRLO™ was found by Argonne to be more susceptible to radial-hydride precipitation than Zry-4. The differences in the distribution of hydrides across the cladding wall (lower for ZIRLO™ below the hydride rim) may be partly responsible for this behavior [4].

Section 2 of this report describes the materials and test methods used in this program. It has been updated from what was presented in Ref. 10 with regard to test materials relevant to the current work and failure criteria for cladding with only circumferential hydrides. Previous test results for Zry-4 and ZIRLO™ are summarized in Section 3 for materials in the as-irradiated condition and following RHT at 400°C.

Results of current best-estimate thermal analyses indicate that peak cladding temperatures may not exceed 350°C during vacuum drying and storage for canisters and/or casks containing HBU fuel assemblies [12]. Starting with the 3-cycle/350°C RHT conducted in Fiscal Year 2014, the emphasis of current testing has been on peak RHT temperatures ≤350°C. It is also desirable to conduct tests within a relevant RHT hoop stress range. As the database for end-of-life (EOL) rod internal pressures (RIPs) is insufficient to determine this range, RHT hoop stresses for testing remain at 80 MPa to 110 MPa. Efforts to improve this database are described in Section 5.

New test results for HBU Zry-4 and HBU ZIRLO™ are presented in Section 4. RCTs were conducted using as-irradiated Zry-4 with about 620 wppm hydrogen and compared to results previously obtained for Zry-4 with about 640 wppm hydrogen. On the basis of load-interrupt tests followed by metallographic examination, new criteria were developed to distinguish cracking in samples with circumferential hydrides vs. established criteria for samples with both circumferential and radial hydrides. For ZIRLO™ new RCTs results are presented for the rodlet subjected to 3-cycle drying (100°C temperature drop per cycle) at 350°C/92-MPa peak (target) RHT conditions. To distinguish the effects of reduced temperature, increased stress, and temperature cycling, an additional 1-cycle test was conducted at 350°C/92-MPa peak (target) RHT conditions.

To appreciate the influence of peak RHT temperature (i.e., decrease from 400°C to 350°C), stress, temperature cycling, and hydrogen content on radial hydride precipitation and embrittlement, it is important to review literature results for hydrogen dissolution and hydride precipitation. Unlike most, if not all, studies of radial hydride precipitation and subsequent ductility, the Argonne RHT process includes decreasing internal gas pressure and hoop stress with decreasing temperature during cooling, as would occur in actual fuel rods. Other researchers have used an open, actively pressurized cladding tube for which the pressure is kept constant during cooling. As such, it is important to understand the dependence of hydrogen solubility (C_{HD}) on temperature (T_D) during the heating phase and the initiation of hydrogen precipitation (C_{HP} at T_P) during the cooling phase. Figure 1 summarizes the data of Kearns [13], Kammenzind et al. [14], and McMinn et al. [15] for these parameters, as well as the temperature gap (ΔT_{PD}) between precipitation and dissolution. The results in Fig. 1 are used in Sections 3 and 4 to determine the cladding temperature and stress at which precipitation, especially radial hydride precipitation, can initiate. In particular, the solubility of hydrogen at 400°C is 206±5 wppm and the precipitation temperature is 335°C. The hydrogen solubility at 350°C is 126±6 wppm and the precipitation temperature is 285°C.

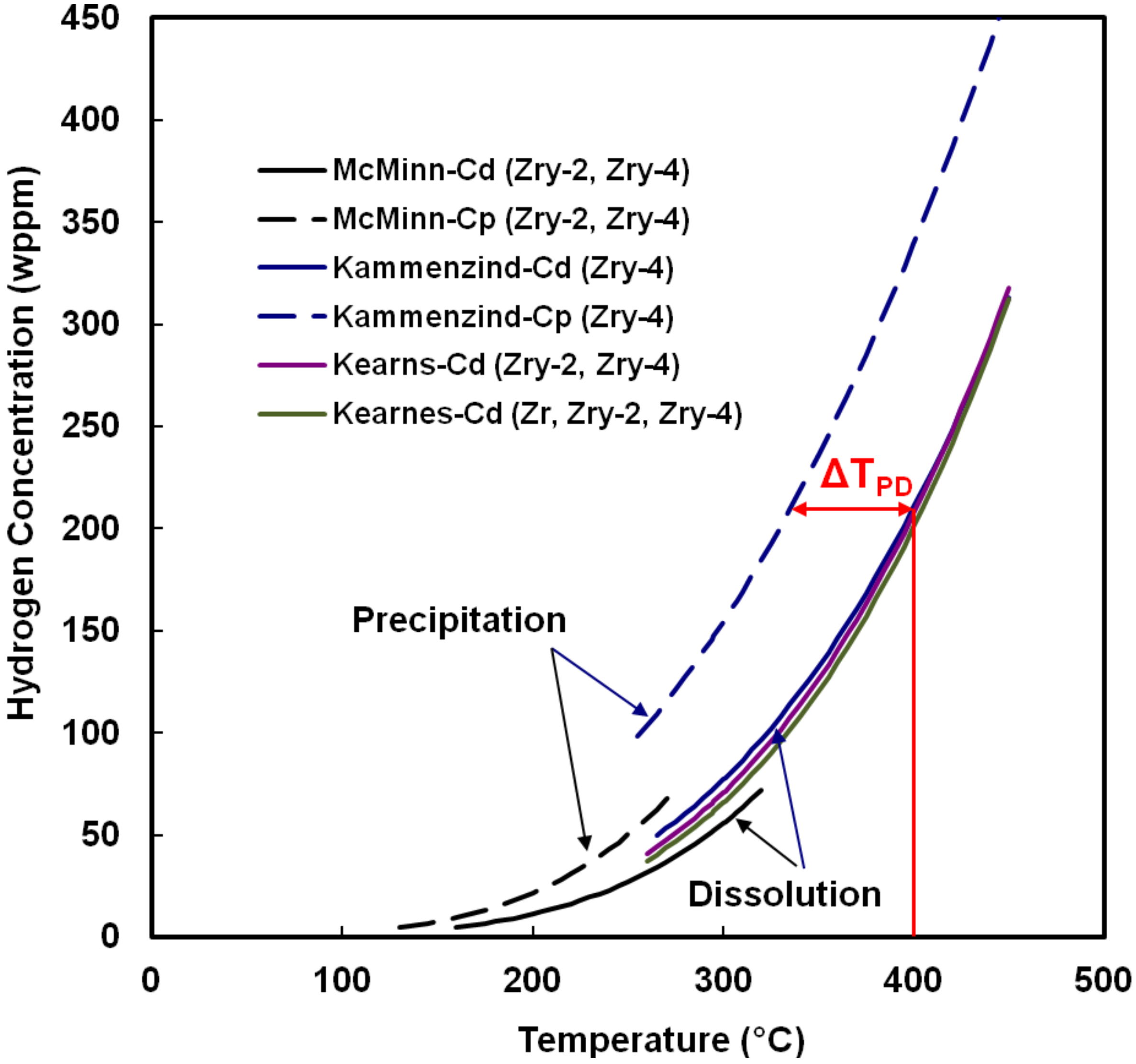

Figure 1: Steady-state curves for hydrogen dissolution and precipitation in Zr alloys.

Page intentionally blank

2. HBU CLADDING MATERIALS AND TEST METHODS

2.1 HBU CLADDING MATERIALS

References 9 and 10 contain detailed lists of defueled cladding materials used in previous testing. Relevant materials for the current work are listed in Table 1. The materials came from fuel rods irradiated to HBU in commercial light water reactors. The Zry-4 cladding segments listed at 67 GWd/MTU were from two fuel rods irradiated in the same assembly in one of the H.B. Robinson reactors. ZIRLO™ cladding segments came from a fuel rod irradiated in the North Anna Units 1 and 2 reactors. The $\pm C_H$ values represent one-sigma variations in data collected from multiple axial locations along each segment and quarter-ring samples at each axial location. In general, the large one-sigma values were due to circumferential variation in C_H, especially for average C_H values ≥350 wppm. Additional characterization results are presented in subsequent sections.

Table 1 Summary of HBU Zry-4 and ZIRLO™ cladding materials used in studies of cladding ductility following reactor discharge and following simulated drying and storage (RHT) at peak RHT temperature (T_{max}).

Cladding Alloy	TMT	Burnup, GWd/MTU	Hydrogen Content, wppm	Peak RHT Stress, MPa	Peak RHT T_{max}, °C	Number of Drying Cycles
Zry-4	RXA	67	640±140	–	–	–
		67	616±78	–	–	–
ZIRLO™	CWSRA	68	530±100	89	400	1
		68	480±131	88	400	3
		68	564±177	93	350	3
		68	644±172	94	350	1

2.2 TEST PROTOCOL

The protocol for single-cycle heating-cooling tests consisted of two steps: (a) simulated drying and storage testing (called "RHT") during which a sealed, pressurized rodlet is heated to and stabilized at 400°C within one hour, held at 400°C for one hour, cooled slowly at 5°C/h to 200°C (135°C for low-C_H M5®), and cooled at a higher rate to RT and (b) ring-compression testing at three to four temperatures from RT to 200°C and at 5 mm/s (reference value) displacement rate to a maximum displacement of 1.7 mm. For three-cycle heating-cooling RHTs, rodlets were heated to peak temperatures of 400°C or 350°C, held at T_{max} for one hour, cooled at 5°C/h to 100°C below T_{max}, reheated to T_{max}, held at T_{max} for one hour, cooled at 5°C/h to 100°C below T_{max}, reheated to T_{max}, held at T_{max} for one hour, and then cooled at the same rates used for the single-cycle tests.

HBU cladding segments were used to fabricate sealed and pressurized (with argon) rodlets. Details of rodlet fabrication are given in Ref. 10.

Prior to rodlet pressurization, the outer diameter was measured for each corroded segment at two orientations (90° apart) and at three axial locations. These values were averaged to give the cladding outer diameter (D_o). The thickness of the corrosion (oxide) layer (h_{ox}) was estimated from sibling rod data or from interpolation and extrapolation of data from the same rod at different axial locations. The same approach was used to estimate the cladding metal wall thickness (h_m). The outer diameter of the cladding alloy (D_{mo}) was calculated from $D_o - 2\ h_{ox}$, and the metal inner diameter (D_{mi}) was calculated from $D_{mo} - 2\ h_m$. The ratio R_{mi}/h_m, where R_{mi} is the metal inner radius, was used in Eq. 1 to calculate the average hoop stress (σ_θ) from the pressure difference ($\Delta p = p_i - p_o$) across the cladding wall, where p_o was 0.1 MPa during RT (23°C) fabrication and 0.17 MPa in the RHT furnace.

$$\sigma_\theta = (R_{mi}/h_m)\ \Delta p - p_o \qquad (1)$$

The ideal gas law was used to relate the absolute pressure at the RHT hold temperature (T_h) to the RT pressure according to $p_i(T_h) = ([T_h + 273\ K]/296\ K)\ p_i(23°C)$. Given the target σ_θ value at T_h, the fabricated RT pressure can be calculated using Eq. 1 and the information given above.

Following RHT, the rodlet was depressurized and sectioned for C_H samples, RCT samples, and metallographic imaging samples, which allowed precise determination of the geometrical factors in Eq. 1. Using this procedure, the calculated peak rodlet stress was within 3 MPa of the target value.

The second phase of the test protocol consisted of RCTs. Figure 2 shows a schematic of RCT loading. The RCT load induces maximum hoop bending stresses (σ_θ) at the inner surfaces of the 12 (under load) and 6 (above support) o'clock positions. Tensile hoop stresses also occur at the 3 and 9 o'clock outer surfaces. Associated with these maximum tensile stresses are maximum tensile strains (ε_θ). Within the elastic range, these hoop stresses at 3 and 9 o'clock are about 60% of the maximum stresses at 12 and 6 o'clock. Also, because the length ($L \approx 8$ mm) of the rings is much greater than the cladding wall thickness ($h_m = 0.54$ to 0.56 mm for HBU ZIRLO™ and 0.70 to 0.75 mm for HBU Zry-4), an axial stress is induced that is 0.37 times the hoop stress within the elastic deformation regime. The maximum displacement (1.7 mm) was chosen to give ≈10% offset strain at RT. The reference displacement rate was 5 mm/s.

Load-displacement curves and post-test examinations were used to determine offset displacements (δ_p) and permanent displacements (d_p), respectively. These were normalized to D_{mo} to give relative plastic displacement (i.e., plastic strain) for the ring structure. Permanent displacement is defined as the difference between pre- and post-test diameter measurements along the loading direction. Figure 3 shows how traditional and corrected offset displacements were determined from a benchmark load-displacement curve for a non-irradiated M5® ring. For the benchmark sample, $D_{mo} = 9.50$ mm, $h_m = 0.61$ mm, and $L = 8.00$ mm. The traditional offset methodology calls for unloading the sample at the same slope as the measured loading slope (K_{LM}). It should be noted that this slope is less than the calculated sample stiffness (K_{LC}) due to the influence of machine compliance. This approach gave a traditional $\delta_p = 0.94$ mm, which is greater than the more accurate $d_p = 0.83$ mm. Thus, there is an inherent error in the traditional approach as the measured unloading slope ($K_{UM} = 0.81$ kN/mm) is always less than the measured loading slope. K_{UM} was determined from the slope of the line connecting the maximum displacement to the displacement axis value based on the measured value of d_p at zero load. Normalizing these displacements to D_{mo} gives 9.9% traditional offset strain and 8.7% permanent strain, which is also called the "corrected offset strain."

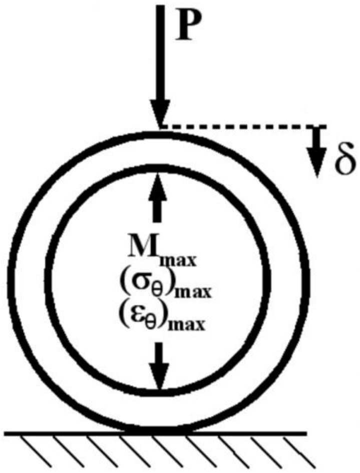

Figure 2: RCT measured load (P) and controlled displacement (δ).

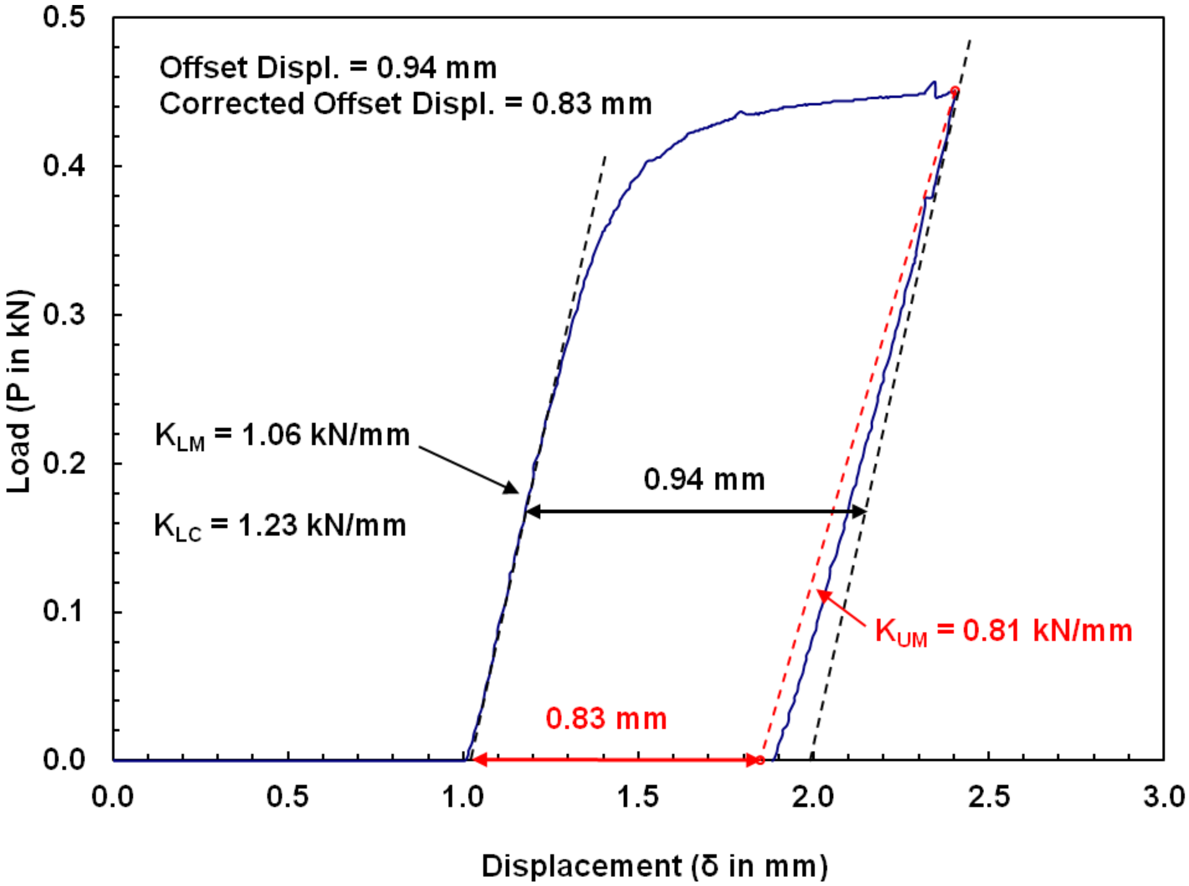

Figure 3: Load-displacement curve for non-irradiated M5® ring tested at RT and 5 mm/s to 1.7 mm displacement.

For HBU cladding rings that crack during the 1.7-mm displacement, d_p cannot be determined accurately. Thus, one must rely on a correlation for the unloading slope to determine the corrected offset displacement prior to the first significant crack, from which the ductility can be determined. The correlation developed for this application is based on the results from a large number of benchmark tests with permanent displacements ranging from 0.14 mm to 1.2 mm. Results of these benchmark tests are shown in Fig. 4 in terms of the ratio of measured unloading/loading (K_{UM}/K_{LM}) slopes vs. traditional offset strain (δ_p/D_{mo}). Also shown in Fig. 4 are results from HBU M5® cladding samples (solid red circles) that exhibited no cracking after 1.7 mm of total displacement. Five benchmark tests have been conducted following the generation of data shown in Ref. 10. These data for as-fabricated M5® are shown as open black triangles in Fig. 4. The new data fall within the scatter band for the primary data set.

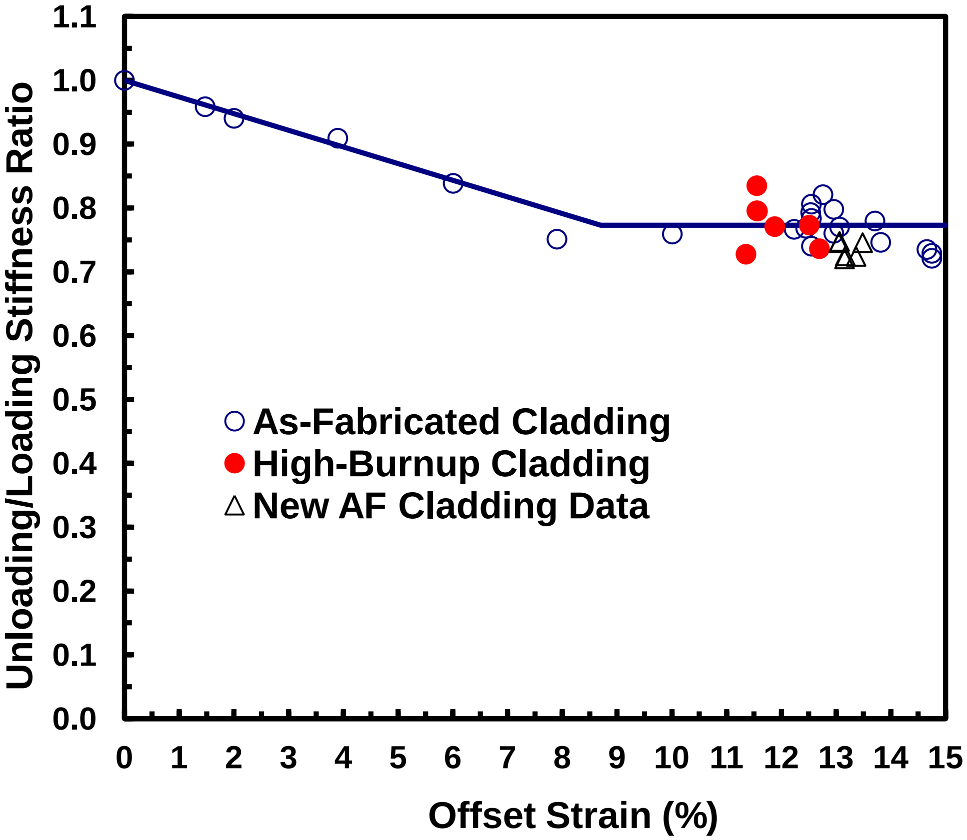

Figure 4: RCT benchmark results for determining the ratio of unloading/loading stiffness as a function of the traditional offset strain.

The correlation for calculating the unloading slope (K_U in kN/mm) as a function of the measured loading slope (in kN/mm) and the measured traditional offset strain (in %) is given by:

$$K_U/K_{LM} = 1 - 0.02612\ \delta_p/D_{mo} \text{ for } \delta_p/D_{mo} \leq 8.7\% \quad (2a)$$

$$K_U/K_{LM} = 0.773 \text{ for } \delta_p/D_{mo} > 8.7\% \quad (2b)$$

The one-sigma variation for the 0.773 high-strain ratio is 0.031.

The criteria for determining embrittlement remain the same for cladding with radial and circumferential hydrides: corrected δ_p/D_{mo} <2% prior to >25% load drop or >50% decrease in loading slope. In previous works [4–7], it was established that >25% load drop and >50% decrease in loading slope correspond to a crack or cracks extending through >50% of the wall thickness. The 2% offset strain limit is based on the uncertainty in measurement of the permanent strain (d_p/D_{mo} ≤1%) for as-fabricated cladding and the added uncertainty (≤1%) in the permanent displacement for HBU cladding due to flaking off of the corrosion (i.e., oxide) layer under the applied load and above the support plate.

The criteria established for determining ductility from load-displacement curves works reasonably well for materials with a smooth rise to a peak load followed by an abrupt load drop caused by rapid crack growth along continuous radial and circumferential hydrides, as is shown in Fig. 5 for HBU Zry-4 following RHT. However, it was found to be too conservative for as-irradiated HBU Zry-4 with a high hydrogen content. All hydrides were circumferentially oriented, densely packed at the oxide-metal interface, and spaced progressively sparser through the cladding wall. Load-displacement curves were characterized by sequences of small load drops followed by plastic flow and cracking of the metal matrix between the cracked circumferential hydrides (see Fig. 5). Both samples shown in Fig. 5 would be classified as brittle if they were mathematically unloaded at the displacement corresponding to the peak load. Special techniques were developed to determine the permanent displacement prior to 50%-wall cracking for as-irradiated Zry-4: (a) load removal after 20% to 30% total load drop, (b) direct measurement of the permanent displacement and strain, and (c) metallographic examination to determine the extent of wall cracking. This procedure is used in Section 4 to determine the permanent strain for new and previous test data.

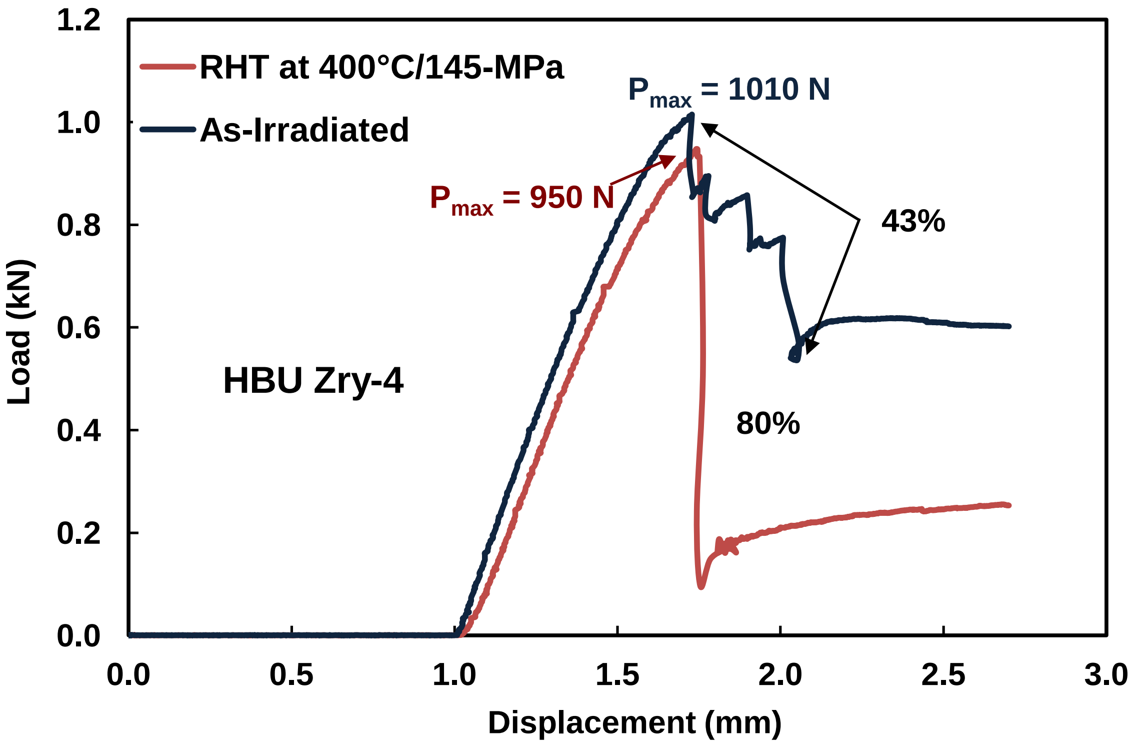

Figure 5: RT Load-displacement curves for HBU Zry in the as-irradiated condition and following RHT at 400°C and 145 MPa peak conditions.

Page intentionally blank

3. PREVIOUS RESULTS FOR HBU ZRY-4 AND HBU ZIRLO™

3.1 HBU ZRY-4

Figure 6 summarizes data previously generated for HBU Zry-4 in the as-irradiated condition and following RHT at peak conditions of 400°C and hoop stresses of 114 MPa and 145 MPa. Following RHT at 400°C, relatively short radial hydrides precipitated during slow cooling and the DBTT was about 20°C for a peak hoop stress of 114 MPa. Data are also shown for the 145-MPa RHT case even though this hoop stress is considered to be excessive for dry-cask-stored fuel rods. Although more data are needed to accurately determine the DBTT for this case, the data shown in Fig. 6 indicate a relatively low DBTT of about 60°C.

As-irradiated HBU Zry-4 with moderate hydrogen content (300 wppm) exhibited high-ductility at RT and 5 mm/s displacement rate. With the exception of oxide cracking, no cracks were observed following 1.7-mm displacement. Thus, the Zry-4 metal retains ductility even after an exposure to a fast fluence (neutron energy > 1 Mev) of 1.4×10^{26} n/m^2. However, for HBU Zry-4 with very high hydrogen content (640±140 wppm, maximum local value >850 wppm average across cladding wall), offset strains were determined to be 1.7±0.5% for five RCTs at 0.05 mm/s to 50 mm/s and 20°C to 90°C. The embrittlement appeared to be caused by high concentrations of circumferential hydrides. However, as is illustrated in Fig. 5, load-displacement curves were characterized by a series of small load drops interspersed with load increases associated with plastic flow of the metal matrix.

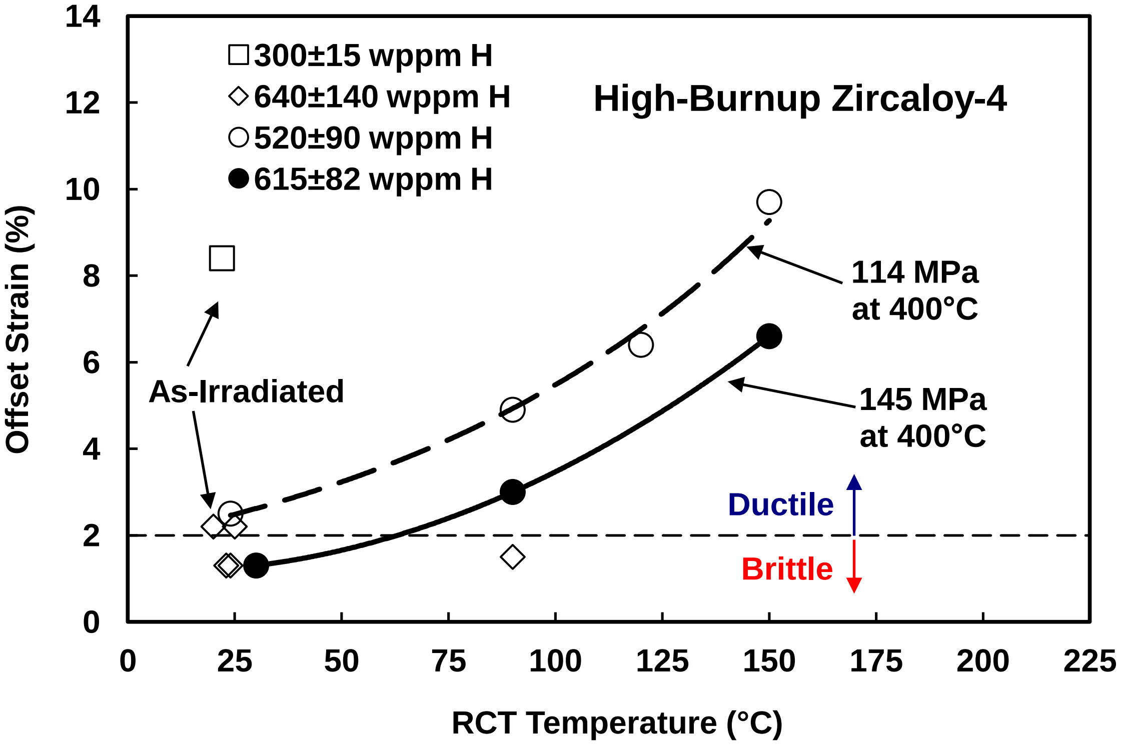

Figure 6: Summary of ductility data for HBU Zry-4 in the as-irradiated condition and following RHT at 400°C peak cladding temperature.

For one of the slow displacement-rate tests, the load was removed after a total load drop of 27% (see Fig. 7) and post-RCT metallographic examination of the ring mid-span was performed to determine the presence of a single crack extending from the outer cladding surface through 44% of the cladding wall (Fig. 8). On the basis of pre-and post-RCT diameter measurements in the loading direction, it was determined that the permanent displacement was 2.1% for <50% wall cracking. These data, along with new data, are used in Section 4.1 to establish the criteria for determining the ductility for cladding materials with only circumferential hydrides.

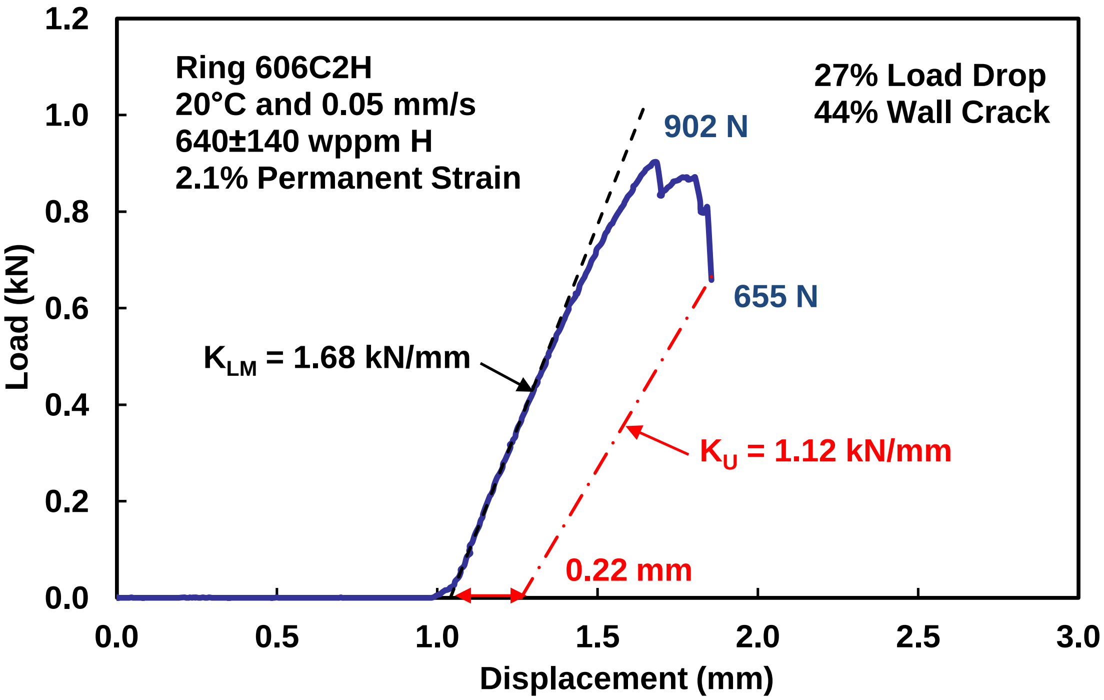

Figure 7: Load-displacement curve for as-irradiated HBU Zry-4 subjected to a RCT at RT and 0.05 mm/s with the load removed after a load drop of 27%.

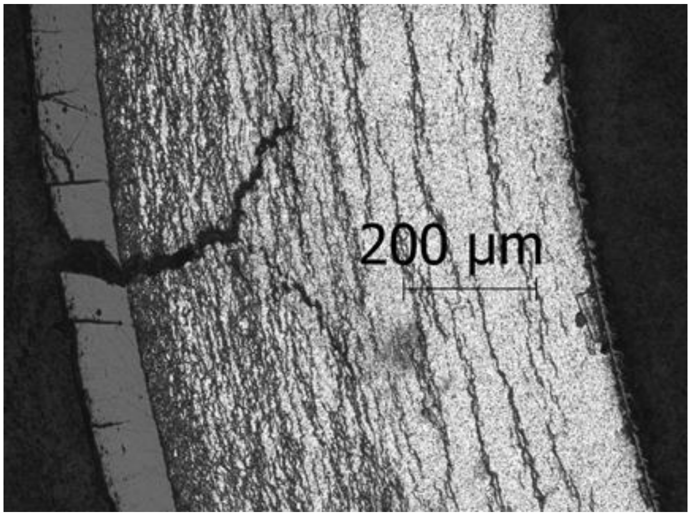

Figure 8: Post-RCT metallographic image of as-irradiated HBU Zry-4 subjected to the RCT shown in Fig. 7.

3.2 PREVIOUS RESULTS FOR HBU ZIRLO™

HBU ZIRLO™ was subjected to RCTs in the as-irradiated condition and following RHT at a peak temperature of 400°C and peak hoop stresses of 80 MPa to 140 MPa. The hydrogen concentrations of the test samples ranged from about 350 wppm to 650 wppm. In the as-irradiated condition HBU ZIRLO™ had relatively high ductility of 6% to >11% offset strain for tests conducted at RT displacement rates of 0.05 mm/s to 50 mm/s and at 5 mm/s and RT to 150°C. For a peak RHT hoop stress of 80 MPa, radial hydrides were short (effective length of 9±4% radial hydride continuity fraction [RHCF]) and ductility values were relatively high at RT (5%) and at 90°C (>11%) to 150°C. Thus, for peak RHT hoop stresses ≤80 MPa, the corresponding DBTT is <20°C and radial-hydride-induced embrittlement is not an issue. These test results are documented in Refs. 6 and 9. For a peak RHT hoop stress of 141 MPa, the DBTT was >150°C (estimated to be 185°C). However, this stress level was too high to be considered relevant to HBU fuel rods in dry-cask storage. On the basis of EOL-RIP data collected for fuel rods irradiated to 40 to 80 GWd/t (see Section 5), relevant stresses at 400°C appear to be in the range of 80 MPa to 110 MPa.

Figure 9 shows ductility results for rodlets subjected to target peak hoop stresses of 90 MPa and 110 MPa at 400°C. Two sets of rodlets were subjected to each peak RHT hoop stress, which resulted in eight RCT ductility values at each stress level. Actual peak hoop stresses based on post-RHT determination of cladding metal wall thickness and outer diameter were 111 MPa (one-drying-cycle rodlet), 89 MPa (one-drying-cycle rodlet) and 88 MPa (three-drying-cycle rodlet).

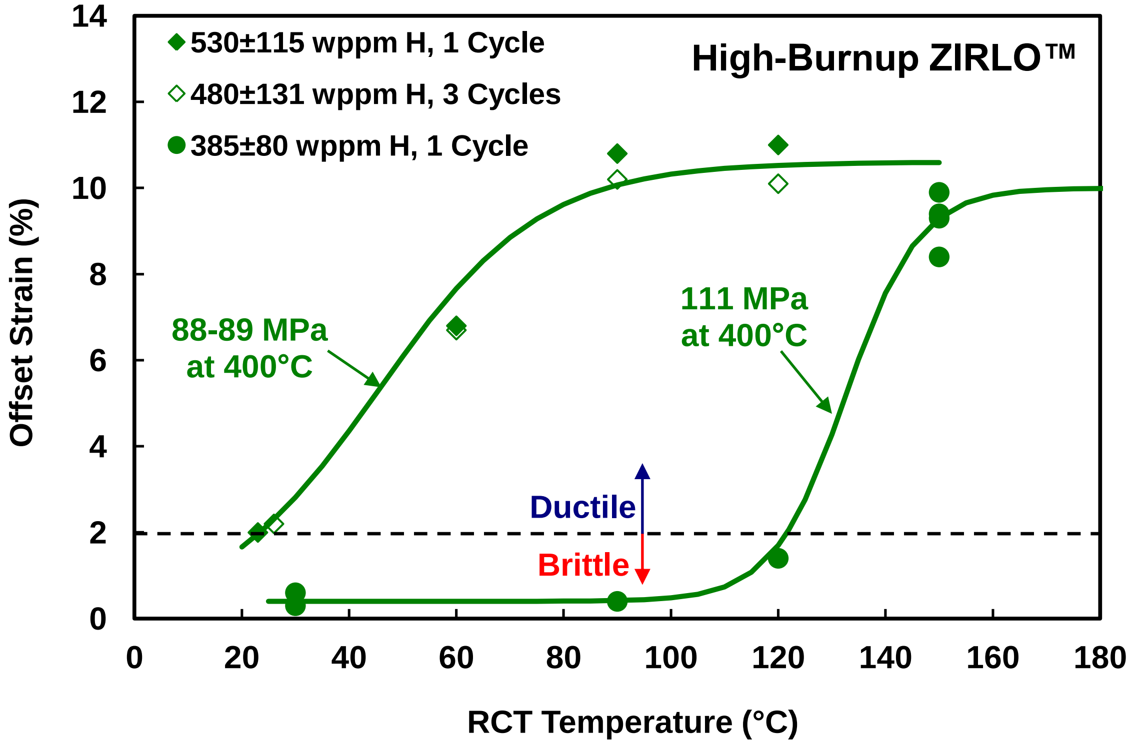

Figure 9: Summary of ductility data for HBU ZIRLO™ following RHT at 400°C peak cladding temperature.

DBTT values were determined to be about 23°C for RHT peak hoop stresses of 88–89 MPa (≈90 MPa) and 122°C for a RHT peak hoop stress of 111 MPa. This rather sharp decrease in DBTT with decreasing stress emphasizes the need for determining percentages of fuel rods in dry storage which experienced peak hoop stresses <90 MPa, between 90 MPa and 111 MPa, and >111 MPa. Also, data are needed for rodlets subjected to intermediate values of peak RHT hoop stress (e.g., 100±5 MPa).

In terms of data assessment, the four data points at 150°C for 111-MPa RHT rings give reasonable assurance that the DBTT is <150°C. The three data points at 30°C and 90°C, along with the one data point at 120°C are sufficient to conclude that the DBTT is >90°C. However, only one data point was generated near the ductile-to-brittle transition. One repeat RHT rodlet should be prepared and four additional RCTs should be conducted in the narrow temperature range of 120°C to 130°C to generate a more robust data set for DBTT determination.

The hoop stresses shown in Fig. 9 are the maximum values at 400°C. From a mechanistic viewpoint, the hoop stress at the initiation of hydride precipitation, especially radial hydride precipitation, is more fundamental. Using the 65°C ΔT_{PD} (difference between T_P and T_D) established in Section 1, the hoop stresses at which radial hydrides are likely to begin precipitating are: (a) 100 MPa for the 111-MPa RHT and (b) 80 MPa for the 89-MPa and 88-MPa RHT.

Two useful graphs can be drawn from the data previously generated for HBU ZIRLO™. Figure 10 shows a plot of DBTT vs. peak hoop stresses at 400°C, as well as the hoop stresses at which the initiation of radial hydride precipitation begins. As most tests by other researchers are conducted at constant pressure and hoop stress during cooling, the hoop stress at which radial hydride precipitation initiates is more relevant for comparison to other research results. Figure 11 is more fundamental as it shows DBTT as a function of the effective lengths of continuous radial-circumferential hydrides (RHCF). As RHCF is generated before RCTs are conducted, the graph is used to estimate RCT temperatures with the goal of choosing two temperatures for which the cladding is likely to be brittle and two temperatures for which the cladding is likely to be ductile.

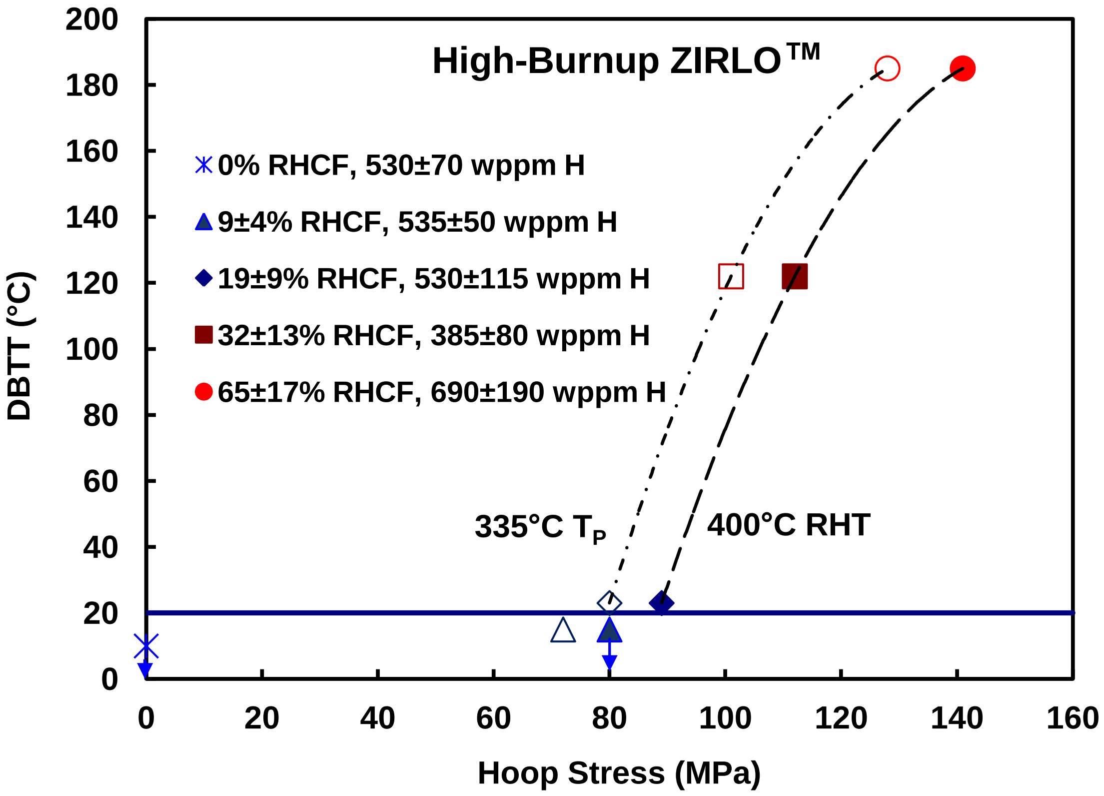

Figure 10: DBTT of HBU ZIRLO™ as a function of peak cladding hoop stress at 400°C and at the T_P.

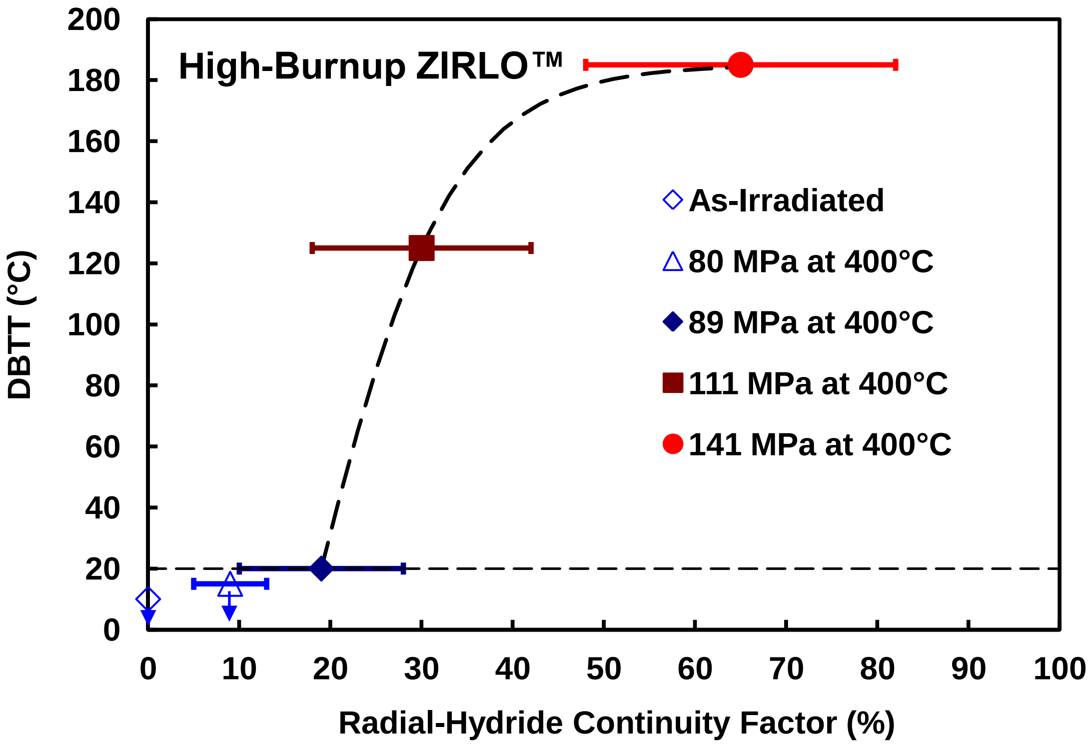

Figure 11: DBTT of HBU ZIRLO™ as a function of RHCF for 400°C RHT temperature.

Page intentionally blank

4. RESULTS FROM CURRENT TESTS

4.1 AS-IRRADIATED HBU ZRY-4

Additional RCTs were conducted with as-irradiated HBU Zry-4 to resolve the issue of the apparently low ductility of the material with high hydrogen content. Previous tests were conducted with HBU Zry-4 containing 640±140 wppm and a peak local hydrogen content >850 wppm (averaged over the cladding wall thickness). Figure 12 shows the sectioning diagram for the HBU Zry-4 segment 605C3 used in the current testing.

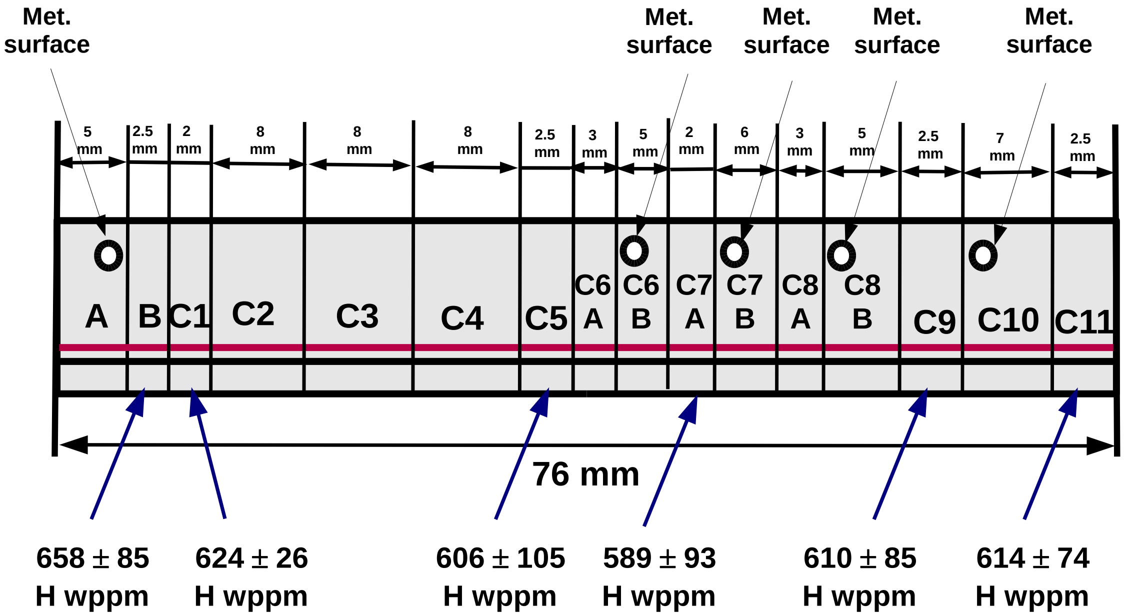

Figure 12: Sectioning diagram for as-irradiated HBU Zry-4 segment 605C3

Prior to conducting RCTs, hydrogen concentrations were determined using rings B, C1, C5, C9, and C11 and metallographic examinations were performed using rings A and C10. Samples C2, C3, C4, C6, C7, and C8 were used to conduct RCTs. Following RCTs, rings C6, C7, and C8 were sub-sectioned to produce one ring for hydrogen-content measurement (C7A) and three rings for metallographic examination (C6B, C7B, and C8B).

The average segment outer diameter (D_o), oxide layer thickness (h_{ox}), metal outer diameter (D_{mo}), and metal wall thickness (h_m) were 10.79 mm, 99±5 µm, 10.59 mm, and 0.71 mm, respectively. These values are comparable to those measured for the as-irradiated HBU Zry-4 segment 606C2 used in the previous study. The average and one-standard deviation for the hydrogen-content measurements (3 to 4 arc-length measurements at each axial location) were 616±78 wppm, with a maximum local concentration of 744 wppm for the 21 individual measurements.

RCTs were conducted at 5 mm/s and temperatures of 20°C, 60°C, 90°C, and 120°C. Two additional rings were tested at 0.05 mm/s and at 20°C and 120°C to allow removal of the load after load drops of 20 to 30%. These load-interrupt tests, along with the one shown in Figs. 7 (load-displacement) and 8 (metallographic image of crack) proved to be essential for interpretation of new data and re-interpretation of previous data. Results of the load-interrupt tests are discussed first because they were used to determine ductility values for the remaining tests.

Figure 13 shows load-displacement results for the load-interrupt test conducted at 20°C and 0.05 mm/s. The test was terminated (i.e., loading rod was retracted) after a load drop of 22%. Figure 14 is from the 100X metallographic image of the single long crack that initiated at the outer surface and propagated through 41% of the cladding wall. On the basis of measured pre- and post-test diameters, the permanent displacement and strain were determined to be 0.23 mm and 2.2%, respectively. By connecting the final displacement point to the permanent displacement on the zero-load axis, the unloading slope (1.21 kN/mm) was determined for the partially cracked sample. This unloading slope is about 64% of the loading slope, which is lower than predicted by Eq. 2a for intact rings with no crack growth. The sequence of small load drops interspersed with load increases is indicative of radial crack growth through the densest part of the hydride rim, cracking along more sparsely distributed circumferential hydrides, and plastic flow and cracking of the metal matrix between circumferential hydrides. Crack growth through the ductile metal matrix tends to occur along a line that is about 45° from the radius. Evidence of crack growth through the metal matrix can be seen in Fig. 14 for the inner half of the crack.

Figure 15 shows results for the second load-interrupt test conducted at 0.05 mm/s and 120°C. The test was terminated after a total load drop of 24%. The saw-tooth pattern of load drops and load increases is similar to what was observed for the sample tested at 20°C. The permanent displacement and strain were determined to be 0.29 mm and 2.7%, respectively. The unloading slope was 1.10 kN/mm, which is about 60% of the loading slope. The zigzag pattern of crack growth can be seen more clearly in Fig. 16, which is also from a 100X metallographic image, than was observed in Fig. 14. On the basis of the 100X image, it appears as if the crack extends across about 50% of the wall. However, the 200X images shown in Fig. 17 indicate that the 45° line connecting the inner circumferential hydrides is not yet a well-developed crack. With further deformation, it is a likely location for a crack to form.

Data presented in Figs. 13 and 15 were used to express the unloading-to-loading slope ratio as a linear function of the percentage load drop (100 $\Delta P/P_i$, where P_i is the peak load associated with crack initiation, P_d is the minimum load prior to unloading, and $\Delta P = P_i - P_d$) for load drops in the range of 19% to 24% leading to a <50% crack extension across the cladding wall. This relationship (Eq. 3) was used to determine the unloading slopes just prior to ≤50% wall cracking for the four current RCTs conducted at 5 mm/s to 1.7-mm displacement. Figure 7 was used to determine unloading slopes (Eq. 4) for previous tests conducted to 1.7-mm displacement for load drops in the range of 22% to 27%. For smaller load drops, Eq. 2a was used as the upper bound for K_U/K_{LM}.

$$K_U/K_{LM} = 0.64 + 0.02\,(22 - 100\,\Delta P/P_i) \tag{3}$$

$$K_U/K_{LM} = 0.67 + 0.02\,(27 - 100\,\Delta P/P_i) \tag{4}$$

Figures 18 through 21 show load-displacement curves for the four current tests, and Figs 22 through 25 show the re-analyzed load-displacement curves for the previous four tests with as-irradiated HBU Zry-4. As was shown in Fig. 5, cracking in as-irradiated HBU Zry-4 with only circumferential hydrides is less severe than cracking in HBU Zry-4 with radial and circumferential hydrides following RHT. The improved approach for determining ductility (i.e., permanent strain prior to >50% wall cracking) gave ductility values of 2.8±0.7%. The new results are summarized in Fig. 26 for as-irradiated HBU Zry-4. No increase in ductility was observed by increasing the RCT temperature from 20°C to 120°C.

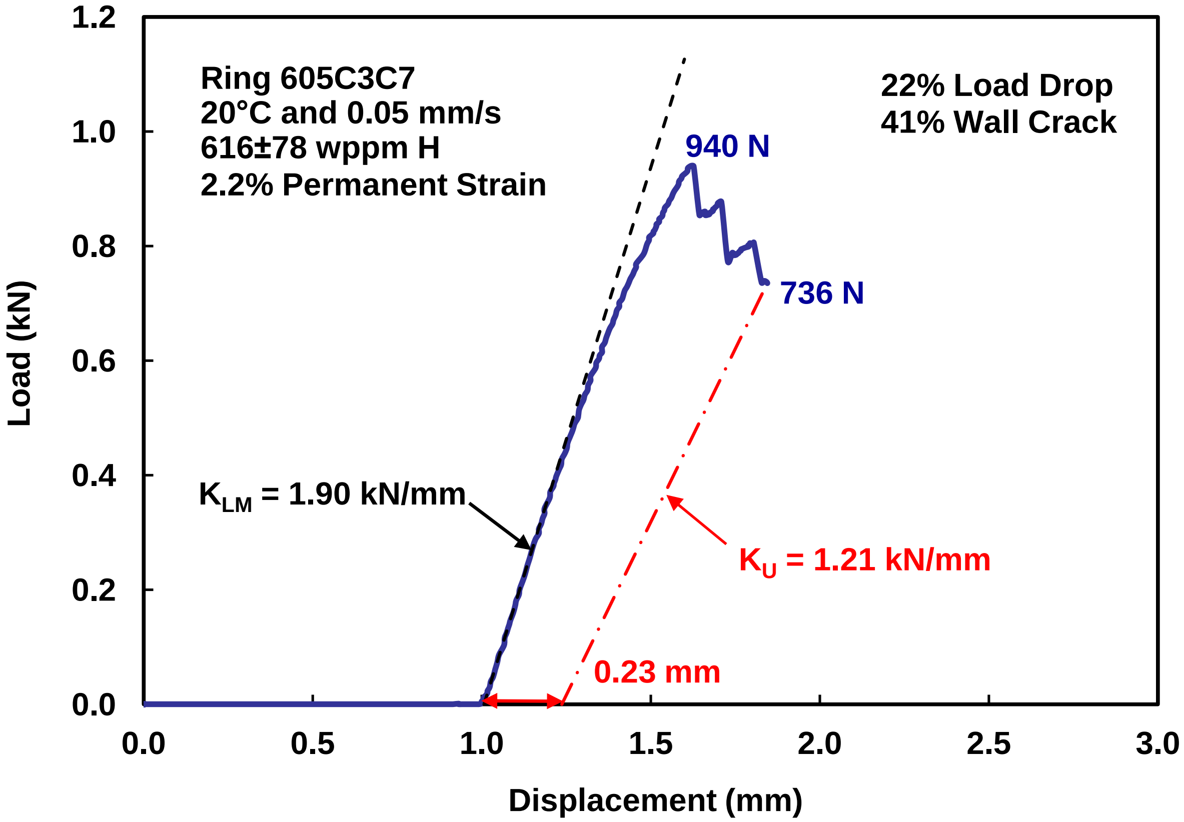

Figure 13: Load-displacement curve for as-irradiated HBU Zry-4 tested at 0.05 mm/s and 20°C.

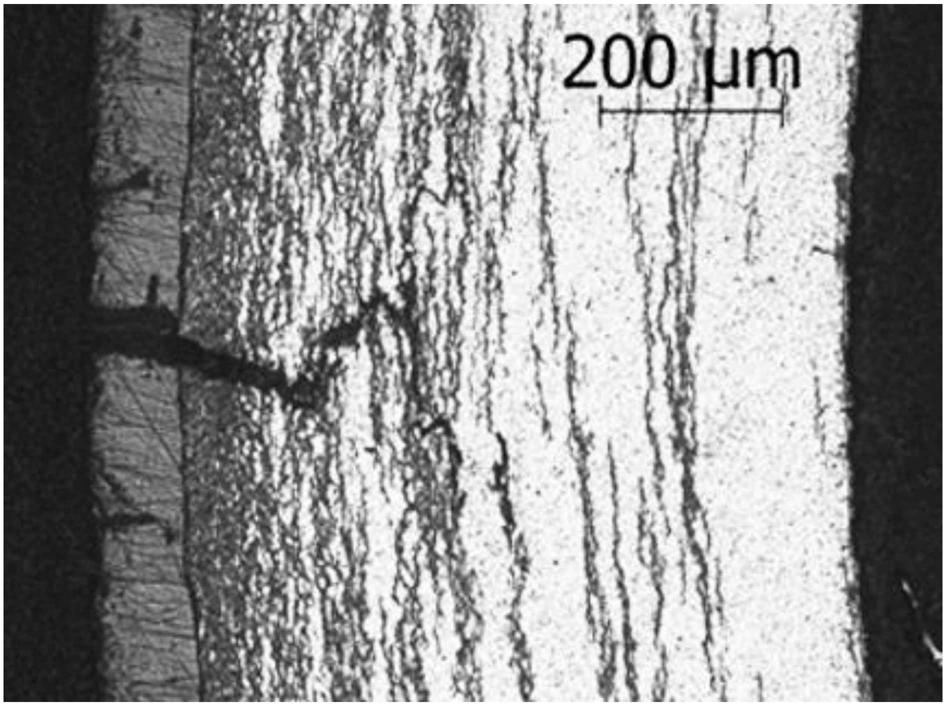

Figure 14: Crack pattern and depth near mid-span of ring 605C3C7 from 100X image.

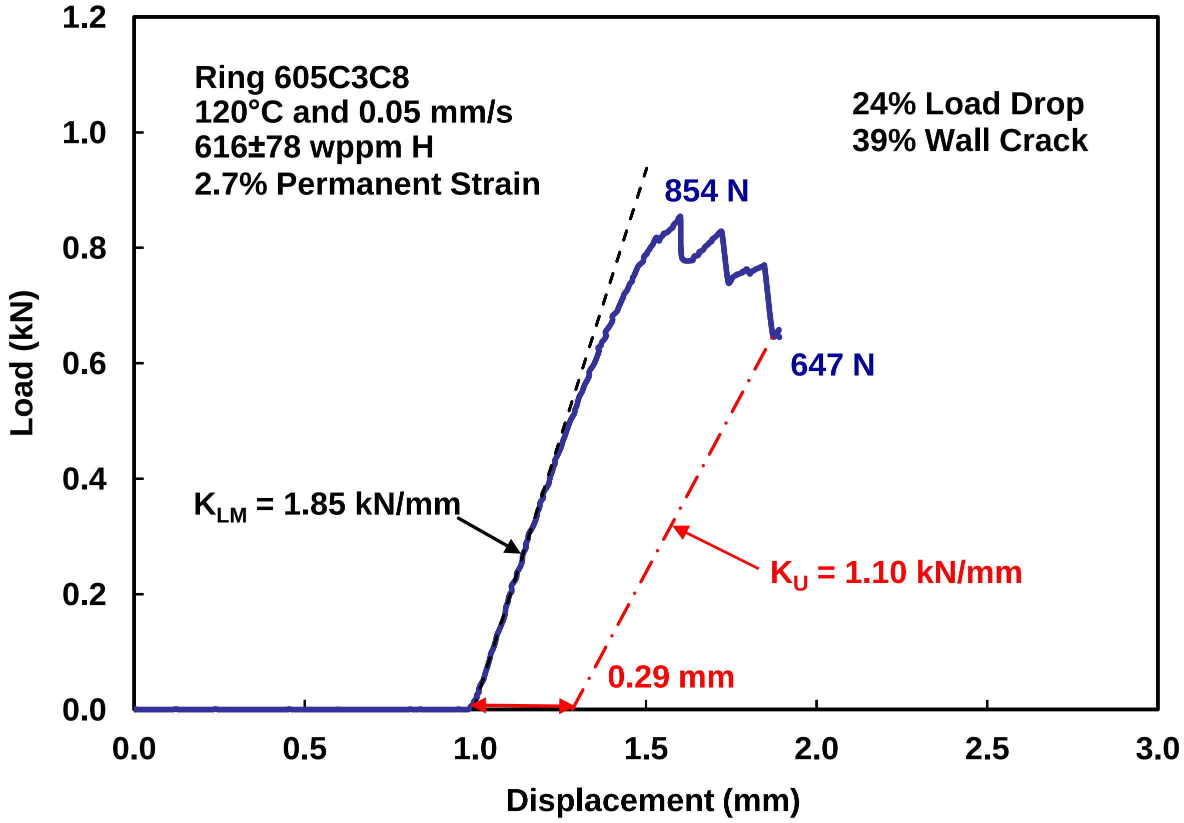

Figure 15: Load-displacement curve for as-irradiated HBU Zry-4 tested at 0.05 mm/s and 120°C.

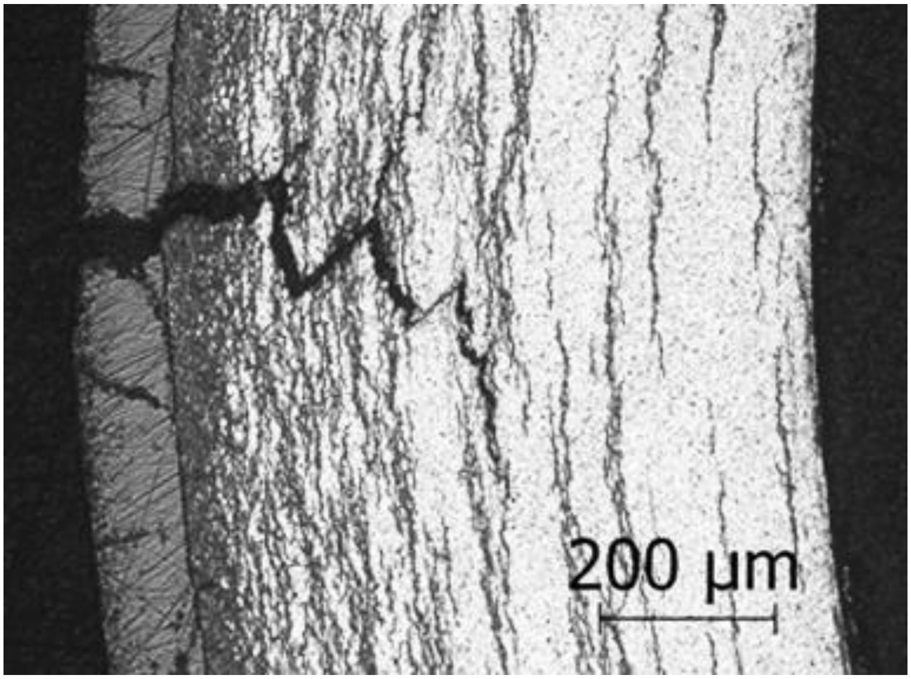

Figure 16: Crack pattern and depth near mid-span of ring 605C3C8 from 100X image.

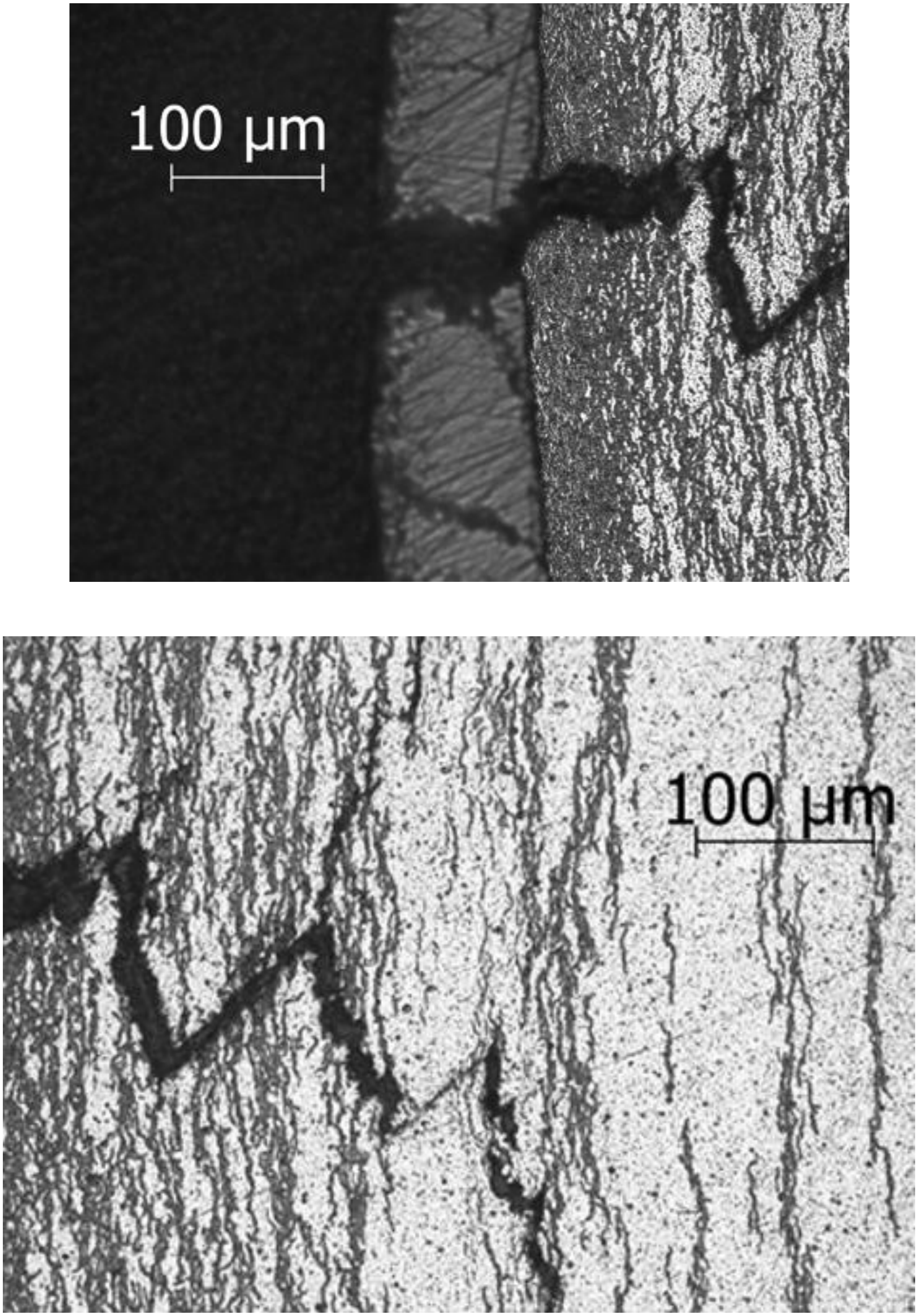

Figure 17: Crack pattern and depth near mid-span of ring 605C3C8 from 200X images.

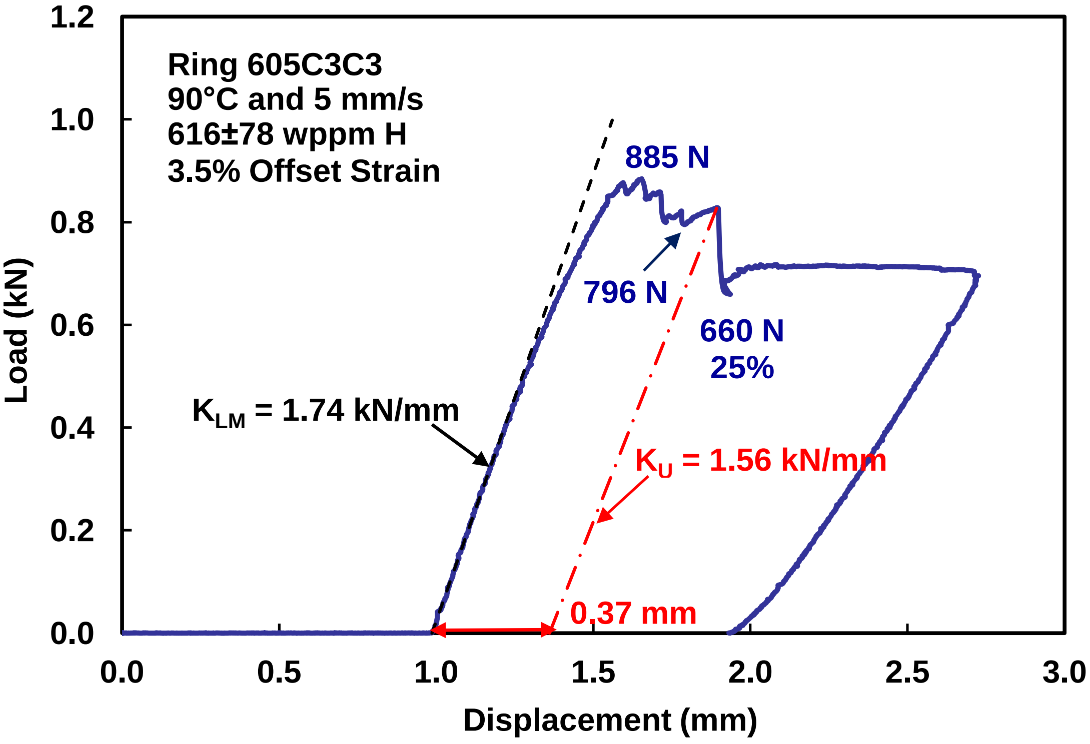

Figure 18: Load-displacement curve for as-irradiated HBU Zry-4 tested at 5 mm/s and 20°C.

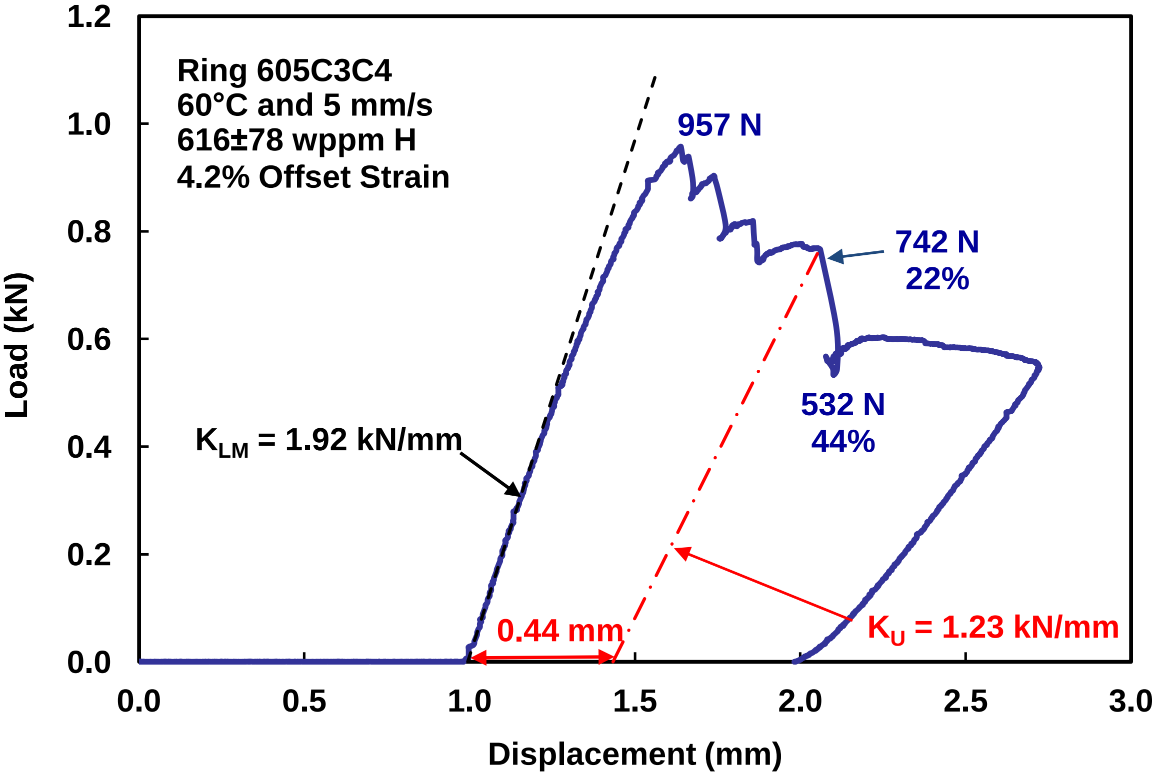

Figure 19: Load-displacement curve for as-irradiated HBU Zry-4 tested at 5 mm/s and 60°C.

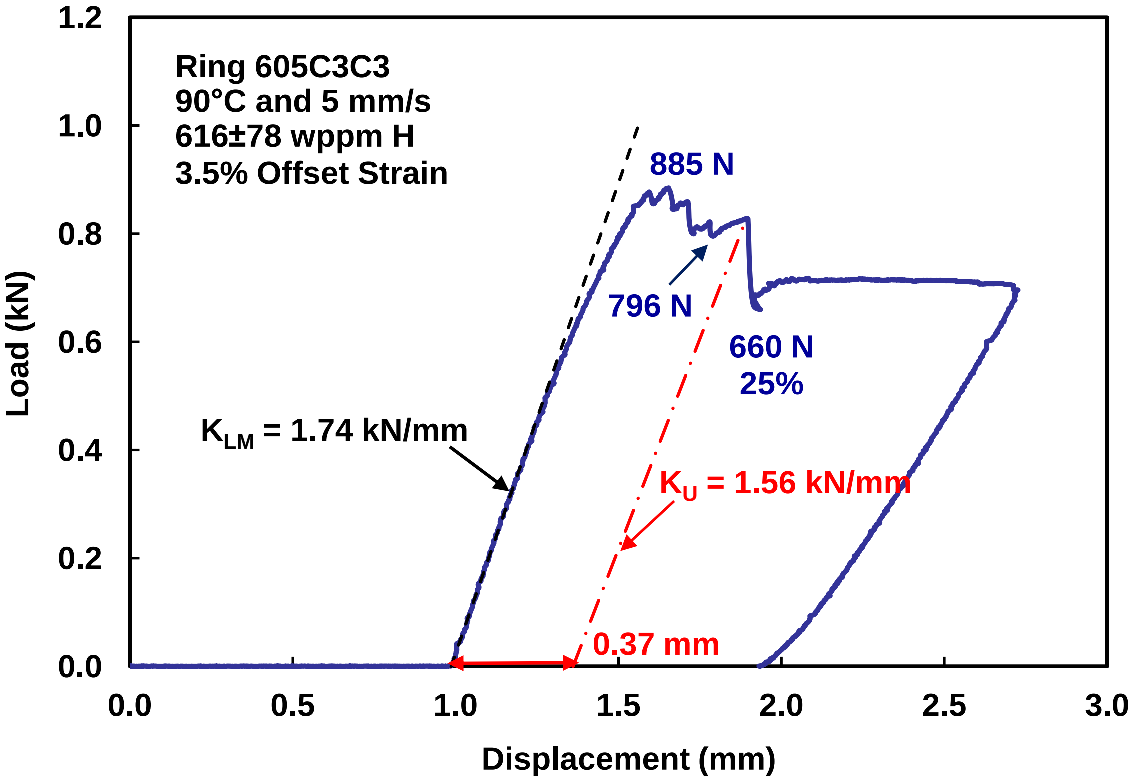

Figure 20: Load-displacement curve for as-irradiated HBU Zry-4 tested at 5 mm/s and 90°C.

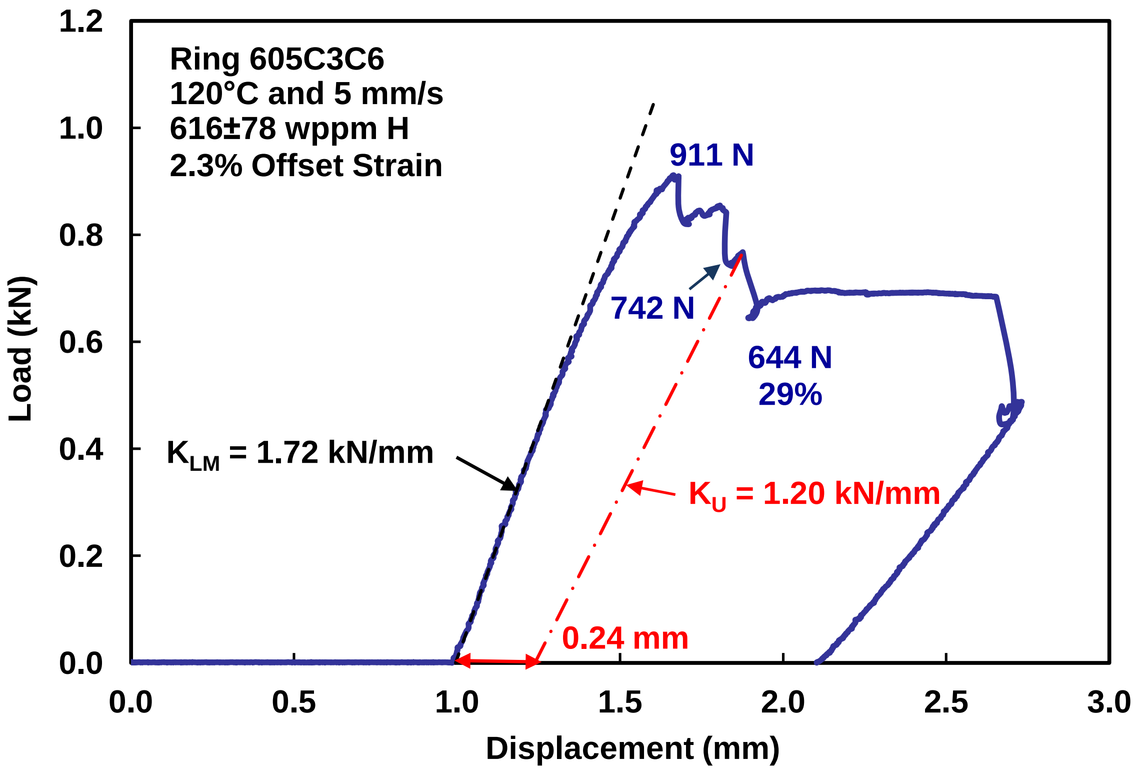

Figure 21: Load-displacement curve for as-irradiated HBU Zry-4 tested at 5 mm/s and 120°C.

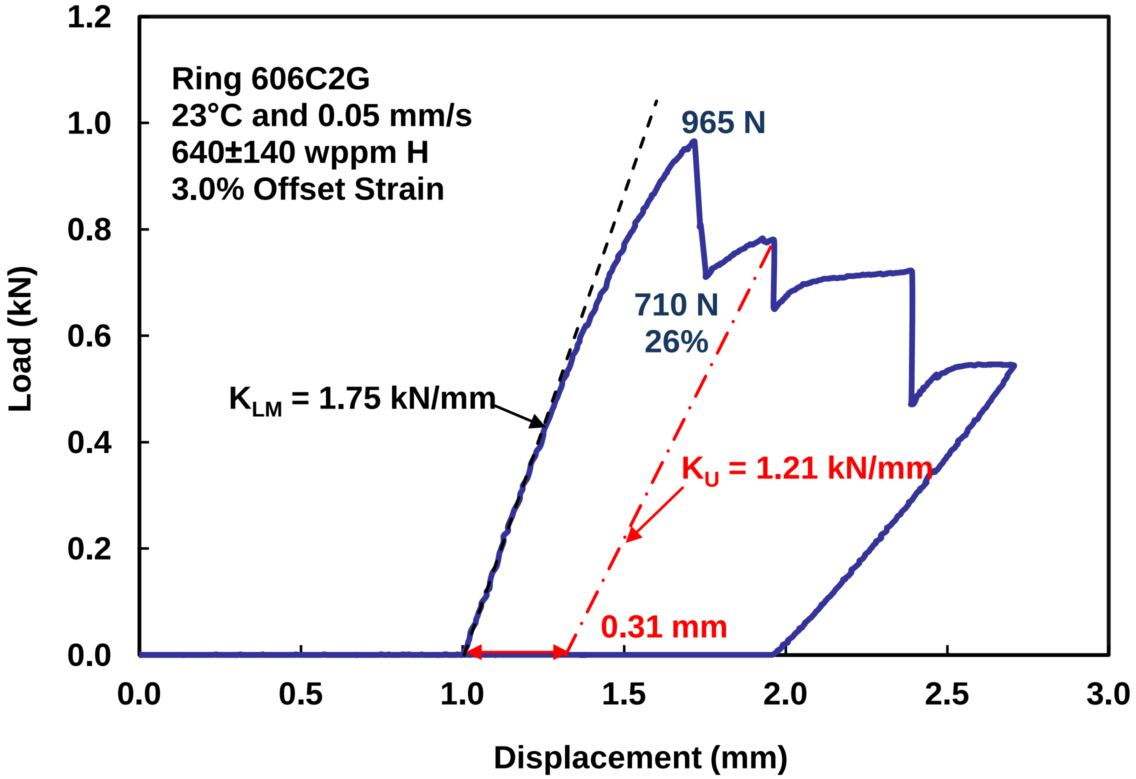

Figure 22: Load-displacement curve for as-irradiated HBU Zry-4 tested at 0.05 mm/s and 20°C.

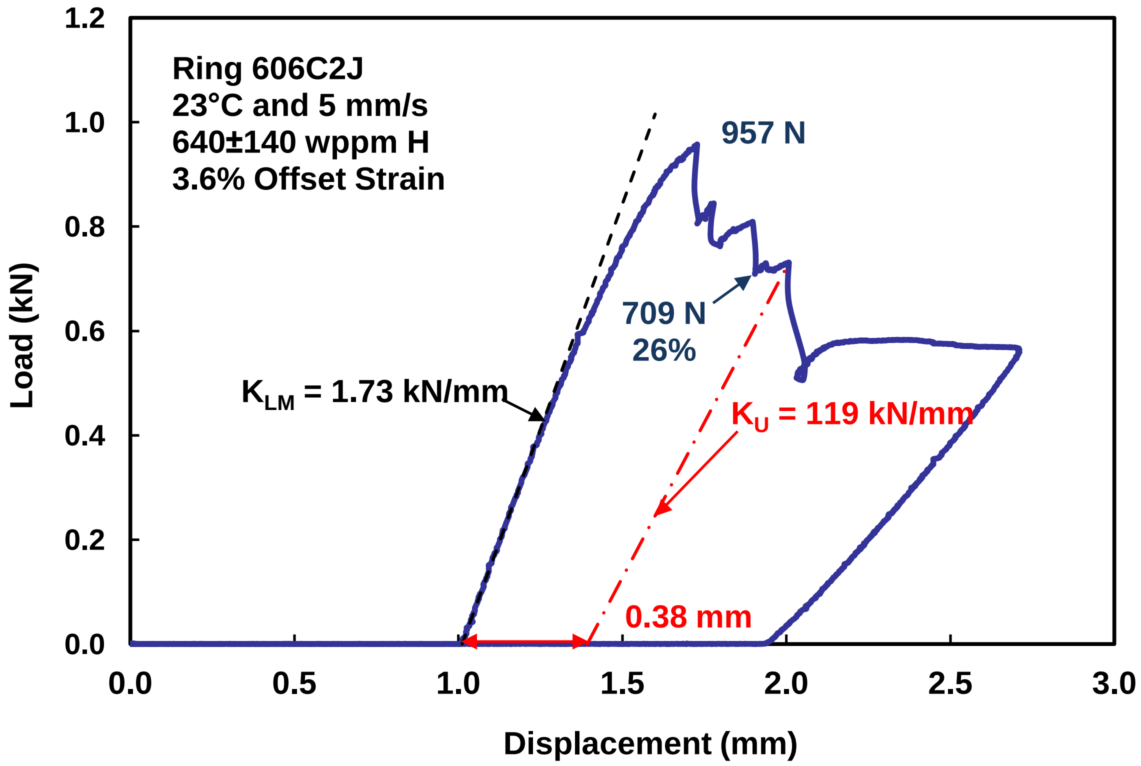

Figure 23: Load-displacement curve for as-irradiated HBU Zry-4 tested at 5 mm/s and 20°C.

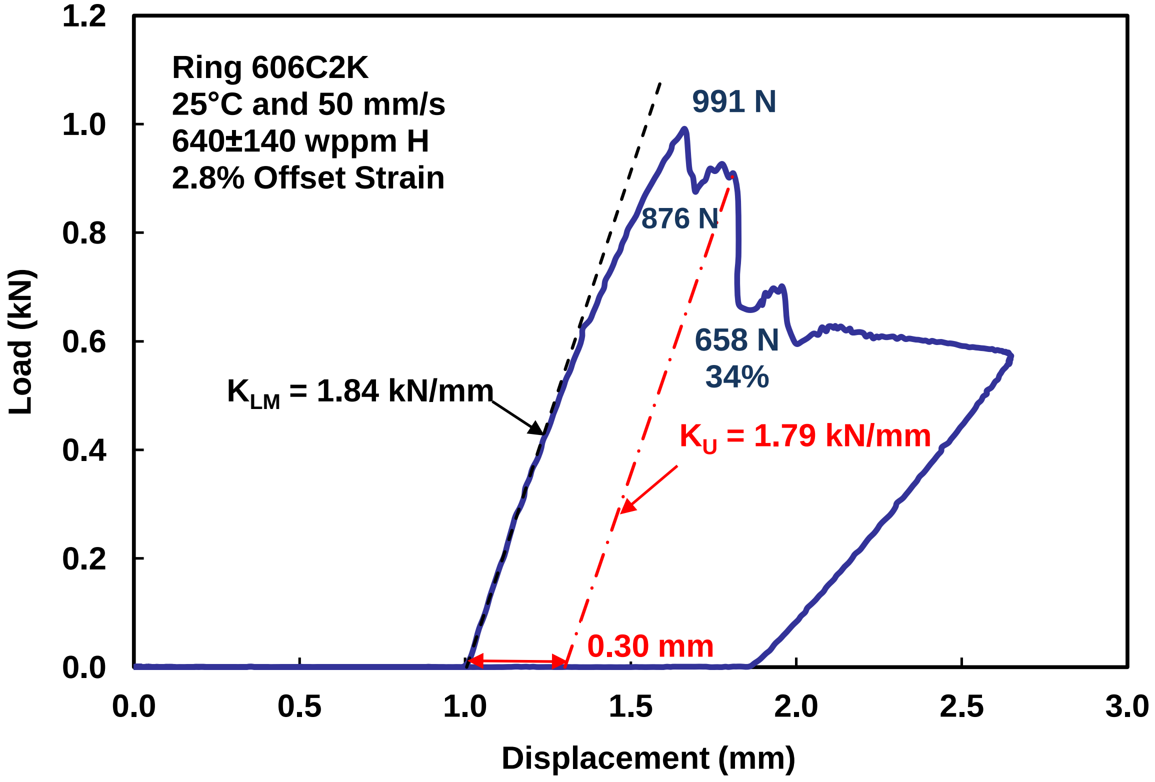

Figure 24: Load-displacement curve for as-irradiated HBU Zry-4 tested at 50 mm/s and 20°C.

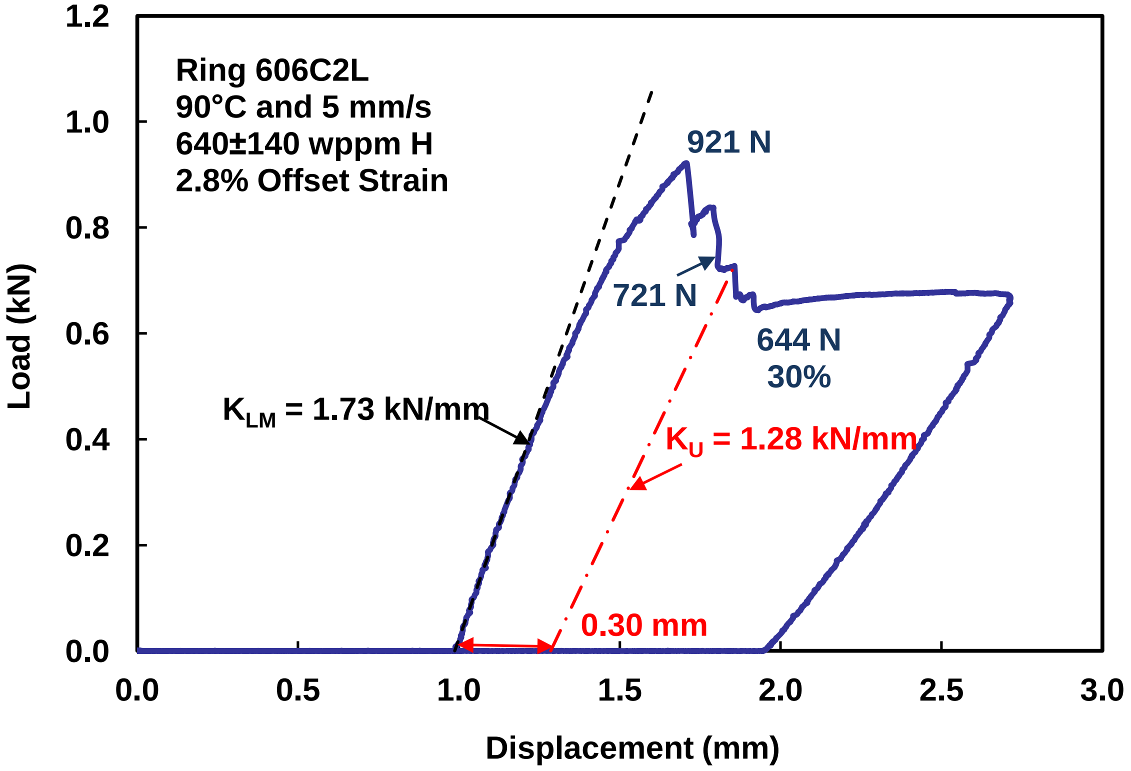

Figure 25: Load-displacement curve for as-irradiated HBU Zry-4 tested at 5 mm/s and 90°C.

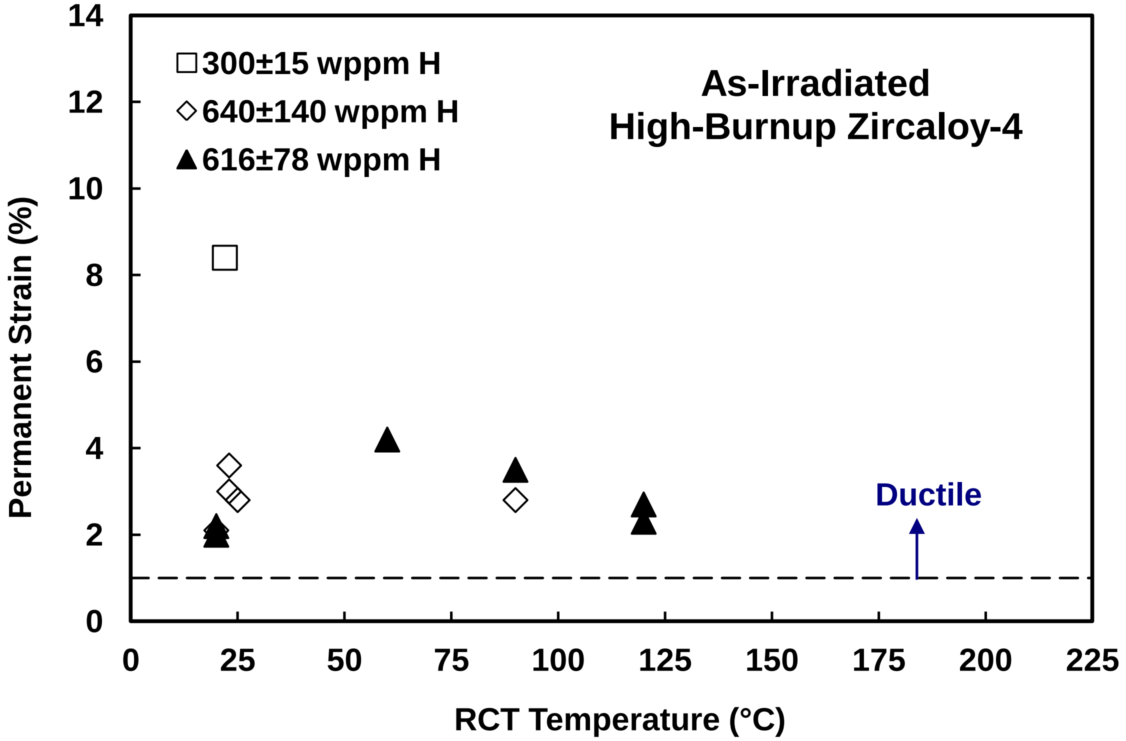

Figure 26: Summary of calculated and measured permanent strains (i.e., ductility) for as-irradiated HBU Zry-4 with low (300 wppm) and high (>600 wppm) hydrogen contents.

4.2 HBU ZIRLO™ TESTED AT 350°C PEAK RHT TEMPERATURE

Two tests were conducted with HBU ZIRLO™ rodlets subjected to a peak drying-storage temperature of 350°C: rodlet 105E subjected to three simulated drying cycles with temperature drops of 100°C and rodlet 105F subjected to one simulated drying cycle. The target peak hoop stress at 350°C was 92 MPa for both tests. Characterization results for rodlet 105E were presented in Ref. 10. They are repeated in this section to allow direct comparisons between the two tests and an assessment of the effects of cycling on the extent of radial hydride precipitation and radial-hydride-induced embrittlement.

During this reporting period, the new work with 3-cycle rodlet 105E included conducting RCTs on four rings, sub-sectioning of two post-RCT samples, determination of hydrogen content for about half of each ring, and metallographic examination of the mid-span of each sub-sectioned ring to determine the number and extent of cracks and the effective lengths of radial hydrides (i.e., RHCF). Figure 27 shows the new sectioning diagram for the 3-cycle rodlet 105E, along with the results of the additional hydrogen-content measurements and locations for metallographic imaging. Rings 3, 4, 7, and 8 were used for RCTs. Following RCTs, rings 3 and 7 were sub-sectioned for hydrogen-content determination (3B and 7B) and metallographic examination (3A and 7A).

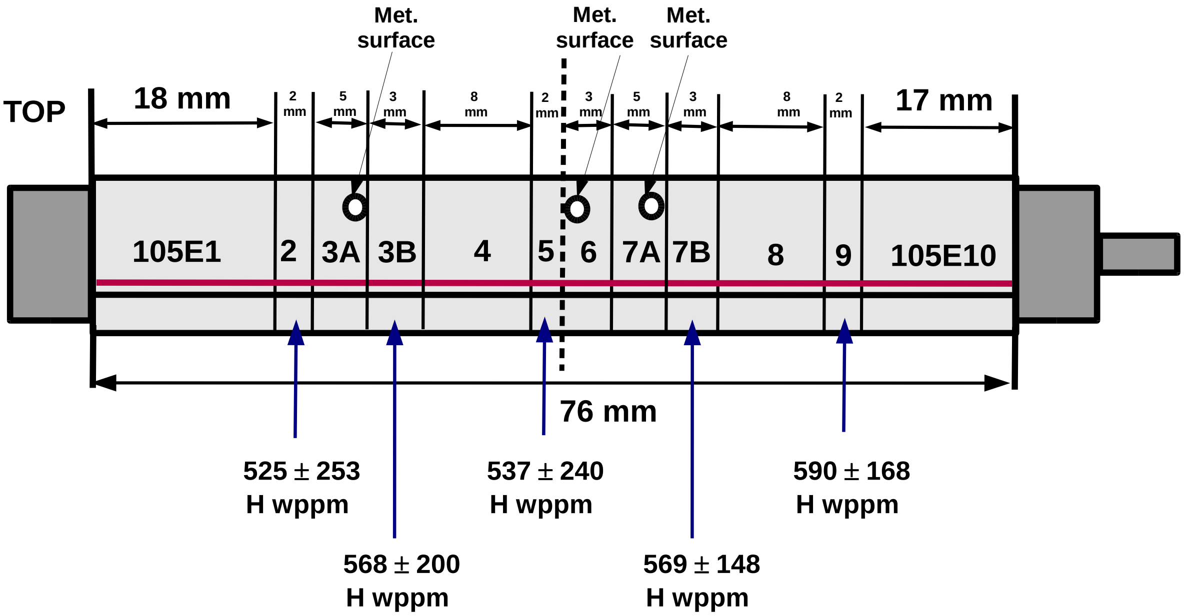

Figure 27: New sectioning diagram for HBU ZIRLO™ 3-cycle rodlet 105E.

New testing was performed using HBU ZIRLO™ rodlet 105F, which was sectioned adjacent to and above 105E on the same fuel rod. By subjecting this rodlet to 1-cycle heating and cooling at the same target peak RHT conditions as rodlet 105E, a direct evaluation of the effects of temperature cycling could be made, as well as an evaluation of possible benefits of reducing the peak RHT temperature from 400°C to 350°C for both cases. The sectioning diagram for rodlet 105F is shown in Fig. 28. Post-RHT and pre-RCT characterization paralleled the characterization performed for rodlet 105F: hydrogen content measurements for rings 2, 5, and 9 and metallographic examination of the indicated surface for ring 6. Rings 3, 4, 7, and 8 were subjected to RCTs. Following RCTs, rings 4 and 7 were sub-sectioned to generate samples for additional hydrogen-content measurements and metallographic examination to determine the number and extent of cracks, as well as the extent of radial hydride precipitation.

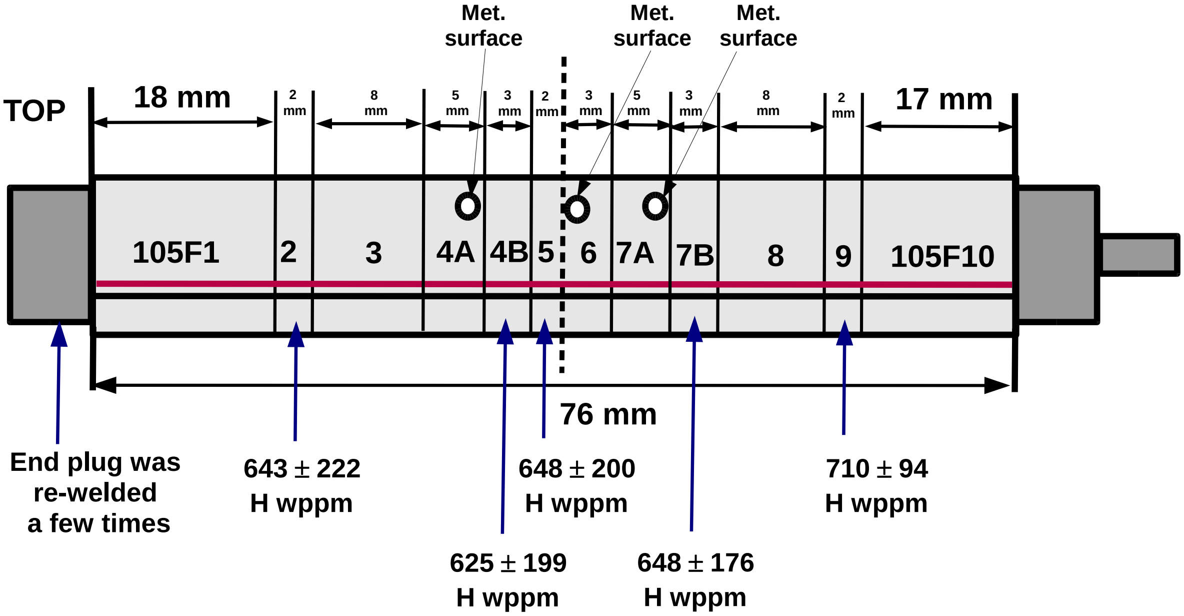

Figure 28: Sectioning diagram for HBU ZIRLO™ 1-cycle rodlet 105F.

Table 2 gives the characterization results for rodlets 105E and 105F, as well as the hoop stress levels at three temperatures based on the actual measurements of the corroded cladding outer diameter (micrometer measurements), oxide layer thickness (from metallographic images), and metal wall thickness (from metallographic images). The peak hoop stresses calculated using the actual geometrical parameters were very close to the target hoop stress of 92 MPa: 93 MPa for rodlet 105E and 94 MPa for rodlet 105F. The hoop stresses at which new hydride precipitation initiates were calculated to be 83 MPa and 84 MPa, respectively. The primary difference between the rodlets is the thicker oxide layer and the correspondingly higher hydrogen content for rodlet 105F.

4.2.1 Radial Hydride Precipitation based on Pre-RHT Examinations

The pre-RCT determination of the RHCF and the locations of the longer radial hydrides are important for determining the sample orientation with respect to the RCT load application point and in selecting the initial test temperature.

Thirty-four overlapping 100X metallographic images covering the whole cross section of ring 105E6 are shown in Appendix A of Ref. 10. At each of these locations, 200X images were also taken to determine radial hydride lengths, continuity of radial hydrides, and continuity of circumferential-radial hydrides. To allow for the effects of etching (e.g., moderate over-etching vs. moderate under-etching), radial hydrides separated by a gap of ≤5 µm are considered to be continuous. This gap is measured within ±45° from the top of one radial hydride to ±45° from the bottom of the next radial hydride. Gaps between a radial hydride and a circumferential hydride are treated as discontinuous in the determination of the RHCF. The assumption is made that cracks propagating along a radial hydride can rapidly propagate to the next radial hydride with a separation of ≤5 µm. It is also assumed that cracks will not propagate rapidly through a gap between the tip of a radial hydride and a circumferential hydride, which is parallel to the global stress field. Using these assumptions, the pre-RCT RHCF for ring 6 of rodlet 105E was determined to be 32±12% with a maximum value of 55%.

Table 2 Post-RHT characterization results for HBU ZIRLO™: 3-cycle rodlet 105E and 1-cycle rodlet 105F subjected to peak RHT conditions of 350°C and 92 MPa hoop stress prior to cooling at 5°C/h down to 200°C (105E) and 135°C (105F).

Parameter	Rodlet 105E 350°C RHT 3-Cycle Cooling	Rodlet 105F 350°C RHT 1-Cycle Cooling
Outer Diameter (D_o), mm	9.53	9.55
Oxide Layer Thickness (h_{ox}), µm	48±6	58±3
Metal Outer Diameter (D_{mo}), mm	9.43	9.44
Metal Wall Thickness (h_m), mm	0.56	0.55
Metal Inner Diameter (D_{mi}), mm	8.31	8.34
Hydrogen Content (C_H), wppm	564±177	644±172
RT Internal Pressure (p_i), MPa	5.97	5.97
Dissolved Hydrogen at T_{max} (C_{HD}), wppm	126±6	126±6
Precipitation Temperature (T_P), °C	285	285
Maximum Hoop Stress (σ_θ), MPa	93	94
Hoop Stress (σ_θ) at T_P, MPa	83	84
Hoop Stress (σ_θ) at 200°C, MPa	70	71
Radial-Hydride Continuity Factor (RHCF), %	30±11	37±11
Surface 1 (ring 6)	32±12	35±10
Surface 2 (rings E3A and F4A)	37±8	37±12
Surface 3 (rings E7A and F7A)	26±10	38±13

Figures 29 and 30 (from 200X images) show a few of the longer radial hydrides. Of the three longer hydrides shown, the one marked with a red arrow in Fig. 30 would be the most damaging if it were located under the load (12 o'clock) or above the support plate (6 o'clock).

At these locations, the maximum hoop bending stress occurs at the cladding inner surface. Radial hydrides that emanate from this surface (e.g., hydride marked with red arrow in Fig. 30) are more vulnerable to crack initiation at low displacement values than radial hydrides that are within the interior of the cladding. It takes a higher load and correspondingly a higher stress to initiate a crack within the interior of the cladding. Depending on the hydride patterns above the interior radial hydrides, they can contribute to crack propagation.

Similar results were obtained for ring 6 of rodlet 105F: 35±11% based on the evaluation of over 40 overlapping images (see Appendix A). For each 100X image, at least one 200X image was taken to assess radial-circumferential hydride continuity within an arc-length of 150 µm. The longest continuous radial-circumferential hydride identified in Appendix A images extended through about 60% of the cladding wall. Figures 31 and 32 show 200X images of long radial hydrides within the 4:15 and 4:30 o'clock areas,

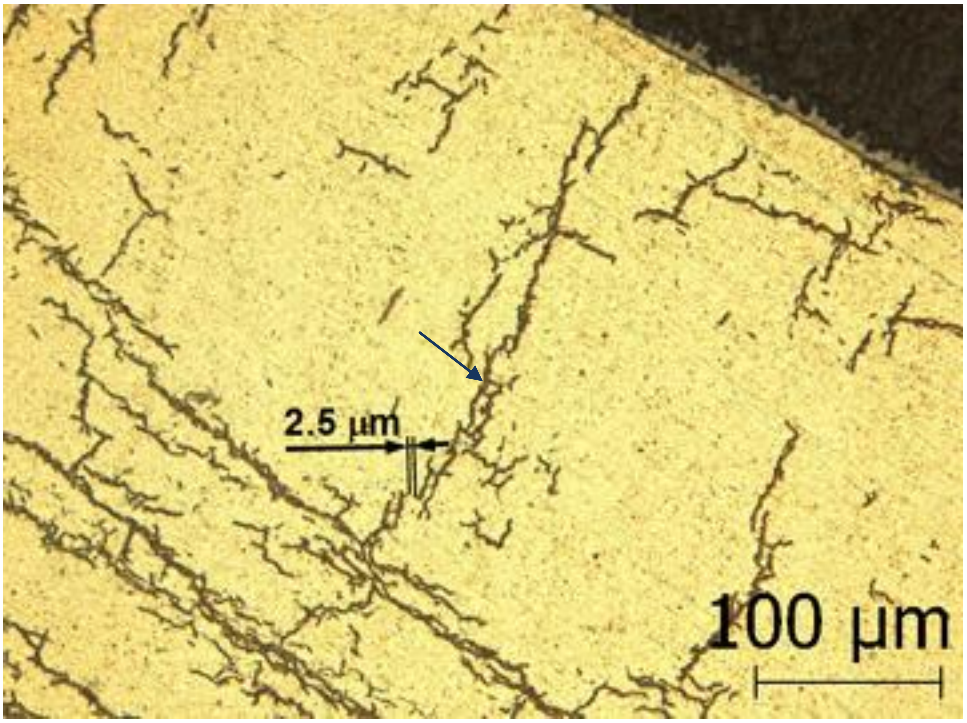

Figure 29: Image of long radial hydride (≈50% of cladding wall up to discontinuity) and 2.5-µm discontinuity within the 7:30 o'clock area of the 105E6 surface.

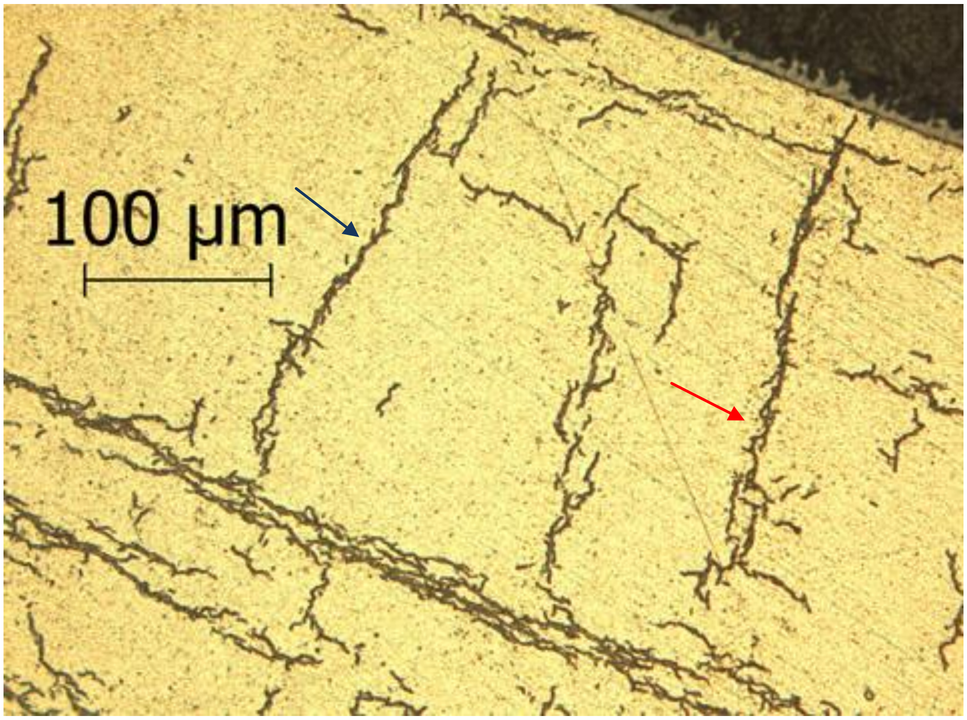

Figure 30: Image of long radial hydrides (≈50% of cladding wall) within the 7:00 o'clock area of the 105E6 surface.

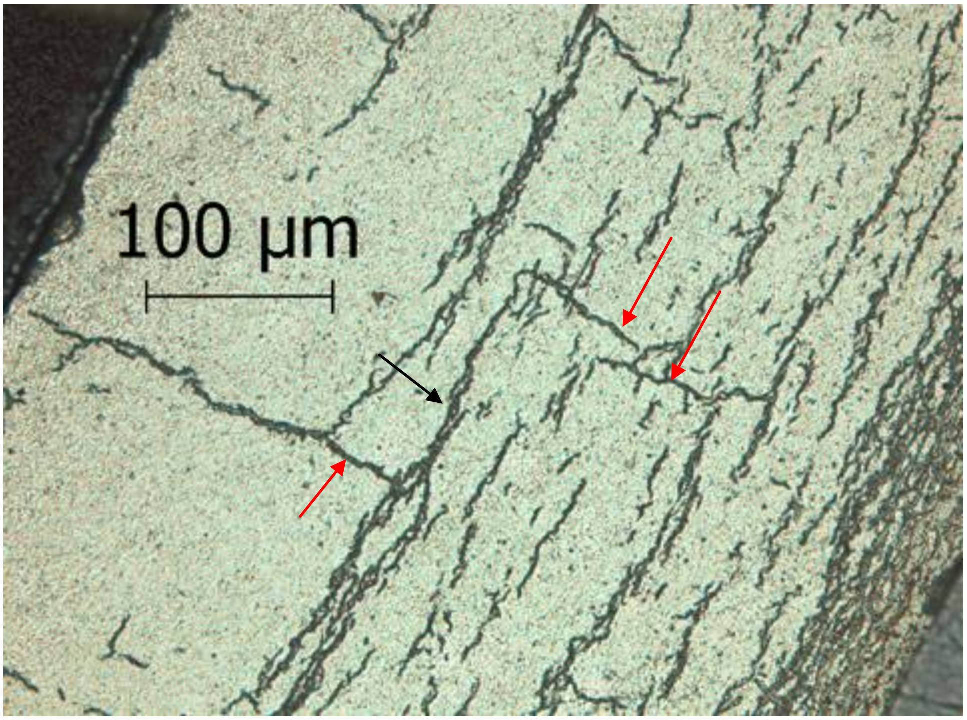

Figure 31: Image of long radial and radial-circumferential hydrides within the 4:15 o'clock area of the 105F6 surface.

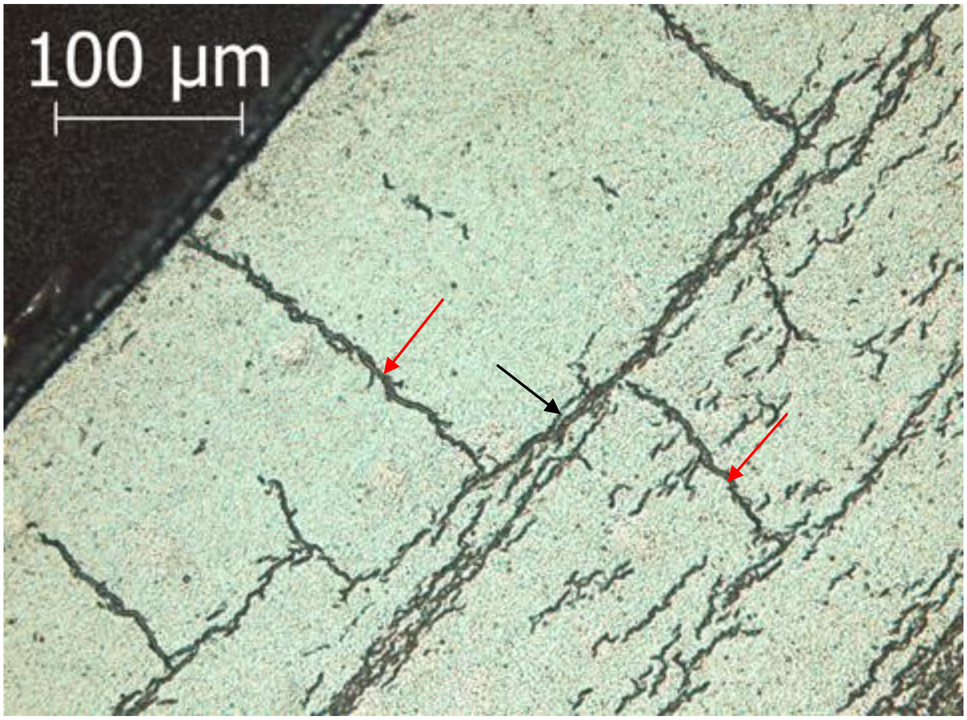

Figure 32: Image of long radial and radial-circumferential hydride within the 4:30 o'clock area of the 105F6 surface.

respectively. The longest radial hydride (red arrow on left) in Fig. 31 is about 48% of the cladding wall. It connects with a circumferential hydride (black arrow), which in turn connects to the radial hydride above, indicated by the second red arrow. Near the outermost tip of this second radial hydride, there is a small gap between it and the third radial hydride. At the intersection of the circumferential hydride and the second radial hydride, the RHCF would be about 50%. Extending the continuous hydrides to the tip of the second radial hydride would give 60% RHCF. If continuity (with 5-µm gap) is assumed at this tip, the hydride extension to the next radial hydride would give 70% RHCF. However, it is unlikely that a crack would initiate at the beginning of the first hydride because it is not in contact with the inner cladding surface. If crack initiation and rapid crack growth were to occur along this innermost radial hydride, crack growth along the connecting circumferential hydride is anticipated to be much slower, while crack growth along the second radial hydride would be rapid. Thus, in terms of rapid crack growth leading to embrittlement, 50% RHCF may be more relevant than 70% RHCF. A similar situation is observed in Fig. 32 except that the innermost long radial hydride (red arrow on left) is in contact with the cladding inner surface. This radial hydride would result in rapid crack growth through 41% of the cladding wall and slower crack growth along the connecting circumferential hydride indicated by the black arrow. This circumferential hydride is not in direct contact with the second radial hydride (red arrow above and to the right). Although the discontinuity is <5 µm, it does not fall within the ±45° zone. It is unlikely that a crack would extend to this second radial hydride at low displacements and high loads. With increasing displacement, the crack could connect to this second radial hydride leading to a 70% wall crack. From the perspective of crack growth leading to embrittlement, a RHCF in the range of 40 to 45% appears to be more relevant than a RHCF of 70%.

4.2.2 RCT and Post-RCT Metallographic Results

For rings from rodlet 105E, RCTs were conducted at 90°C (E4), 120°C (E7), 135°C (E3), and 150°C (E8). Post-RCT hydrogen content measurements (E3B and E7B) and metallographic imaging and evaluations (E3A and E7A) were conducted using subsections of rings E3 and E7. The actual sequence of testing was 120°C, 150°C, 90°C, and 135°C. Figures 33 and 34 show the load displacement curves for tests conducted at 90°C and 150°C, respectively. Interpretation of these curves was relatively straightforward. The ring tested at 90°C was clearly brittle (0.8% offset strain) and the ring tested at 150°C was clearly ductile (8.3% offset strain). Figure 35 shows the load displacement curve for the test conducted at 120°C. The offset strain was determined to be 1.2% (brittle) just prior to the 31% load drop. This load drop was followed by a major load drop that occurred close to the displacement limit of 1.7 mm. Metallographic images were taken at the mid-span of this ring to confirm that at least one crack extended to a length >50% of the wall thickness. Figure 36 shows a major crack at the 6 o’clock orientation that extended through essentially 100% of the wall. The wide crack opening at the cladding inner surface indicates that crack initiation occurred at this surface and crack extension occurred relatively early during the loading. Thus, it is assumed that the first load drop corresponds to the initiation and growth of this crack through >50% of the wall. Partial-wall cracks were also observed at the 12 and 3 o’clock orientations. Metallographic images for these two cracks are shown in Figs. 37 and 38. The crack at 12 o’clock initiated at the cladding inner surface, propagated through about 35% of the wall (wide crack), arrested, and then propagated through most of the wall at a relatively high displacement (thinner crack segments). The crack at 3 o’clock initiated at the cladding outer surface (hydride rim) and propagated in a wavy pattern through about 72% of the wall. It is assumed that most of this crack growth beyond the hydride rim occurred at high displacement during the last load drop.

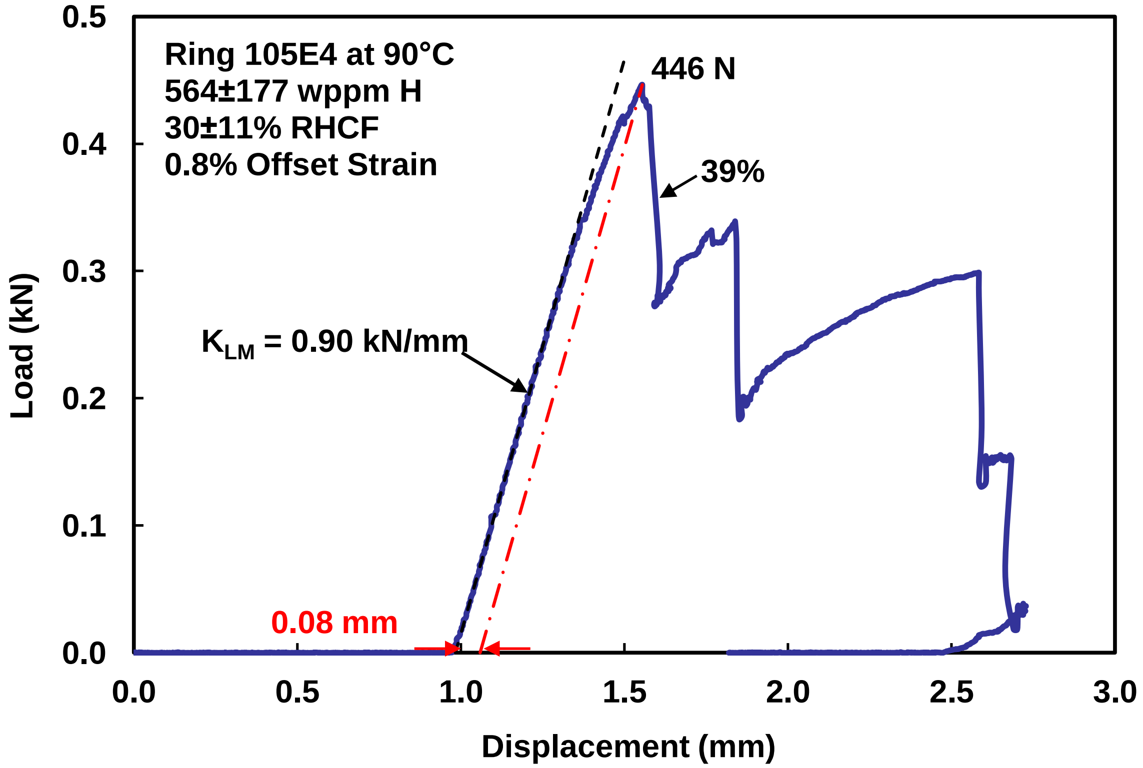

Figure 33: Load-displacement curve for HBU ZIRLO™ ring 105E4 tested at 5 mm/s and 90°C.

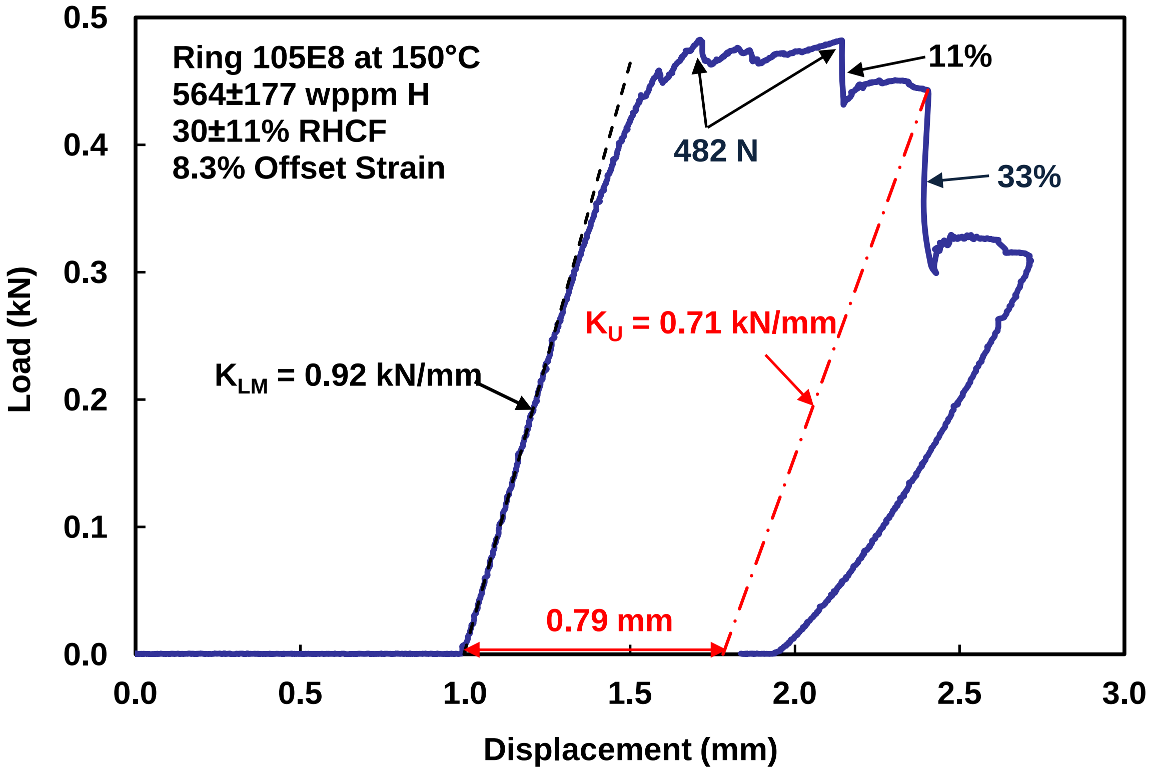

Figure 34: Load-displacement curve for HBU ZIRLO™ ring 105E8 tested at 5 mm/s and 150°C.

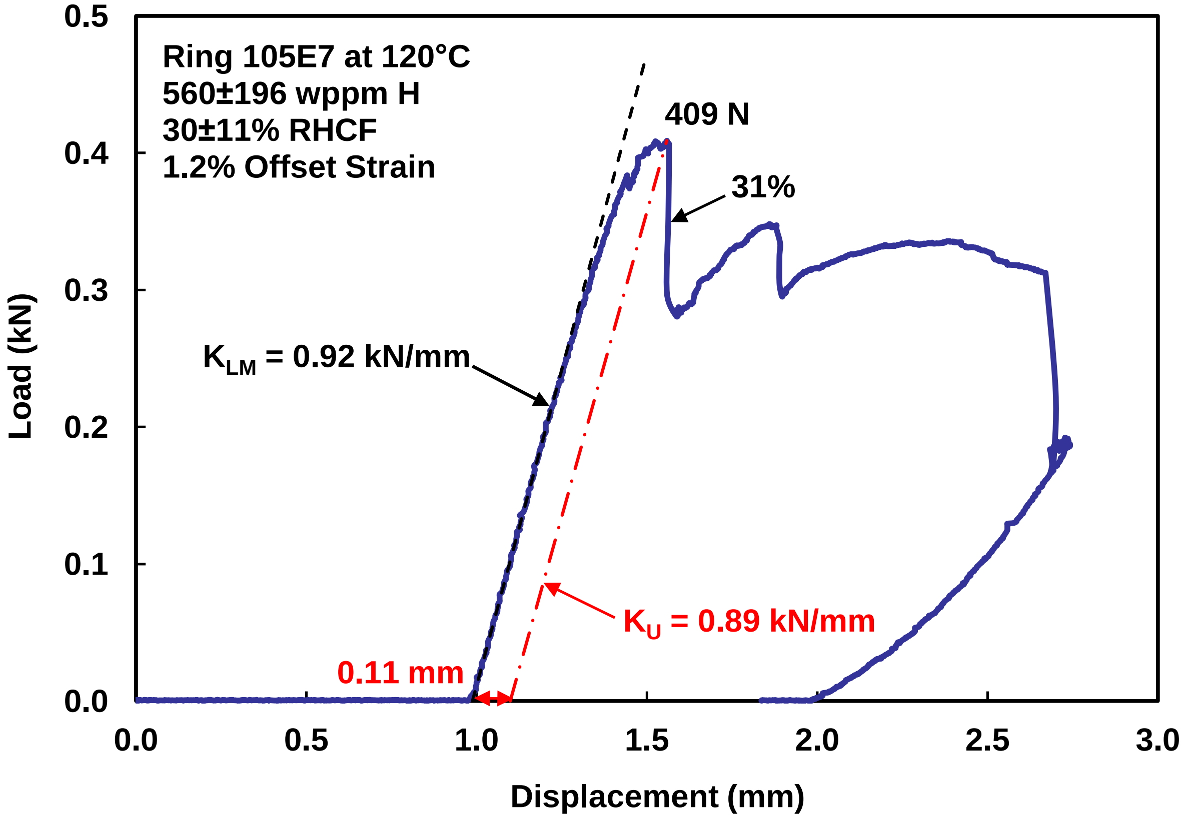

Figure 35: Load-displacement curve for HBU ZIRLO™ ring 105E4 tested at 5 mm/s and 120°C.

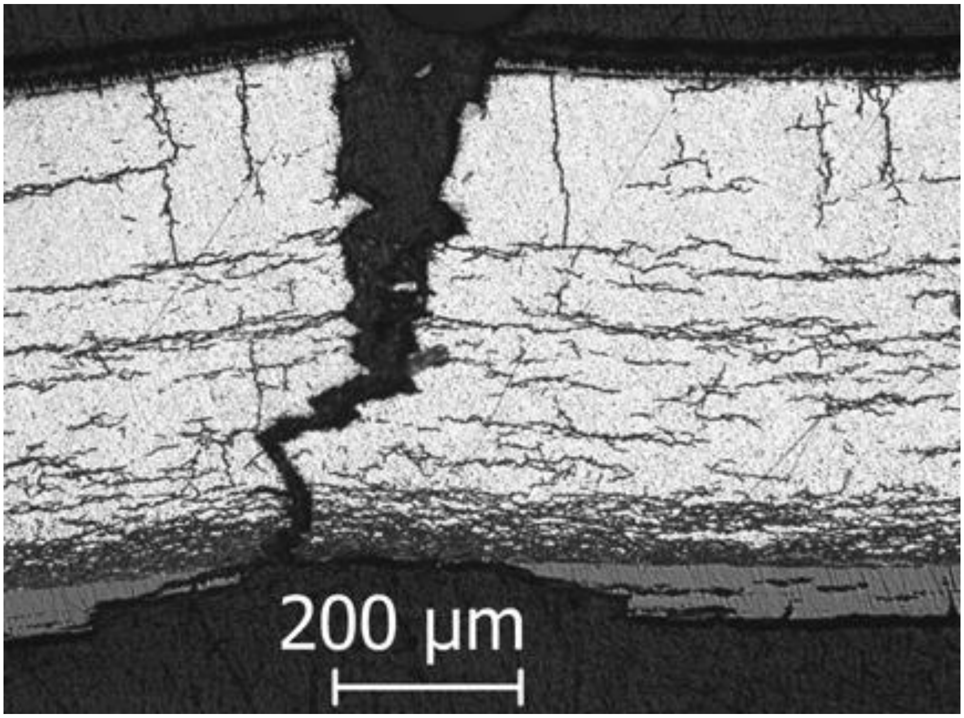

Figure 36: Major crack observed at 6 o'clock position of ring 105E7 mid-span.

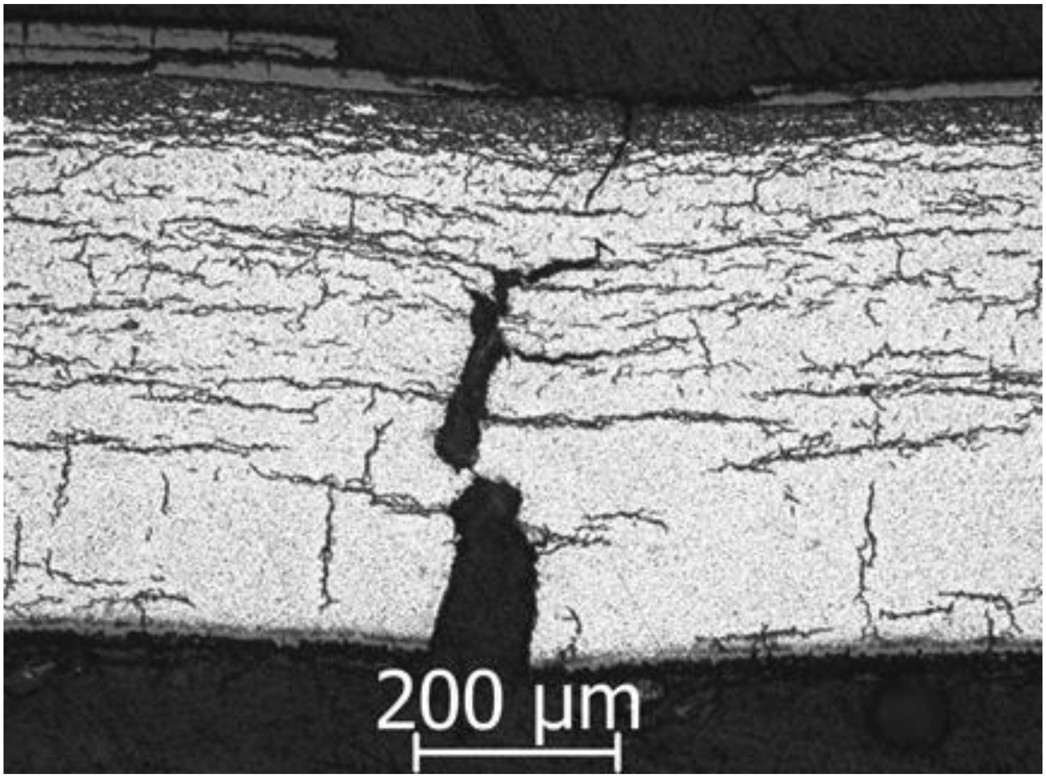

Figure 37: Crack observed at 12 o'clock position of ring 105E7 mid-span.

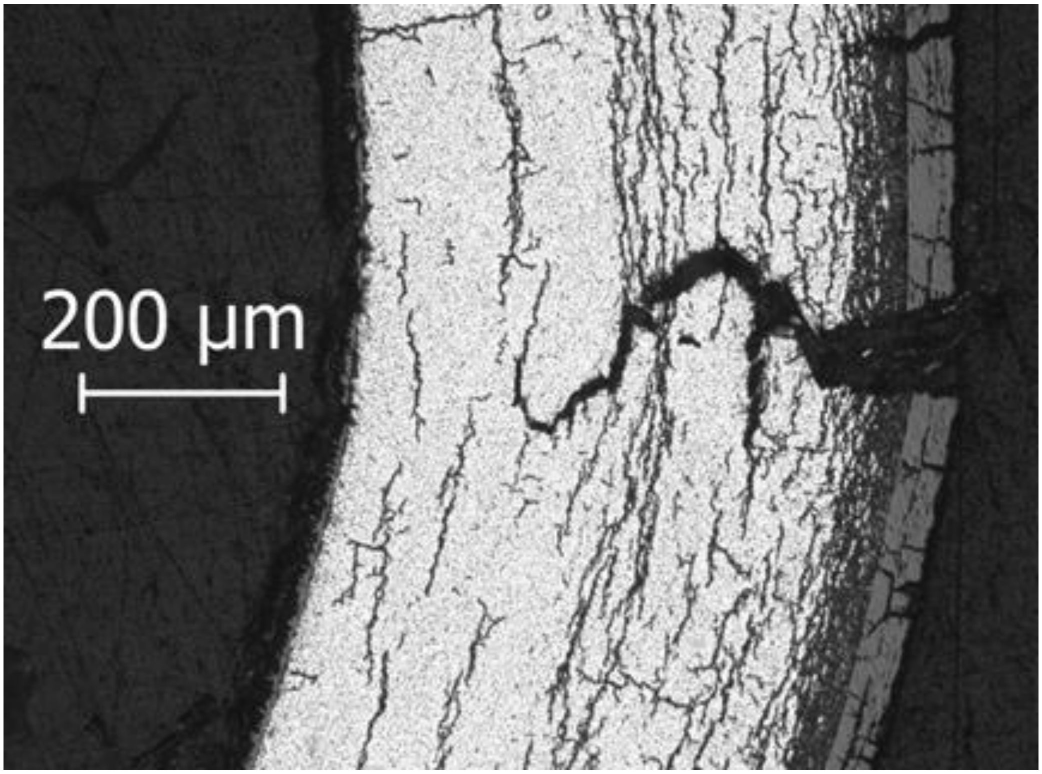

Figure 38: Major crack observed at 3 o'clock position of ring 105E7 mid-span.

For the 4th test, it was desirable to choose a temperature at which the ring would exhibit ductility (i.e., offset strain ≥2% prior to >50% wall cracking). As the HBU ZIRLO™ exhibited brittle behavior at 120°C and high ductility at 150°C, the decision was made to conduct the 4th test at the intermediate temperature of 135°C. The anticipated offset strain was >2% and <8%. The results were quite surprising as the load-displacement curve (see Fig. 39) for the 135°C test exhibited no load drops through 1.7-mm displacement. The offset displacement was about 12%, which was higher than the offset displacement at 150°C. The ring was sub-sectioned into two samples: one for hydrogen determination and one for metallographic examination to determine if any cracks had formed and to determine the RHCF (37±8%). Both the hydrogen content and the RHCF were consistent with values determined for the 105E rodlet. It is unlikely that the increase of offset strain from 1.2% to 11.9% was due to the 15°C increase in test temperature. Rather, the results suggest that the data scatter might be larger than originally anticipated. The metallographic image shown in Fig. 40 was also a surprise as it revealed that a crack had grown at the 6:30 o'clock position from the inner surface through a significant fraction of the cladding wall. The crack width was relatively small suggesting that crack growth had occurred at higher displacements (e.g., during the gradual 12% load drop from 478 N to 423 N). If the crack was continuous in the axial direction, a large load drop would have been observed. The results imply that the crack was a partial-wall crack with respect to the axial direction and the crack extension in the axial direction was small, relative to the length of the sample.

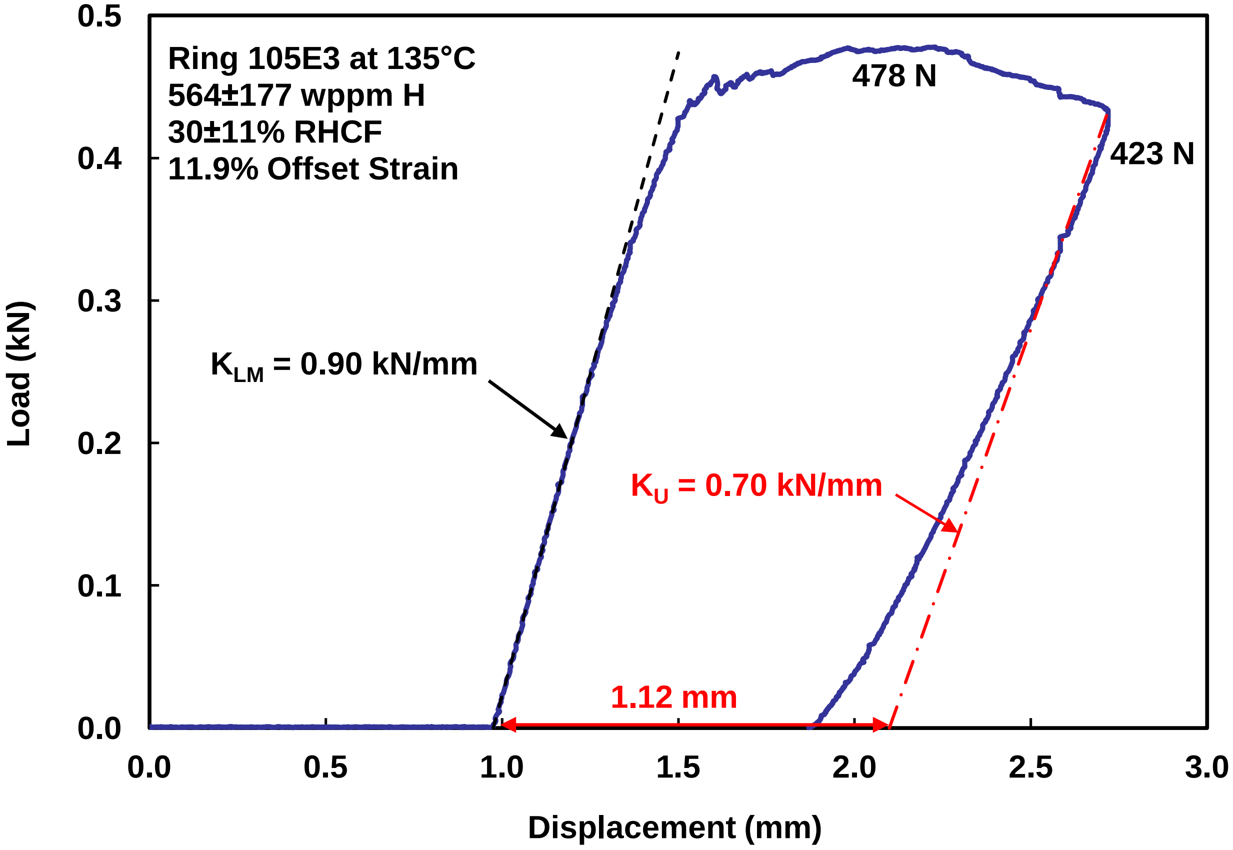

Figure 39: Load-displacement curve for HBU ZIRLO™ ring 105E7 tested at 5 mm/s and 135°C.

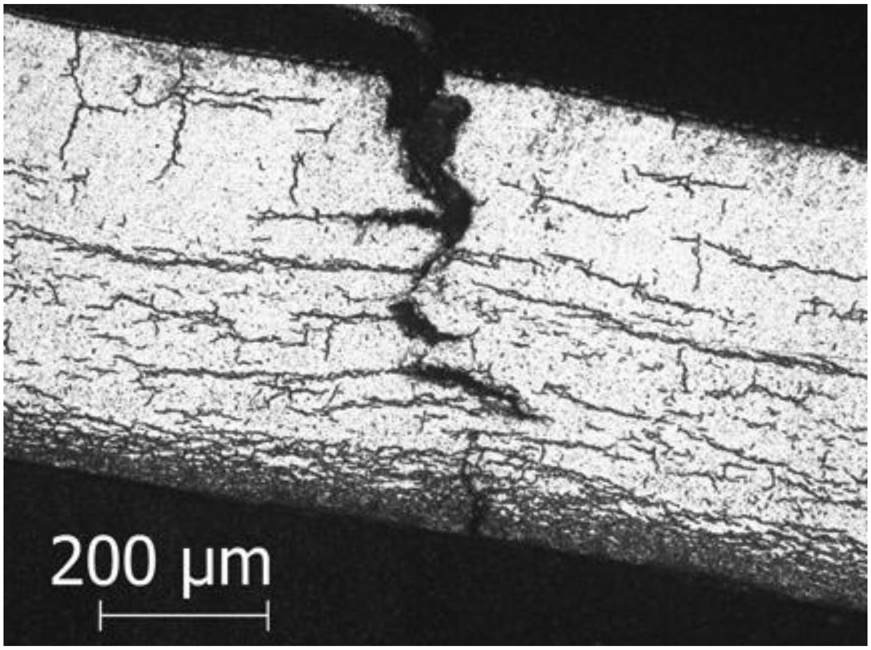

Figure 40: Crack observed at 6:30 o'clock position of ring 105E3 mid-span.

For rodlet 105F samples, RCTs were conducted at 120°C (F8), 135°C (F3), and 150°C (F4 and F7). Figures 41 and 42 show the load-displacement curves for tests conducted at 120°C and 135°C, respectively. At 120°C, the offset strain preceding the 41% load drop was 2%, which indicated borderline ductility. At 135°C, the offset strain was 1.1% preceding the 43% load drop, which indicated embrittlement. Figure 43 shows the results of the first test conducted at 150°C. Although minor load drops were observed prior to the 40% load drop, the offset strain was determined to be 6.4% just prior to the 40% load drop. Another significant load drop occurred at the higher displacement, which generally indicates the initiation and propagation of additional cracks, as well as the extension of the first crack. Figure 44 shows that extensive cracking occurred at the 12 o'clock orientation. The maximum crack opening at the initiation point (inner surface) was only 45 µm, which suggests that crack initiation and propagation occurred at an intermediate-to-high displacement level. Figure 46 shows the crack at the 2:30 o'clock orientation, which propagated from the outer surface (hydride rim) to about 80% of the wall thickness. The maximum crack width was 70 µm, which again indicates that crack propagation occurred at an intermediate-to-high displacement level. Although it is not clear which of these cracks occurred first, the metallographic results do support that crack propagation through >50% of the cladding wall occurred after significant offset strain had accumulated.

Load-displacement results for the 2nd test conducted at 150°C are shown in Fig. 47. These results were difficult to interpret because some minor cracking occurred during the load increase prior to the load reaching the maximum anticipated value (≈430 N). Two relatively small load drops totaling 25% occurred after the maximum load of 322 N was achieved. Although a 25% load drop is considered marginal with regard to >50% wall cracking, the total load drop would have been 35% relative to the anticipated peak load. Thus, the ductility was determined by unloading at the 2nd peak prior to the load drop to 281 N. This approach gave an offset strain of 2.9%, which was lower than expected. Figures 48 and 49 show the cracks that developed at 12 and 6 o'clock.

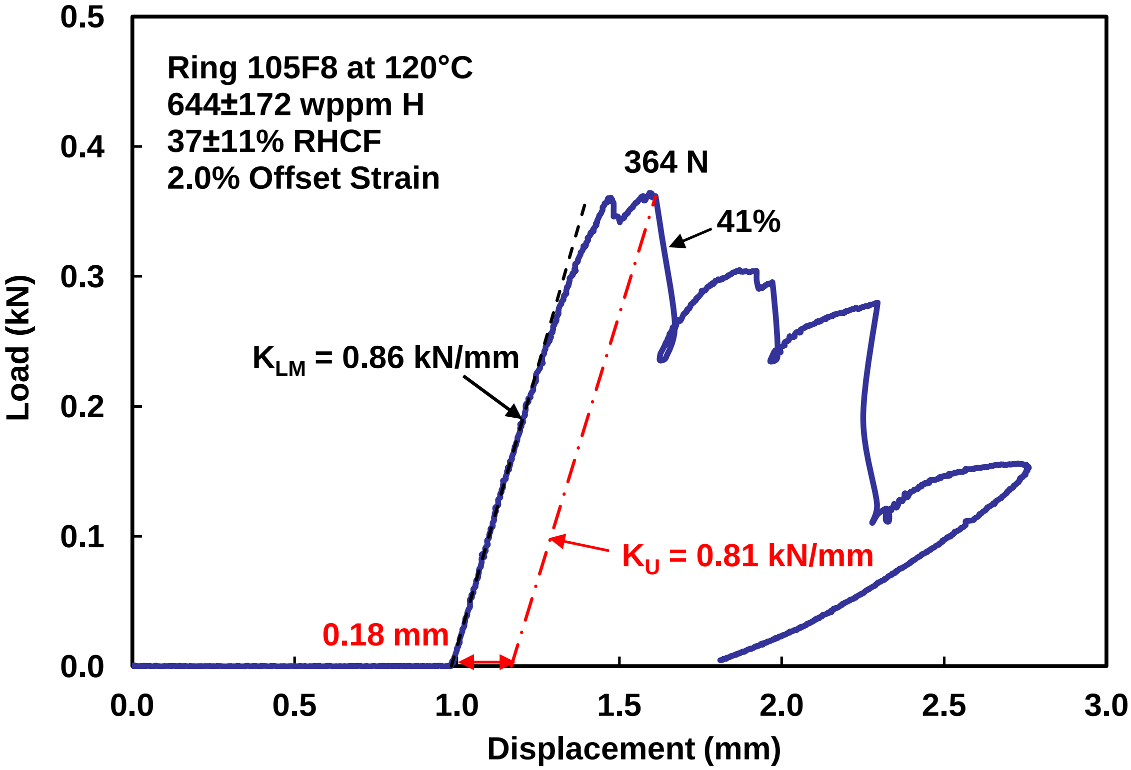

Figure 41: Load-displacement curve for HBU ZIRLO™ ring 105F8 tested at 5 mm/s and 120°C.

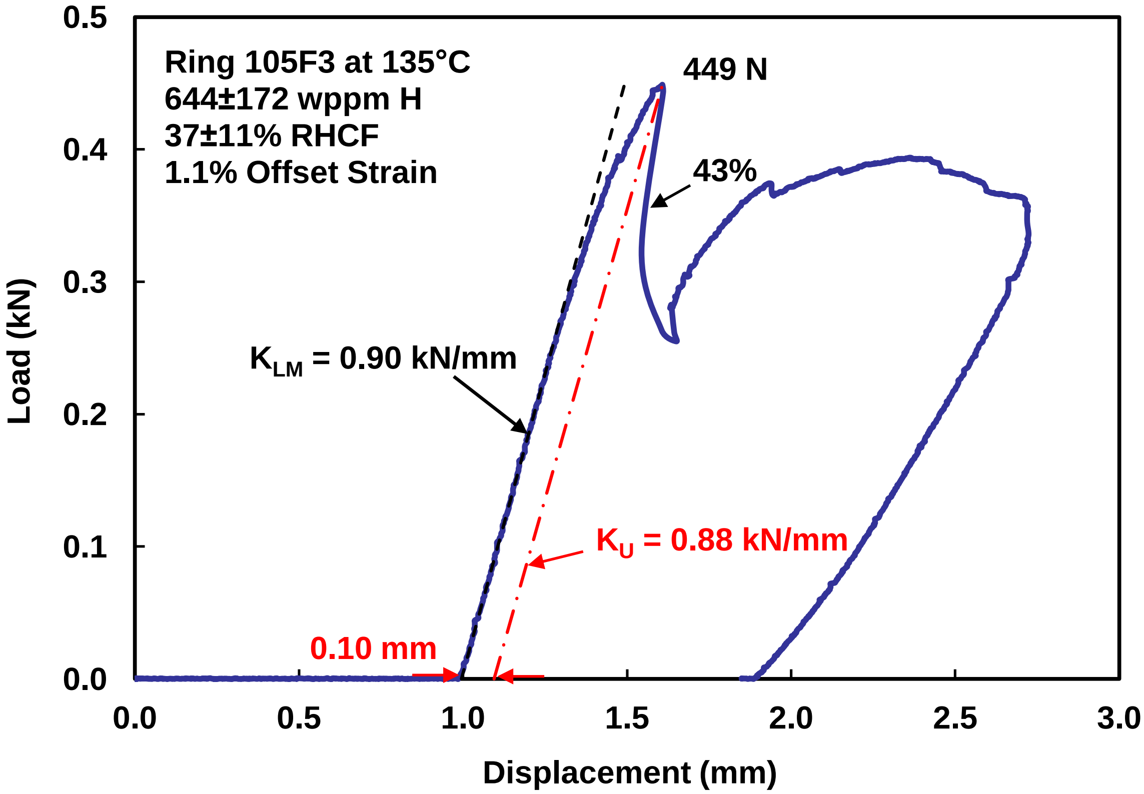

Figure 42: Load-displacement curve for HBU ZIRLO™ ring 105F3 tested at 5 mm/s and 135°C.

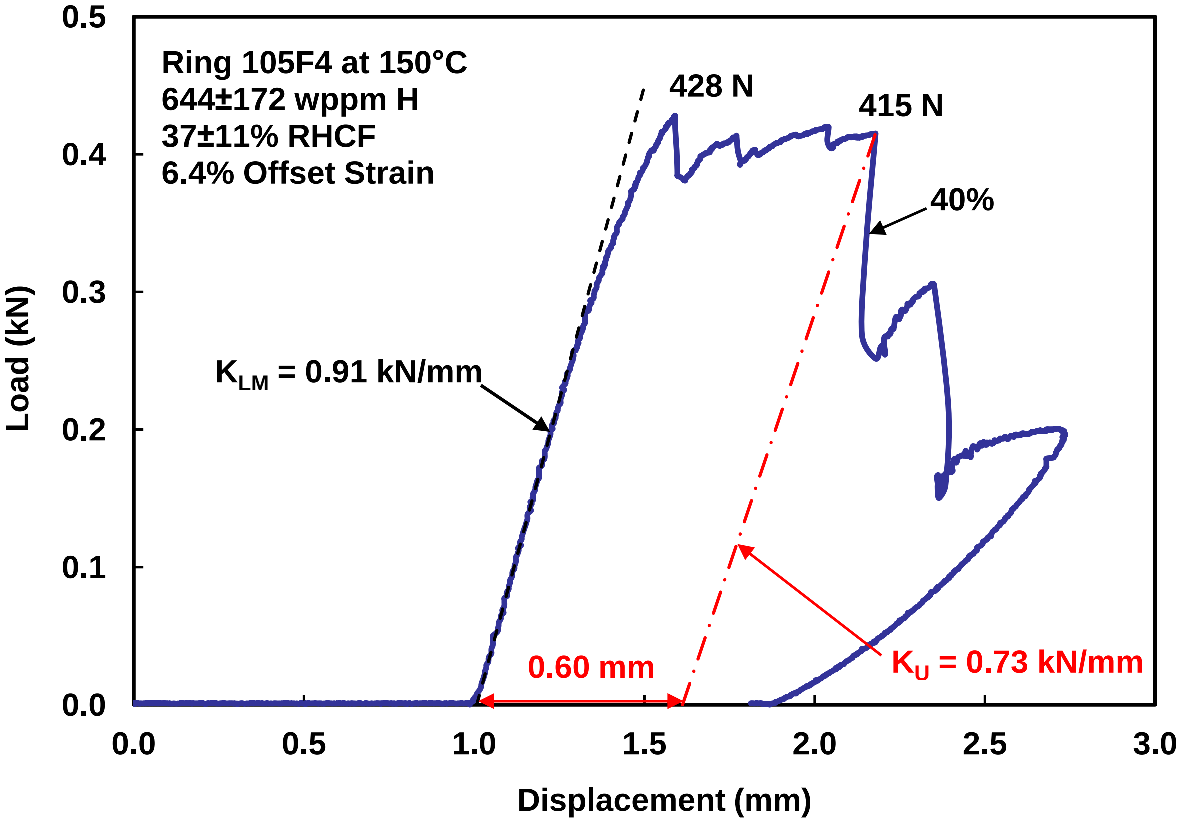

Figure 43: Load-displacement curve for HBU ZIRLO™ ring 105F4 tested at 5 mm/s and 150°C.

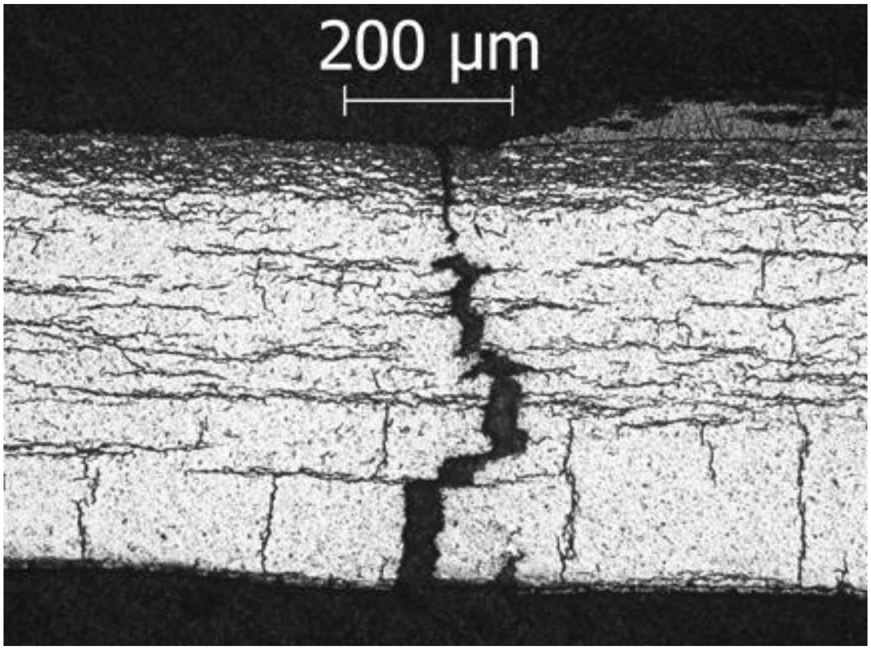

Figure 44: Crack observed at 12 o'clock position of ring 105F4 mid-span.

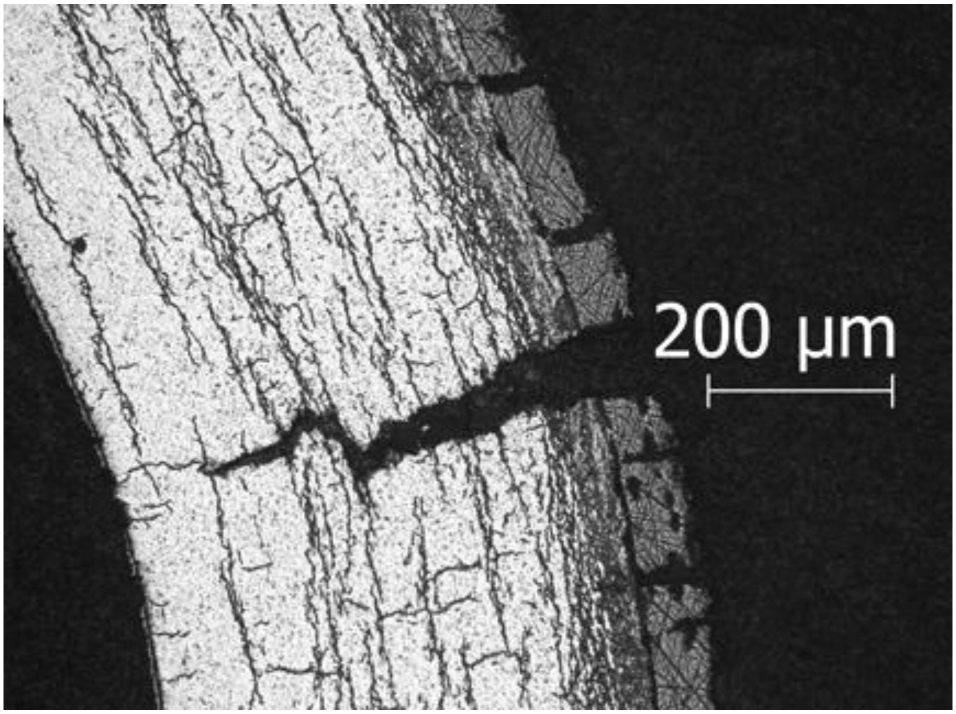

Figure 45: Crack observed at 2:30 o'clock position of ring 105F4 mid-span.

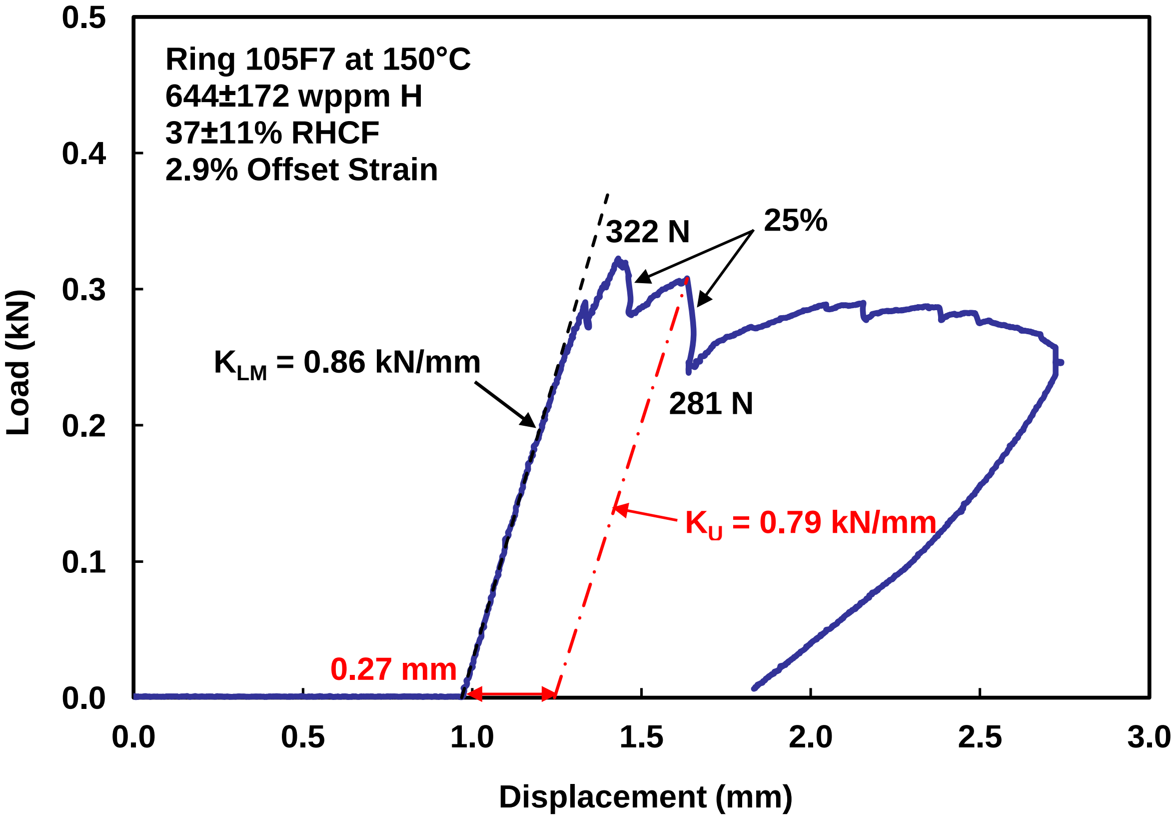

Figure 46: Load-displacement curve for HBU ZIRLO™ ring 105F7 tested at 5 mm/s and 150°C.

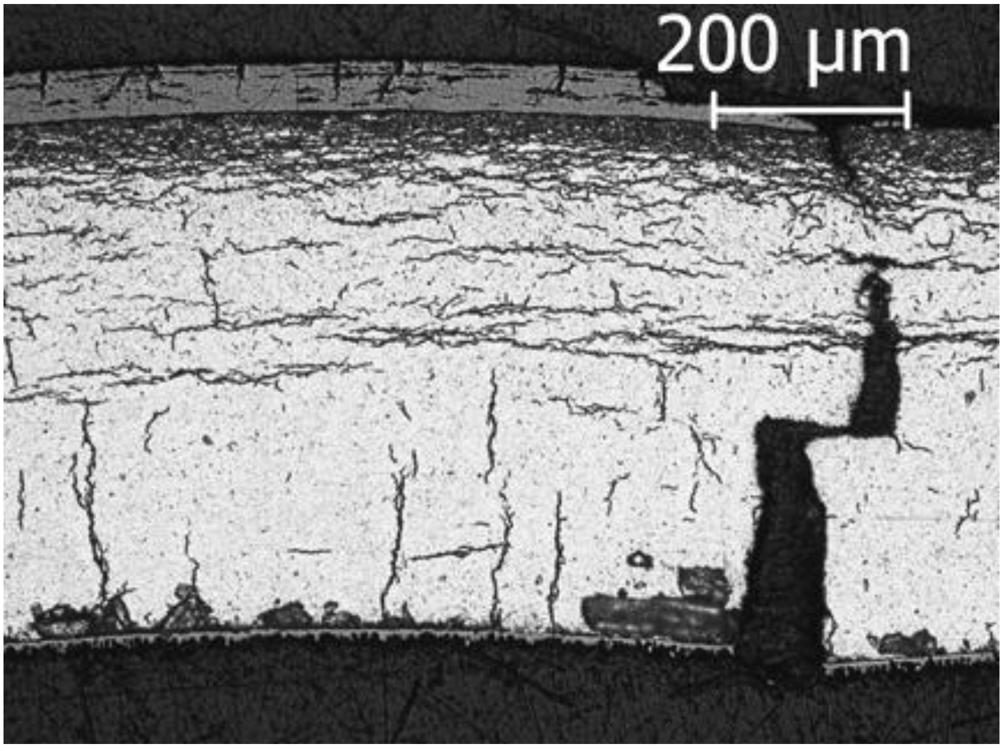

Figure 47: Crack observed at 12 o’clock position of ring 105F7 mid-span.

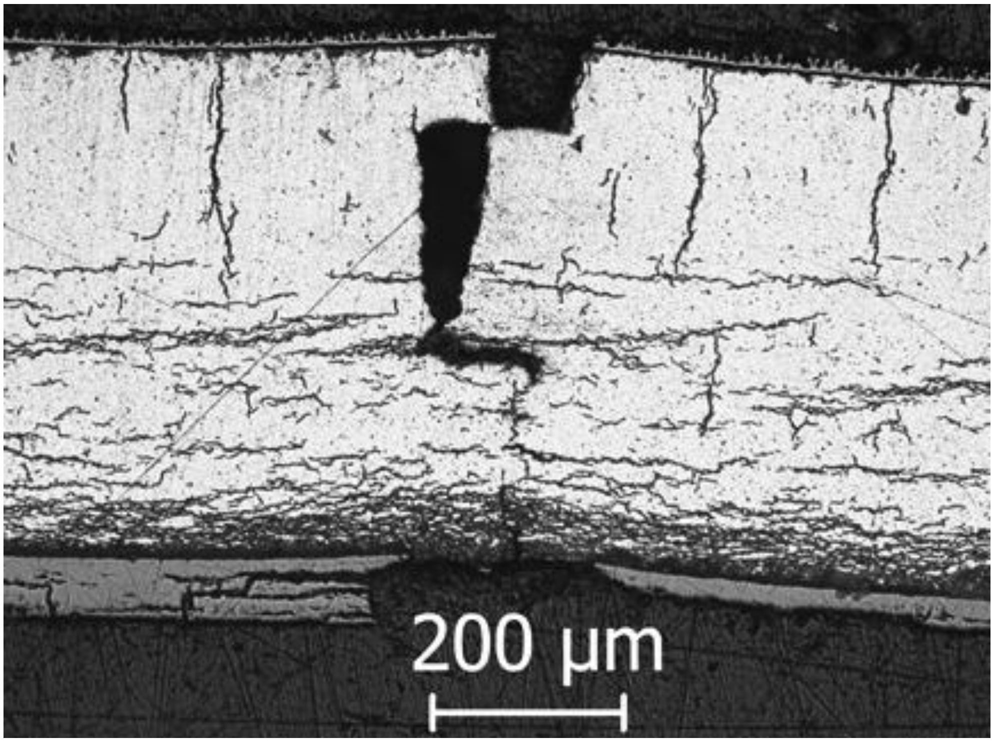

Figure 48: Crack observed at 6 o’clock position of ring 105F7 mid-span.

4.2.3 Summary of RCT Results for HBU ZIRLO™

Table 3 summarizes the results of RCTs and post-RCT characterization for rodlets 105E (3 cycles) and 105F (1 cycle) following RHT at a peak temperature of 350°C. As no significant effects of cycling were observed on the extent of radial hydride precipitation and on radial-hydride embrittlement, the results were combined to determine the DBTT for peak RHT hoop stresses of 93 to 94 MPa. Figure 49 shows the offset strain vs. RCT temperature for the two rodlets with a 350°C peak RHT temperature, as well as previous results for comparable tests conducted with 1-cycle and 3-cycle rodlets with 400°C peak RHT temperature. The combined data set indicates a DBTT of ≈125°C for rodlets subjected to 350°C and 93–94 MPa peak RHT conditions as compared to a DBTT of 23°C for rodlets subjected to a higher peak RHT temperature (400°C) and slightly lower peak RHT hoop stresses (88–89 MPa). The results suggest that the extent of radial-hydride precipitation and embrittlement is very sensitive to peak RHT hoop stress and relatively insensitive to peak RHT temperature within the range of 350°C to 400°C.

Table 3 Summary of RCT and post-RCT characterization results for HBU ZIRLO™ rodlets following RHT at 350°C peak cladding temperature and peak hoop stresses of 93 to 94 MPa.

Rodlet	Cycles	Ring	C_H, wppm	RHCF, %	RCT T, °C	Offset Strain, %
105E	3		564±177	30±11	–	–
		4	–	–	90	0.8
		7	569±148	25±10	120	1.2
		3	568±200	37±8	135	11.0
		8	–	–	150	8.3
105F™	1		644±172	37±11	–	–
		8	–	–	120	2.0
		3	–	–	135	1.1
		4	625±199	37±12	150	6.4
		7	648±176	38±13	150	2.9

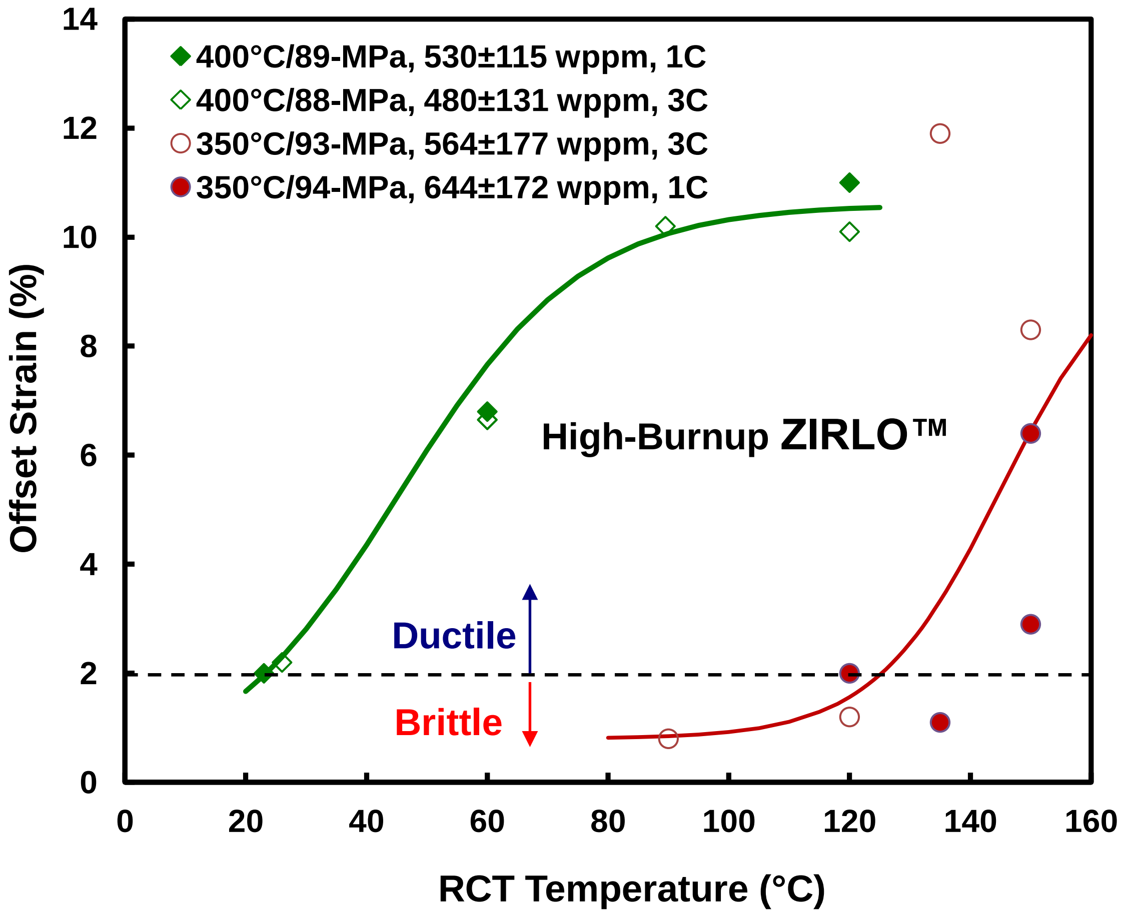

Figure 49: Comparison of RCT results for rodlets subjected to peak RHT temperatures of 350°C and 400°C and peak hoop stresses in the range of 88 MPa to 94 MPa.

Page intentionally blank

5. DISCUSSION AND SUMMARY

Effects of Multiple Drying Cycles on DBTT

For peak hoop stresses in the range of 88 MPa to 94 MPa, 3-cycle-drying results were comparable to 1-cycle drying results at peak RHT temperatures of 350°C and 400°C. No effects of multiple drying cycles were observed for HBU ZIRLO™ tested with these ranges of peak RHT temperatures and hoop stresses.

Effects of Decreasing the Peak Drying-Storage Temperature from 400°C to 350°C

The hydrogen solubility decreases by 80 wppm (from about 206 wppm to 126 wppm) with a decrease in temperature from 400°C to 350°C. Thus, less hydrogen is available to redistribute and precipitate as radial hydrides. However, and surprisingly, current and previous results for HBU ZIRLO™ indicate that the effective lengths of radial hydrides are just as long during precipitation from 350°C as they are during precipitation from 400°C. Consequently, no decrease in DBTT was observed with the decrease in peak RHT temperature. It is likely that peak temperatures <350°C (e.g., 325°C) would allow higher peak hoop stresses without increasing the DBTT. For temperatures ≤325°C, the hydrogen solubility decreases to <100 wppm. At low enough hydrogen levels, there should be greater discontinuity in hydride platelets in the axial direction, improvement in ductility, and decrease in the DBTT.

Effects of Peak Drying Storage Hoop Stress on the DBTT

Previous results indicate that the DBTT for HBU ZIRLO™ decreased dramatically from about 122°C to 23°C with a decrease in peak RHT hoop stress at 400°C from about 110 MPa to about 90 MPa. The current tests conducted at 350°C and hoop stresses of about 90 MPa (93 MPa and 94 MPa) are equivalent to about 100 MPa at 400°C. The DBTT determined from these tests was ≈120°C. These results indicate HBU ZIRLO™ would show a sharp increase in DBTT with a modest increase in peak hoop stress from about 90 MPa to 100 MPa. Additional tests should be conducted at 400°C-equivalent hoop stresses of about 95 MPa to confirm this sharp transition. The tests should be conducted at more realistic RHT temperatures of ≤350°C.

Effects of Circumferential Hydrides on the Ductility of As-Irradiated Cladding

The HBU ZIRLO™ and Zry-4 used in this test program had average hydrogen contents of 300 wppm to 650 wppm. The hydrides observed for these CWSRA materials were oriented in the circumferential direction. For average hydrogen contents >600 wppm, measurements of one-third and quarter arc segments at particular axial locations indicated large circumferential variations in hydrogen content (as much as ±200 wppm standard deviation) with peak local values >800 wppm. The HBU ZIRLO™ test samples came from fuel rods irradiated in commercial PWRs at a relatively high power and temperature drop across the cladding wall. These operating conditions resulted in a very dense hydride rim at the outer cladding surface just below the coolant-side oxide layer. The effects of increased hydrogen content for this material with increased axial elevation along fuel rods were simply to increase the hydride rim thickness (to as much as 80 µm) without changing the hydrogen content (≈135 wppm) below the hydride rim. In response to RCT loading, multiple cracks developed in the hydride rim near the 3 and 9 o’clock regions relative to loading applied at the 12 o’clock position and support at the 6 o’clock position. However, these cracks were within the range of 5% to 20% of the cladding wall thickness and generally did not propagate into the low hydrogen-content region. As such, the HBU ZIRLO™ exhibited high RCT ductility values ≥6% at temperatures as low as RT and for a wide range of displacement rates

(0.05 mm/s to 50 mm/s). The high ductility of the HBU ZIRLO™ is likely associated with the operating conditions rather than with the material itself.

In contrast, the HBU Zry-4 material used in this test program came from fuel rods irradiated in commercial PWRs at a relatively low power and with a low temperature drop across the cladding wall. The distribution of circumferential hydrides was quite different than what was observed for HBU ZIRLO™. The hydride rim at the oxide metal interface was less dense and circumferential hydrides were observed to extend as far as the cladding mid-radius with the spacing between hydrides increasing with increased depth into the cladding. Cracking in such material was observed to initiate at relatively low displacements and corresponding offset strains (<2%). However, crack propagation was much slower and less severe than what has been observed in HBU cladding with radial hydrides due to the fact that circumferential hydrides are parallel to the global hoop stress field. By conducting load-interrupt tests following load drops of 20% to 30% and post-RCT metallographic examinations, the following sequence of cracking was observed: (a) relatively short radial cracks emanating from the outer cladding surface though the denser part of the hydride rim, (b) cracking along circumferential hydrides ahead of the crack front, and (c) plastic flow of the Zry-4 metal between the cracked circumferential hydrides followed by ductile cracking (45° from the radius) of the Zry-4 between the cracked circumferential hydrides. The series of small load drops followed by load increases was apparently due to the relatively ductile cladding metal between the circumferential hydrides. The load-interrupt tests also allowed direct measurement of the permanent decrease in cladding diameter and the corresponding increase in permanent strain for cracks extending to <50% of the cladding wall. Using this approach, it was found that permanent strains were 2.8±0.7% (as compared to the 1% ductility limit for these strains). Thus, even with high hydrogen content, as-irradiated HBU Zry-4 retained respectable ductility over a wide range of displacement rates (0.05 mm/s to 50 mm/s) and temperatures (20°C to 120°C). It is anticipated that HBU ZIRLO™ irradiated under the same conditions as the HBU Zry-4 used in this test program would have a similar broader and less dense hydride rim and would still have permanent strains in the ductile regime (>1%).

Effects of Etching Time on Appearance of Hydrides

One post-RCT HBU ZIRLO™ surface was etched for a time corresponding to what was considered optimum for this material. The sample was re-etched for various time increments and intermittently imaged until the sample was clearly over-etched. Crack morphology remained the same, as well as the presence and lengths of hydrides, for the various degrees of etching. Within the range of etching times studied, the main effect of increasing the etching time was to increase the apparent thickness of the hydrides. Such thickness increases would not affect the lengths of radial hydrides, but it might affect the appearance of radial-circumferential hydride continuity, especially in 100X images. This study was conducted to add assurance that surfaces examined in detail for the presence of radial hydrides were not missing hydrides due to possible under-etching. This insensitivity to etching times used in the Argonne test program has now been confirmed.

Scatter in RCT Ductility Data

Test results for HBU ZIRLO™ following RHT at 350°C appeared to have more data scatter than test results conducted on the same material following RHT at 400°C. Some of this apparent data scatter may have been due to the difficulty encountered in interpreting load-displacement curves. The determination of ductility could be improved by conducting repeat tests including load-interrupt tests followed by direct measurement of permanent strain and by post-RCT metallographic examination—the same procedure used to conduct tests with as-irradiated HBU Zry-4.

Realistic Temperatures, EOL RIPs, and Cladding Hoop Stresses during Drying and Storage

During the early stages of this work, it was assumed that peak cladding hoop stresses during drying and storage could be in the range of 80 MPa to 160 MPa for PWR fuel rods. However, the upper bound of this range was based on conservative upper-bound cask thermal analyses and conservative fuel-vendor-determined internal pressure limits at full reactor power that would prevent cladding liftoff from the fuel. Members of the UFD Campaign have been working with Electric Power Research Institute (EPRI), fuel vendors, cask vendors, and the international community to determine realistic cladding temperatures during drying and storage, as well as more realistic EOL RIPs. To calculate the distribution of peak stresses in fuel rods during drying and storage, it is important to know EOL conditions for these fuel rods and realistic temperature profiles along fuel-rod lengths during drying and storage, especially in the plenum region of the HBU fuel rods where most of the gas resides. The work to collect data for PWR EOL RIPs is being coordinated by the Fuels-Internals Subcommittee (chaired by M.C. Billone of Argonne) of the EPRI-sponsored Extended Storage Collaboration Program (ESCP). This is a work in progress as much of the data needed is restricted (vendor proprietary or EPRI/vendor proprietary). The data collected to date indicate that peak hoop stresses during drying and storage are more likely to be in the range of 80 MPa to 110 MPa. However, the distribution (i.e., fraction of fuel rods above 80 MPa, 90 MPa, 100 MPa, etc.) remains unknown. Also, data collected to date are for “legacy” PWR fuel rods (mostly clad in Zry-4) irradiated in the 1980s and 1990s before the introduction of advanced cladding alloys (e.g., ZIRLO™, Optimized ZIRLO™, M5®), and before power increases and extended burnup were licensed and used by utilities. Also, the data set collected does not include fuel rods with burnable poisons inside the rods that release gases (e.g., He) through transmutations (products of neutron and B-10 reactions). The trend with advanced cladding alloys is decreasing axial growth, which would decrease EOL plenum volumes and increase EOL RIPs.

As shown in this report, radial-hydride-induced embrittlement is very sensitive to the peak cladding hoop stress during drying and storage. Whether or not it even occurs or to what extent it may occur depends on the distribution of EOL RIPs and the peak plenum temperature during drying and storage. In parallel to the Argonne test program, work is in progress to determine the distribution of EOL RIPs for PWR fuel rods by a combination of data collection and fuel-rod-simulation-code predications.

In addition to these efforts, experimental and analytical work is in progress within the UFD Campaign to determine realistic loads on cladding during normal conditions of transport. The data generated in the Argonne test program can be used to determine failure stresses and strains in response to hoop loading, which would then be used to compare measured and/or calculated stresses and strains to failure limits. The goal of this integrated approach is to assess cladding integrity during post-storage transportation, as well as possible retrieval of fuel assemblies following post-storage transport.

Page intentionally blank

REFERENCES

[1] Geelhood, K.J., W.G. Lusher, and C.E. Beyer, *PNNL Stress/Strain Correlation for Zircaloy*, Pacific Northwest National Laboratory Report PNNL-17700, July 2008.

[2] Nuclear Regulatory Commission, Interim Staff Guidance (ISG)-11, Revision 3, "Cladding Considerations for the Transportation and Storage of Spent Fuel," November 2003. ML033230335 at http://www.nrc.gov/reading-rm/adams.html

[3] Billone, M.C., T.A. Burtseva, and Y. Yan, *Ductile-to-Brittle Transition Temperature for High-Burnup Zircaloy-4 and ZIRLO™ Cladding Alloys Exposed to Simulated Drying-Storage Conditions*, Argonne National Laboratory Report ANL-13/13, NRC ADAMS ML12181A238, Sept. 2012.

[4] Billone, M.C., T.A. Burtseva, and R.E. Einziger, "Ductile-to-Brittle Transition Temperature for High-Burnup Cladding Alloys Exposed to Simulated Drying-Storage Conditions," J. Nucl. Mater. **433**, 431–448 (2013).

[5] Billone, M.C., T.A. Burtseva, J.P. Dobrzynski, D.P. McGann, K. Byrne, Z. Han, and Y.Y. Liu, *Phase I Ring Compression Testing of High-Burnup Cladding*, FCRD-USED-2012-000039, Dec. 31, 2011.

[6] Billone, M.C., T.A. Burtseva, and Y.Y. Liu, *Baseline Studies for Ring Compression Testing of High-Burnup Fuel Cladding*, Argonne National Laboratory Report ANL-12/58, FCRD-USED-2013-000040, Nov. 23, 2012.

[7] Billone, M.C., T.A. Burtseva, and Y.Y. Liu, "Effects of Drying and Storage on High-Burnup Cladding Ductility," Proc. IHLRWMC, Albuquerque, NM, April 28–May 2, 2013, Paper 6973, 1106–1113 (2013).

[8] Billone, M.C., T.A. Burtseva, and Y.Y. Liu, "Baseline Properties and DBTT of High-Burnup PWR Cladding Alloys," Proc. PATRAM 2013, San Francisco, CA, August 18–23, 2013.

[9] Billone, M.C., T.A. Burtseva, Z. Han, and Y.Y. Liu, *Embrittlement and DBTT of High-Burnup PWR Fuel Cladding Alloys*, Argonne National Laboratory Report ANL-13/16, FCRD-UFD-2013-000401, Sept. 30, 2013.

[10] Billone, M.C., T.A. Burtseva, Z. Han, and Y.Y. Liu, *Effects of Multiple Drying Cycles on High-Burnup PWR Cladding Alloys*, Argonne National Laboratory Report ANL-14/11, FCRD-UFD-2014-000052, Sept. 26, 2014.

[11] Aomi, M., T. Baba, T. Miyashita, K. Kaminura, T. Yasuda, Y. Shinohara, and T. Takeda, "Evaluation of Hydride Reorientation and Mechanical Properties for High-Burnup Fuel-Cladding Tubes in Interim Dry Storage," J. ASTM Intl., JAI101262 (2008). www.astm.org

[12] Cuta, J.M., S.R. Suffield, J.A. Fort, and H.E. Adkins, *Thermal Performance Sensitivity Studies in Support of Material Modeling for Extended Storage of Used Nuclear Fuel*, Pacific Northwest National Laboratory Report PNNL-22646, FCRD-UFD-2013-000257, Sept. 27, 2013.

[13] Kearns, J.J., "Terminal Solubility and Partitioning of Hydrogen in the Alpha Phase of Zirconium, Zircaloy-2 and Zircaloy-2," J. Nucl. Mater. **22**, 292–303, 1967.

[14] Kammenzind, B.F., D.G. Franklin, H.R. Peters, and W.J. Duffin, “Hydrogen Pickup and Redistribution in Alpha-Annealed Zircaloy-4,” *Zirconium in the Nuclear Industry: 11th Intl. Symp.*, ASTM STP 1295, E.R. Bradley and G.P. Sabol, Eds., ASTM, pp. 338–370, 1996.

[15] McMinn, A., E.C. Darby, and J.S. Schofield, “The Terminal Solid Solubility of Hydrogen in Zirconium Alloys, *Zirconium in the Nuclear Industry: 12th Intl. Symp.*, ASTM STP 1354, G.P. Sabol and G.D. Moan, Eds., ASTM, pp. 173–195, 2000.

[15] Chu, H.C., S.K. Wu, and R.C. Kuo, “Hydride Reorientation in Zircaloy-4 Cladding,” J. Nucl. Mater. **373**, 319–327, 2008.

APPENDIX A METALLOGRAPHIC IMAGES OF ZIRLO™ CROSS SECTION FROM ONE-CYCLE 350°C TEST SAMPLE 105F6

Page intentionally blank

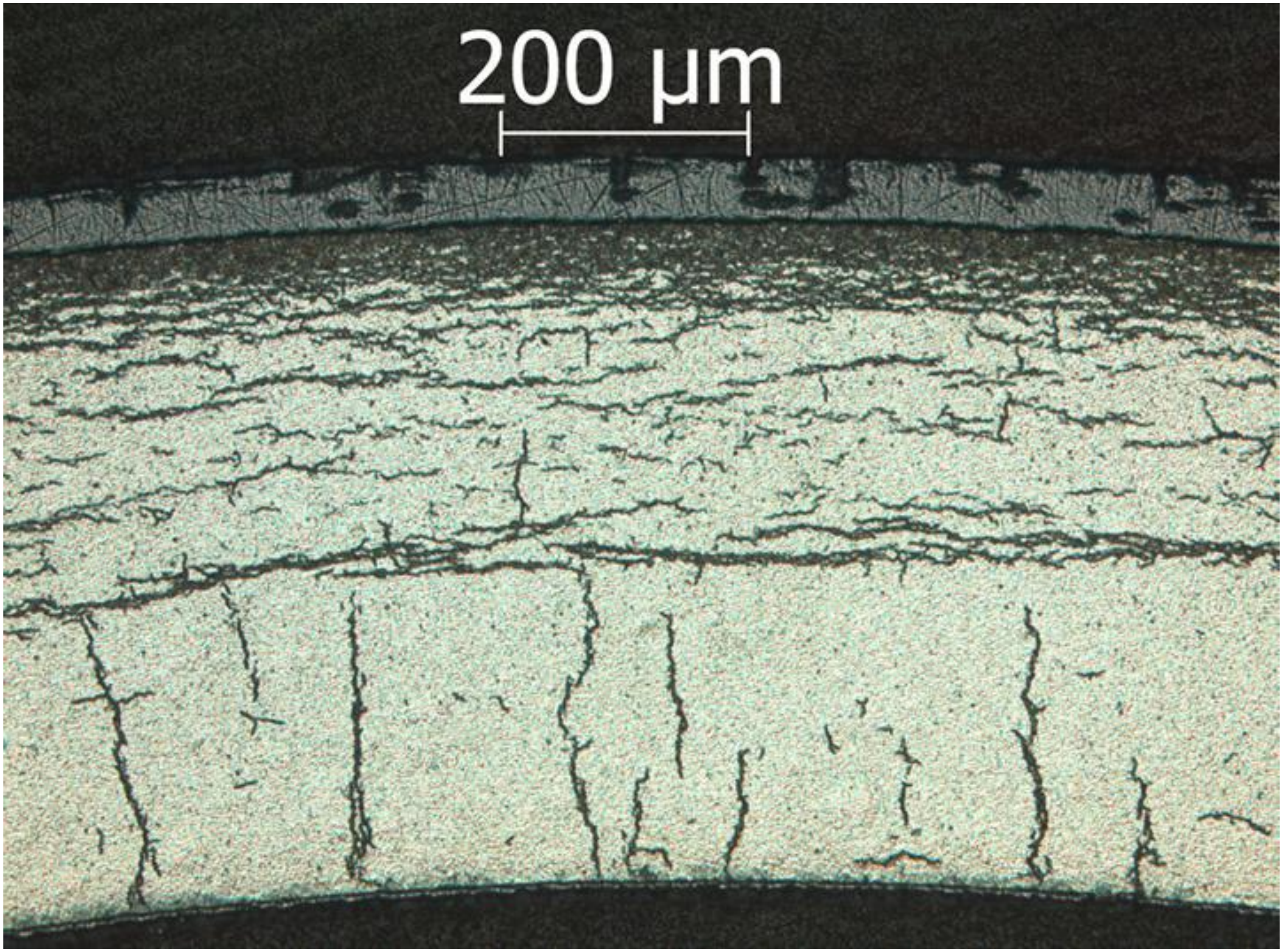

Figure A.1: Image (100X) of ZIRLO™ sample 105F6 in Area 1 (12:00 o’clock orientation) from 1-cycle 350°C rodlet.

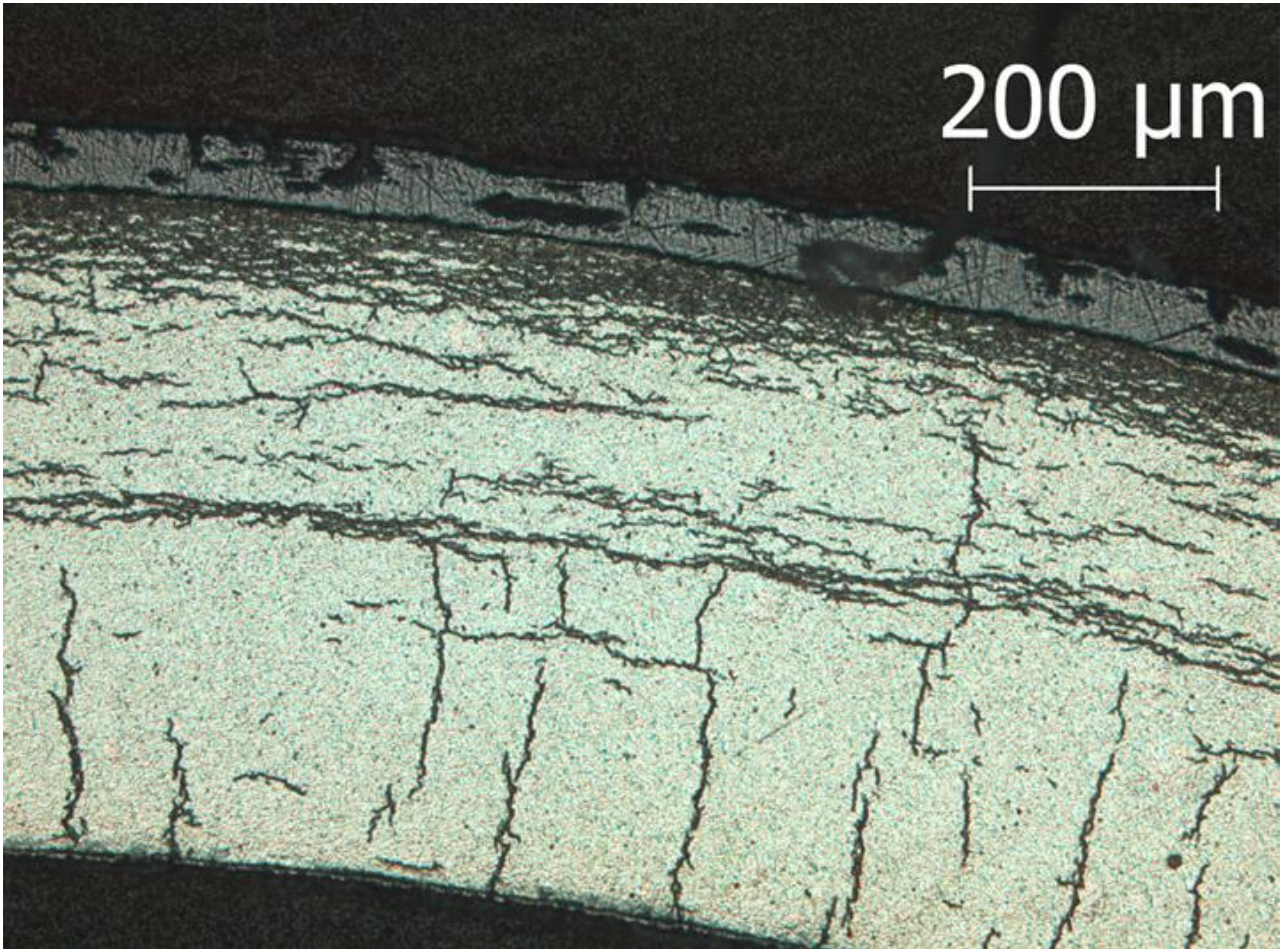

Figure A.2: Image (100X) of ZIRLO™ sample 105F6 in Area 2 from 1-cycle 350°C rodlet.

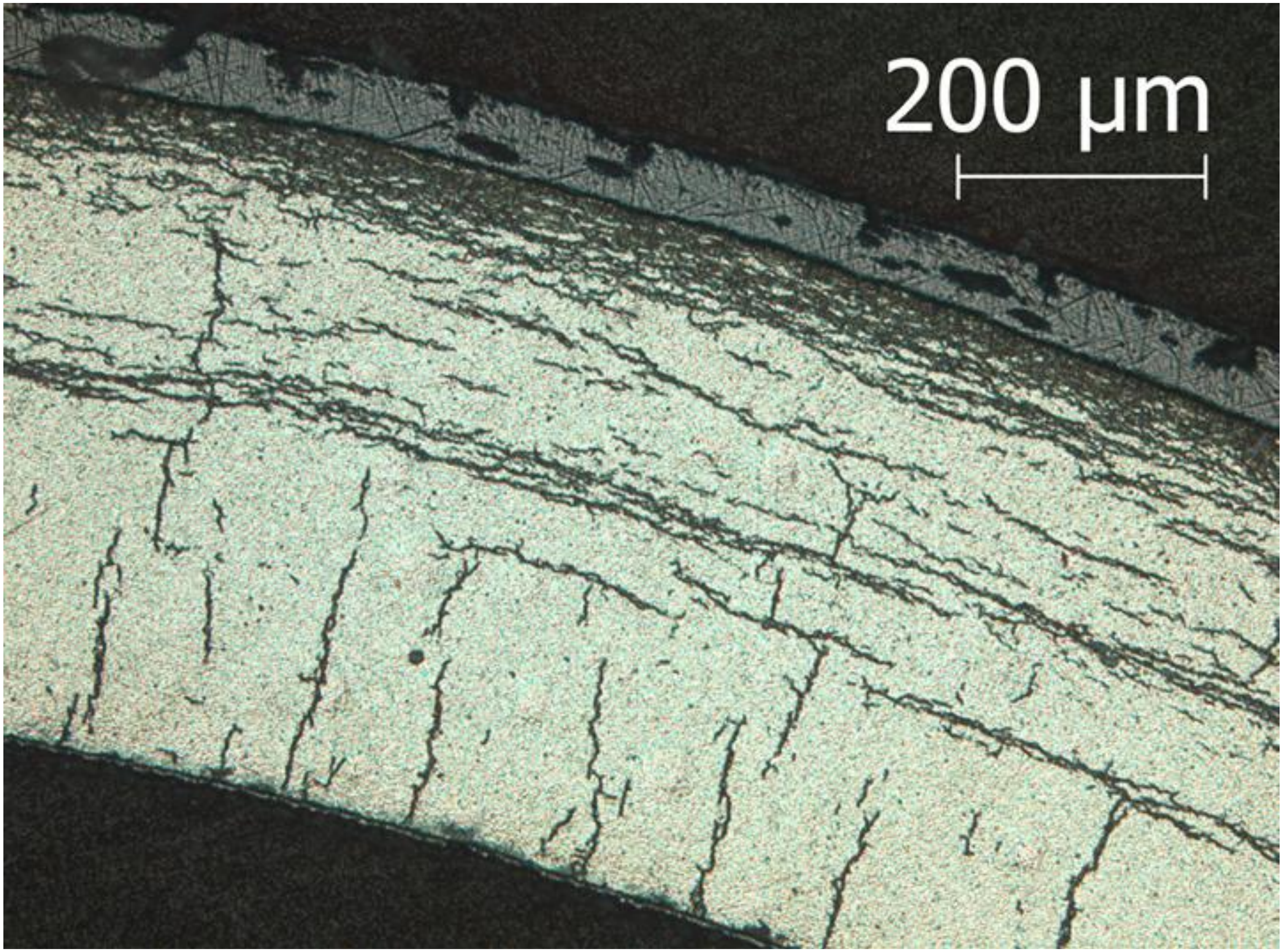

Figure A.3: Image (100X) of ZIRLO™ sample 105F6 in Area 3 from 1-cycle 350°C rodlet.

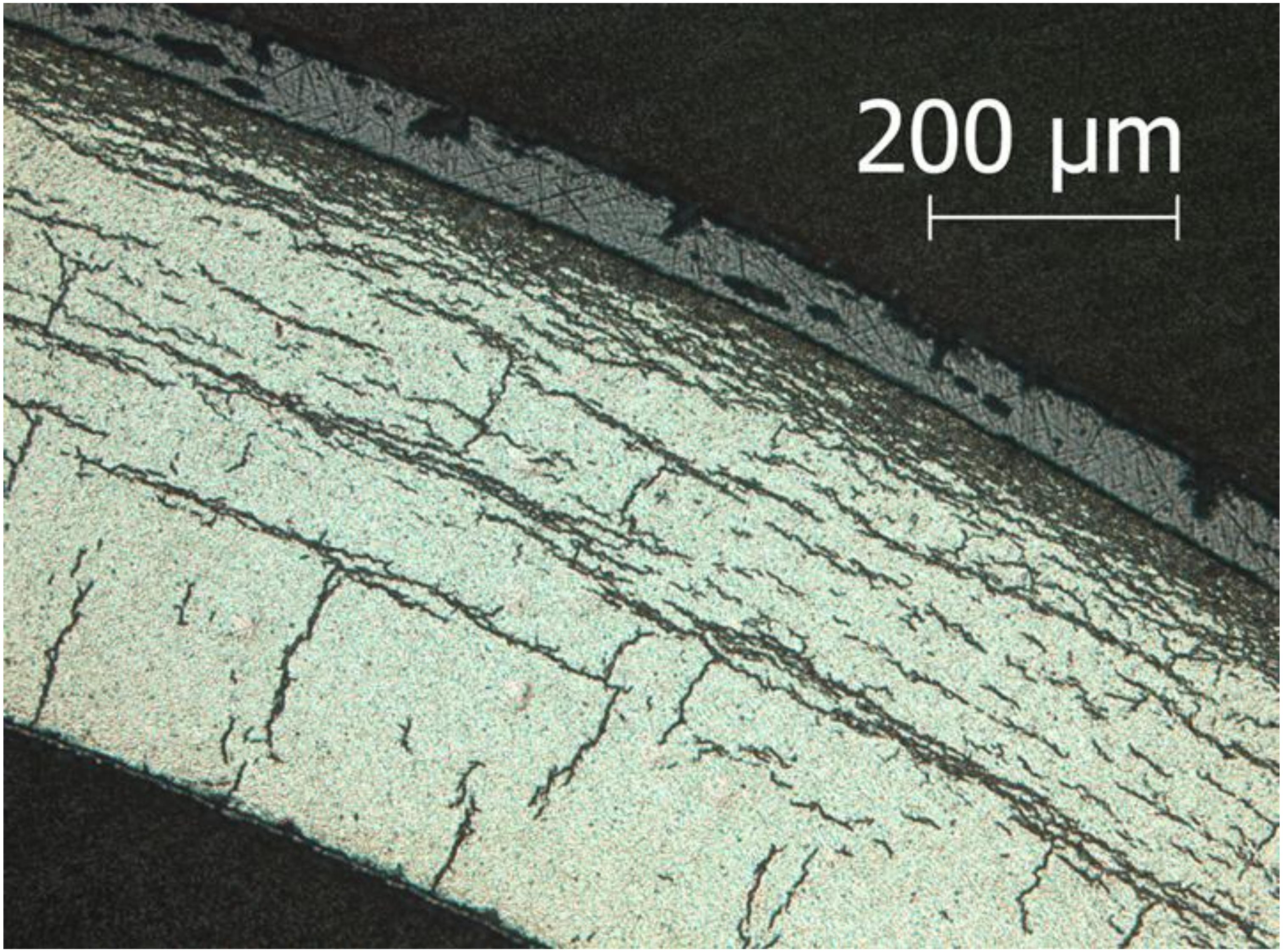

Figure A.4: Image (100X) of ZIRLO™ sample 105F6 in Area 4 from 1-cycle 350°C rodlet.

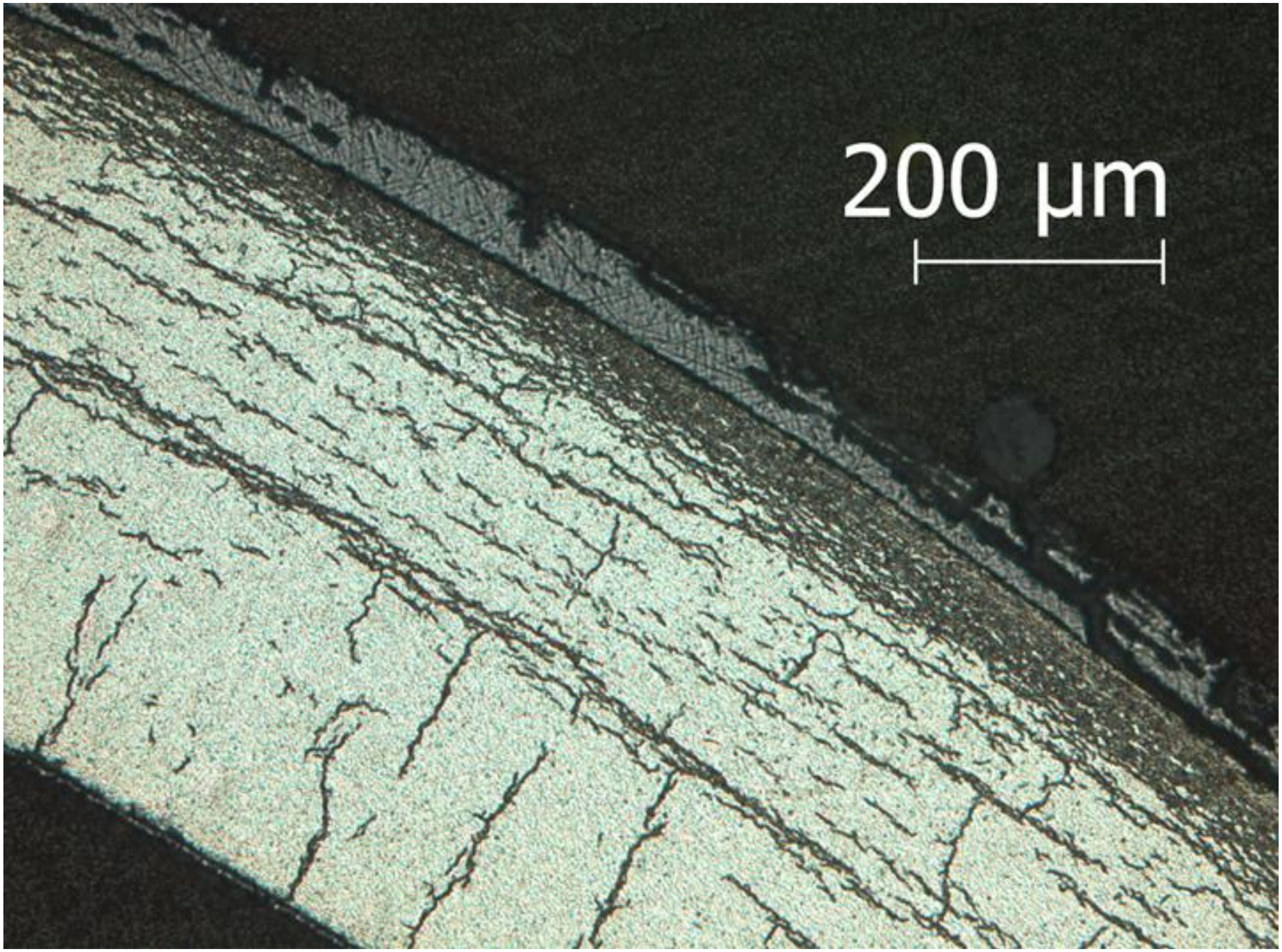

Figure A.5: Image (100X) of ZIRLO™ sample 105F6 in Area 5 from 1-cycle 350°C rodlet.

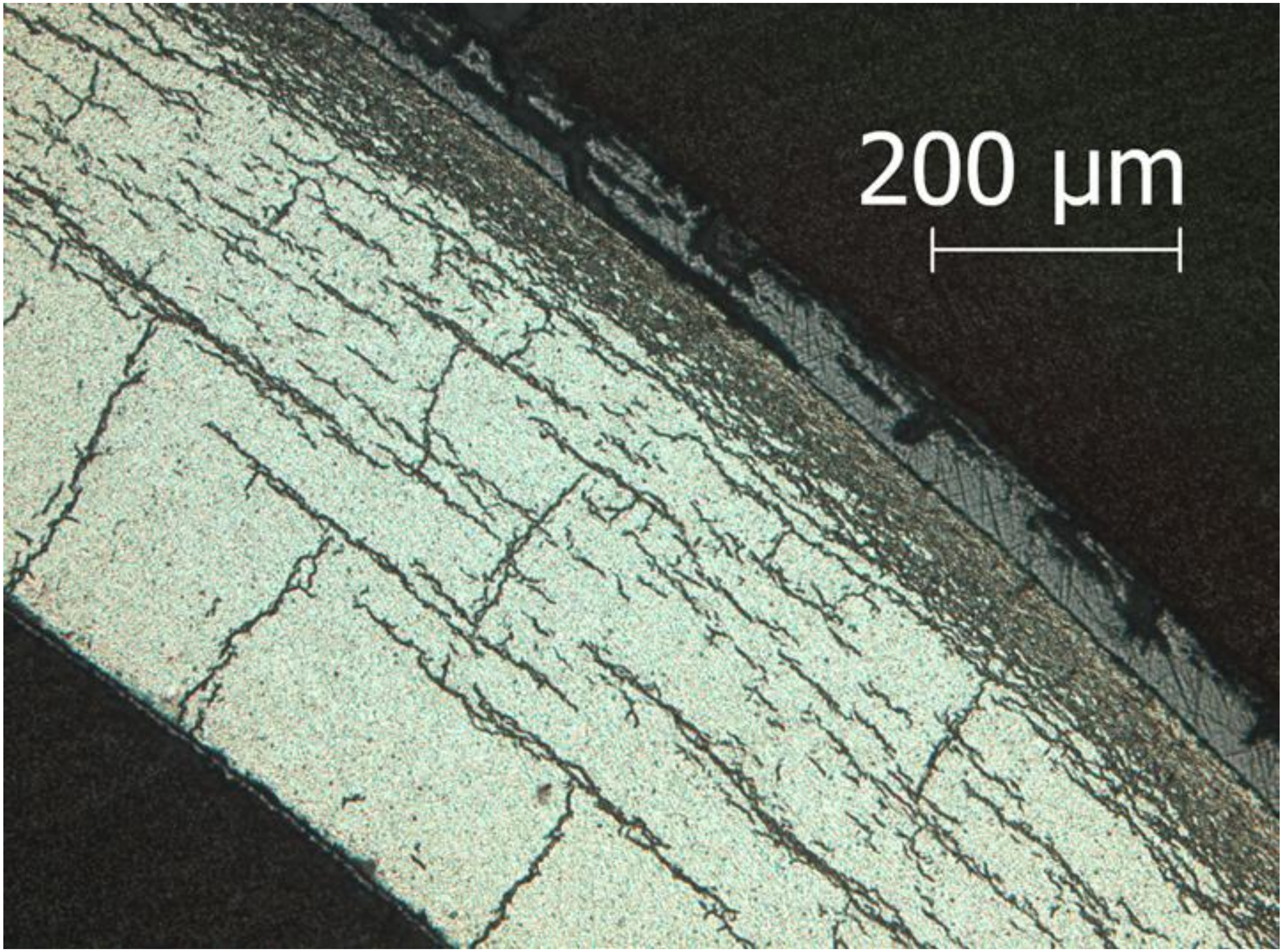

Figure A.6: Image (100X) of ZIRLO™ sample 105F6 in Area 6 from 1-cycle 350°C rodlet.

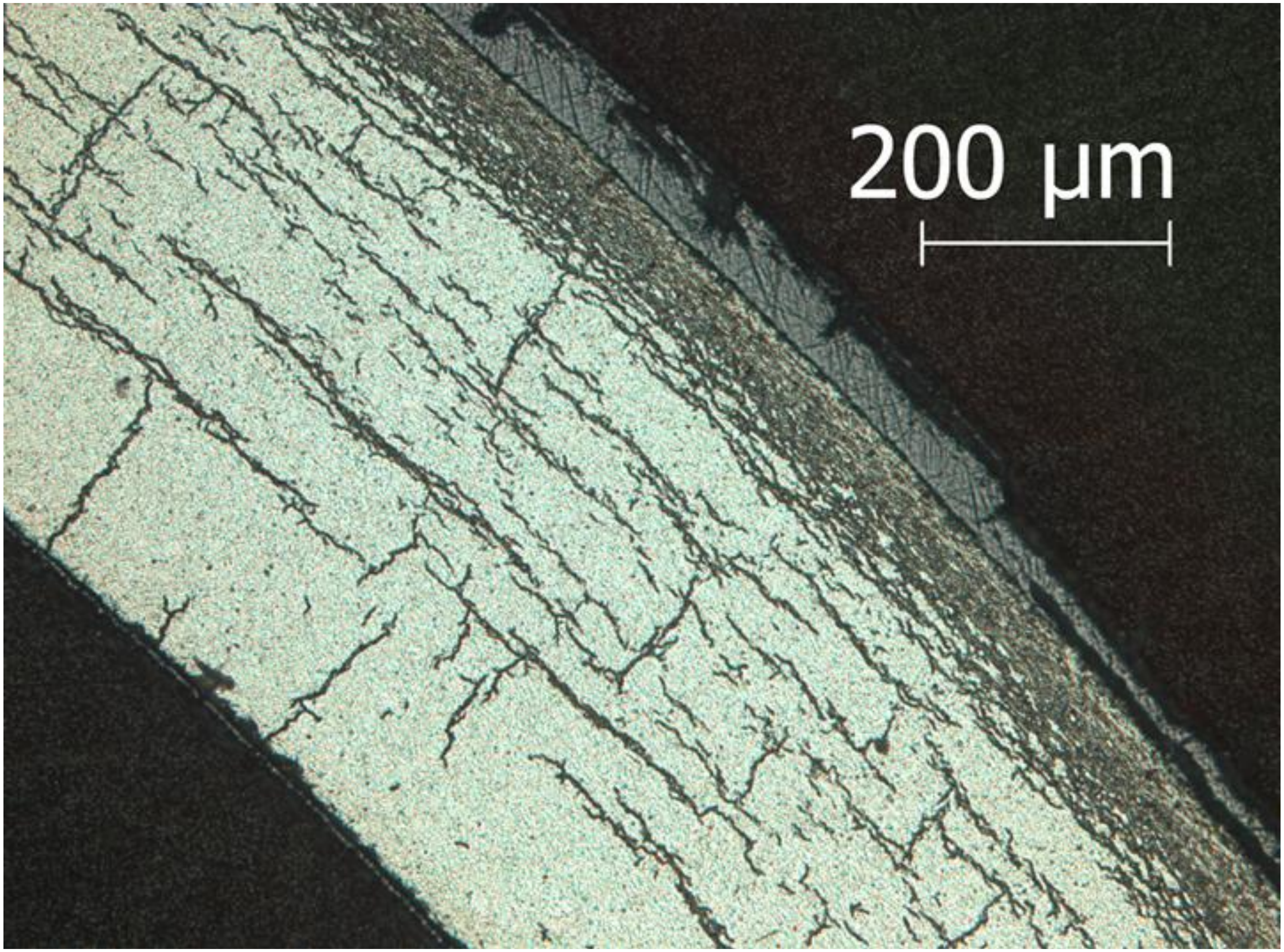

Figure A.7: Image (100X) of ZIRLO™ sample 105F6 in Area 7 from 1-cycle 350°C rodlet.

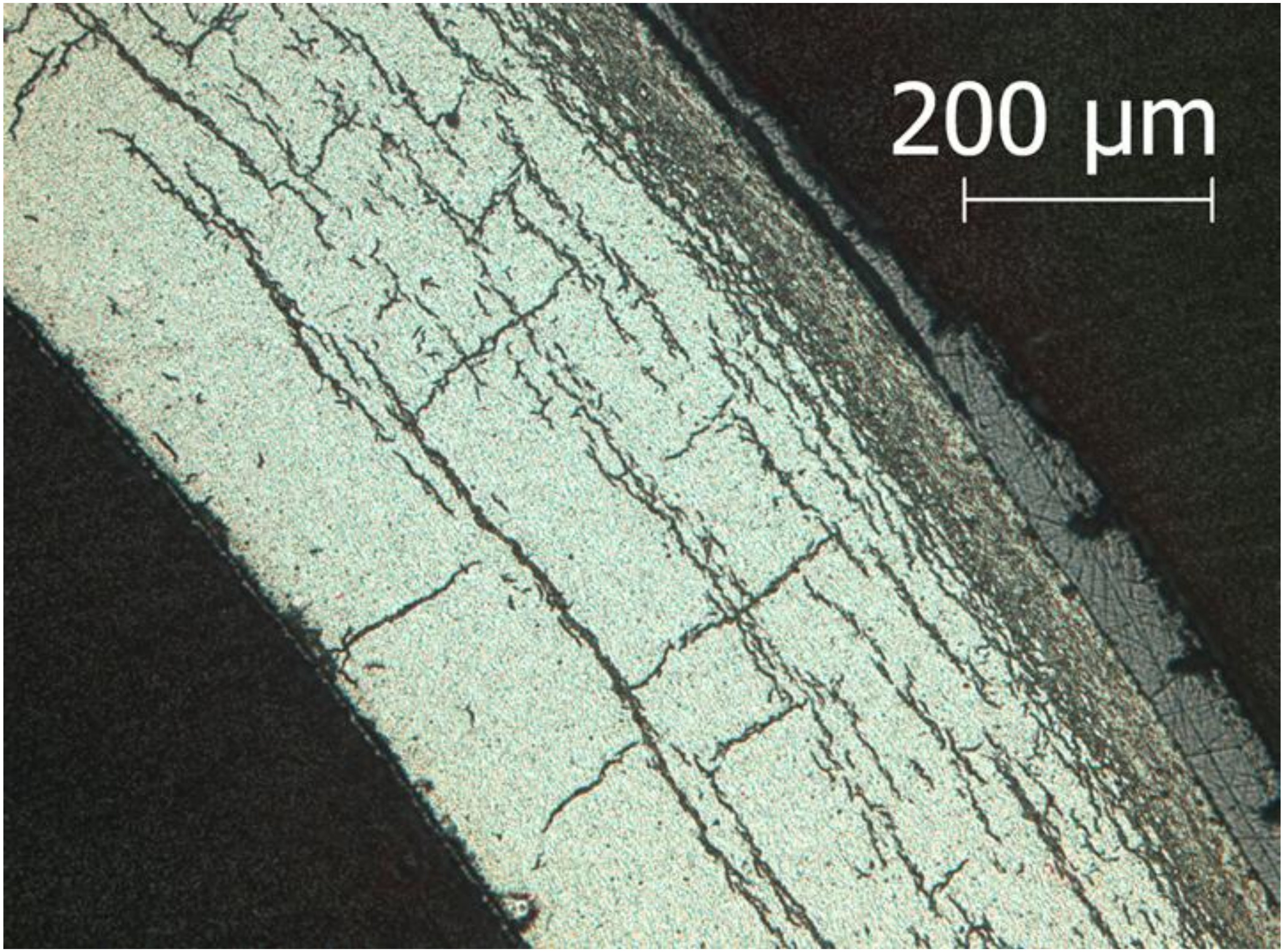

Figure A.8: Image (100X) of ZIRLO™ sample 105F6 in Area 8 from 1-cycle 350°C rodlet.

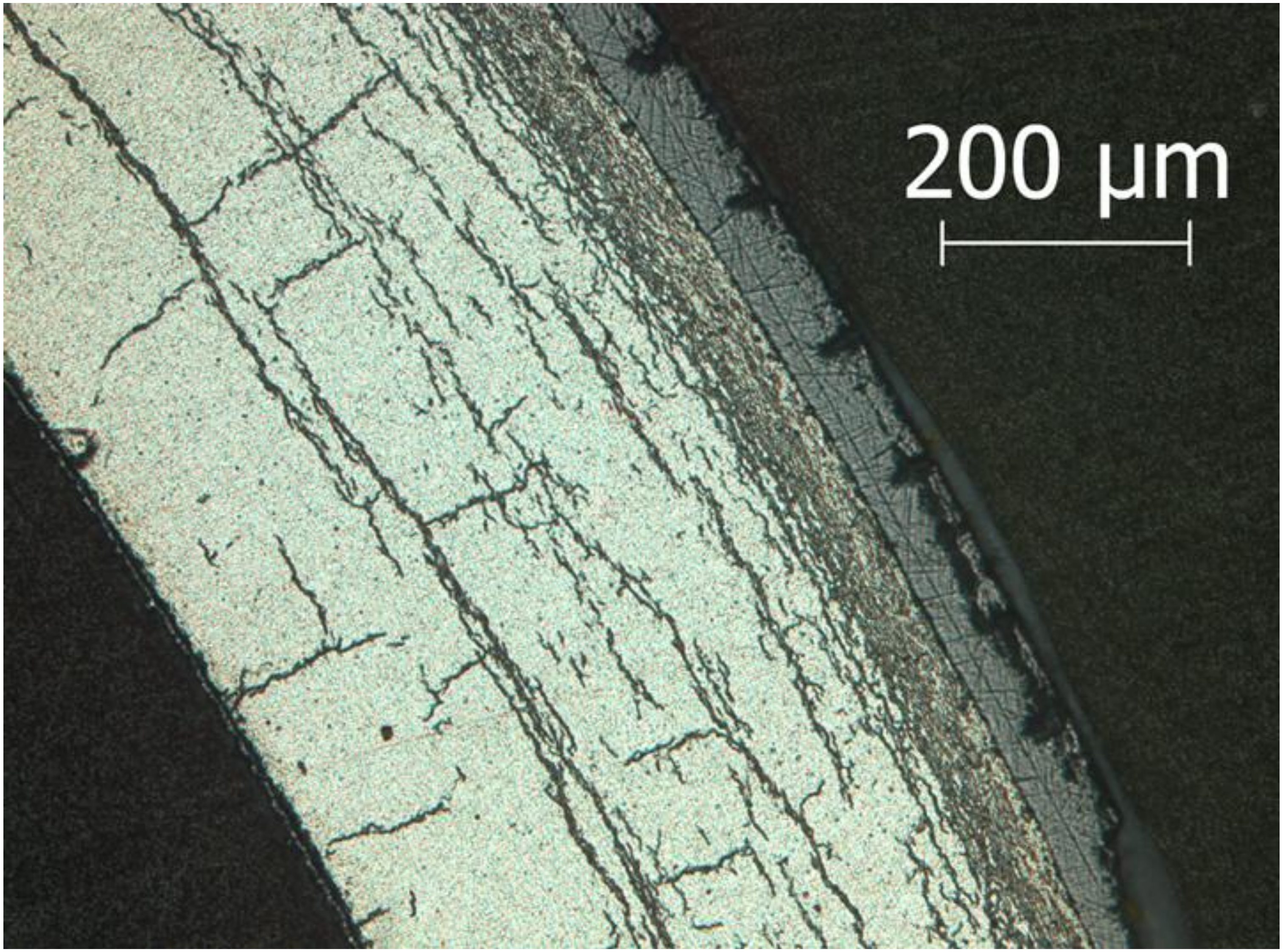

Figure A.9: Image (100X) of ZIRLO™ sample 105F6 in Area 9 from 1-cycle 350°C rodlet.

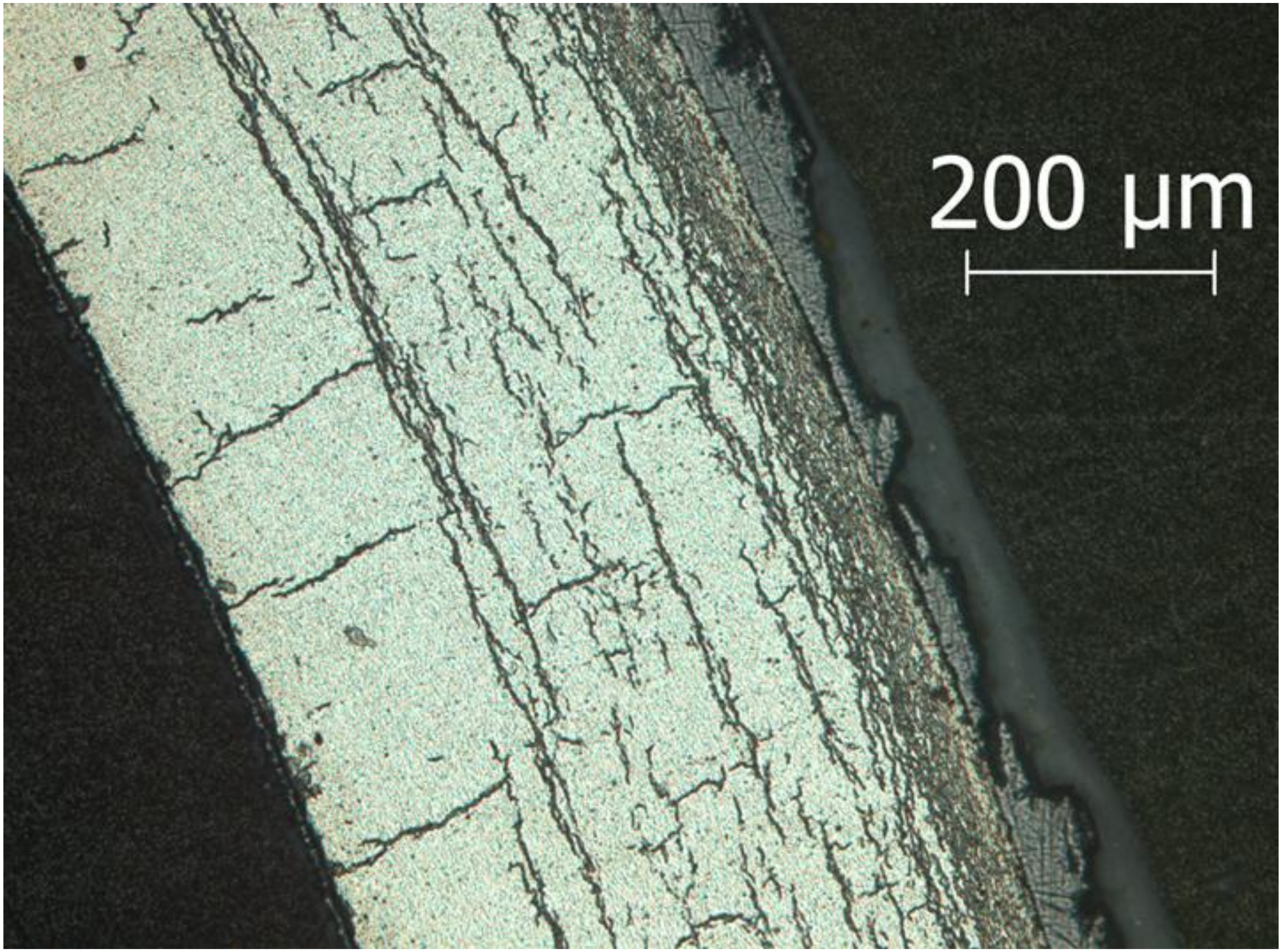

Figure A.10: Image (100X) of ZIRLO™ sample 105F6 in Area 10 from 1-cycle 350°C rodlet.

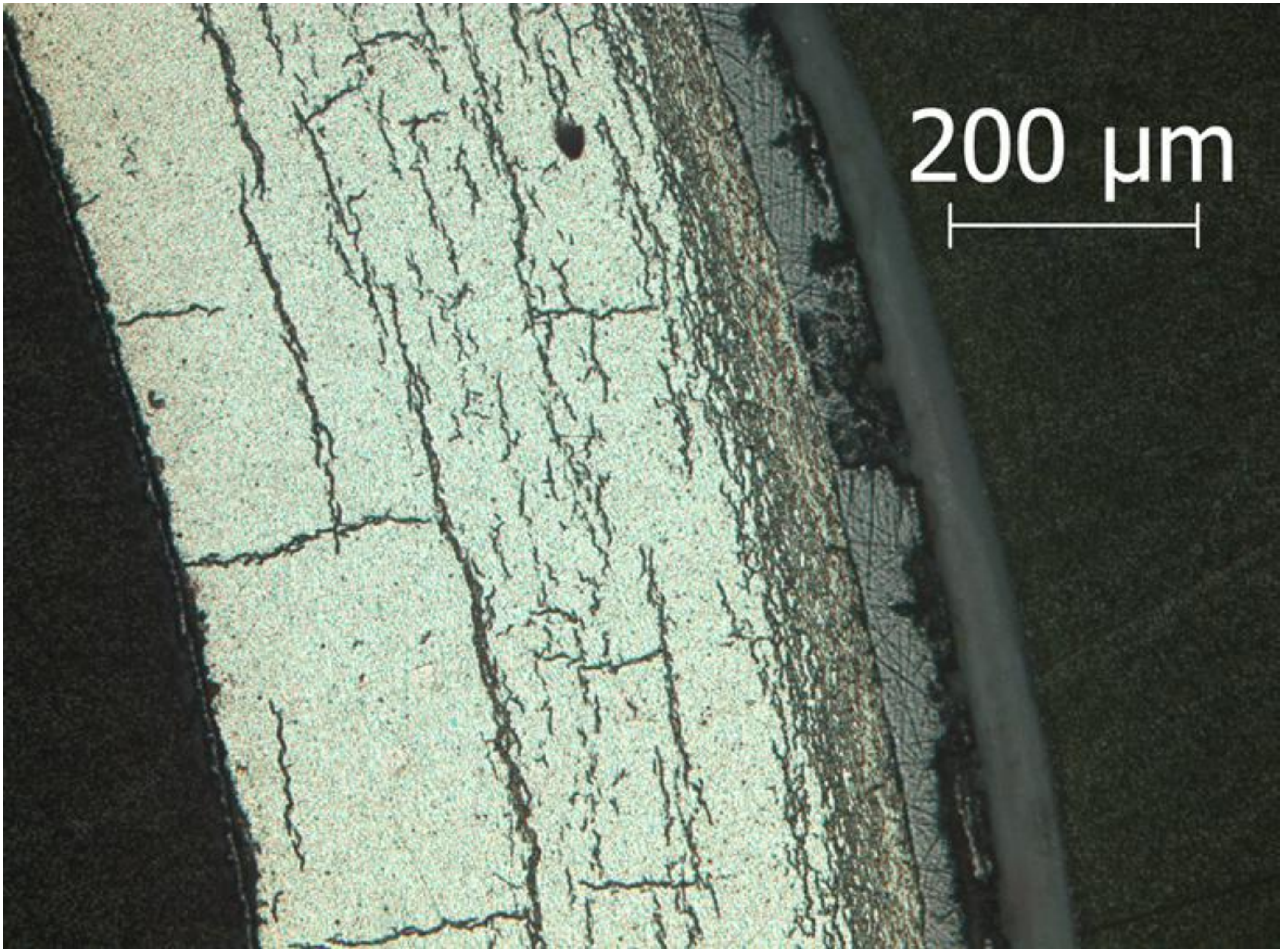

Figure A.11: Image (100X) of ZIRLO™ sample 105F6 in Area 11 from 1-cycle 350°C rodlet.

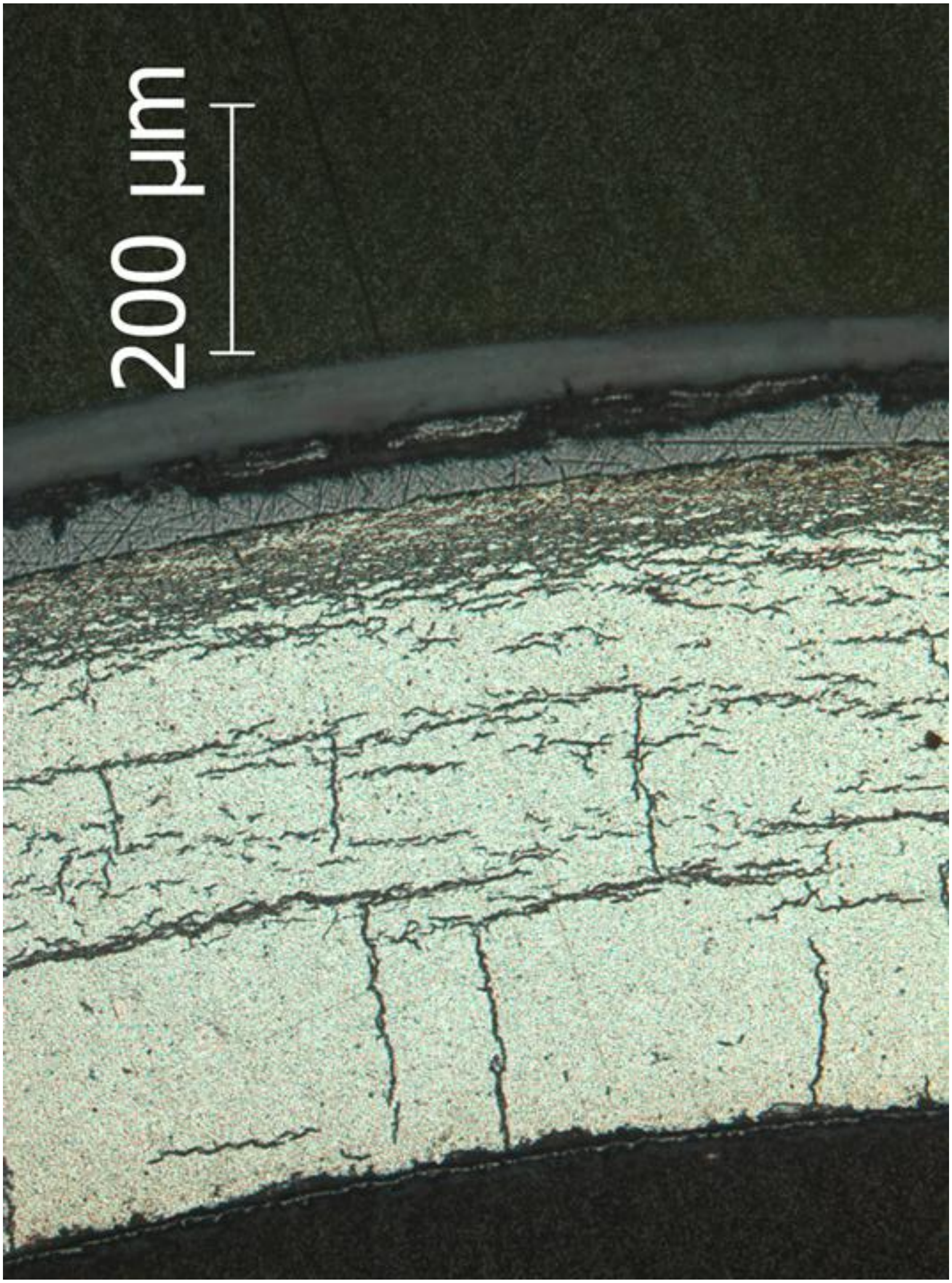

Figure A.12: Image (100X) of ZIRLO™ sample 105F6 in Area 12 from 1-cycle 350°C rodlet.

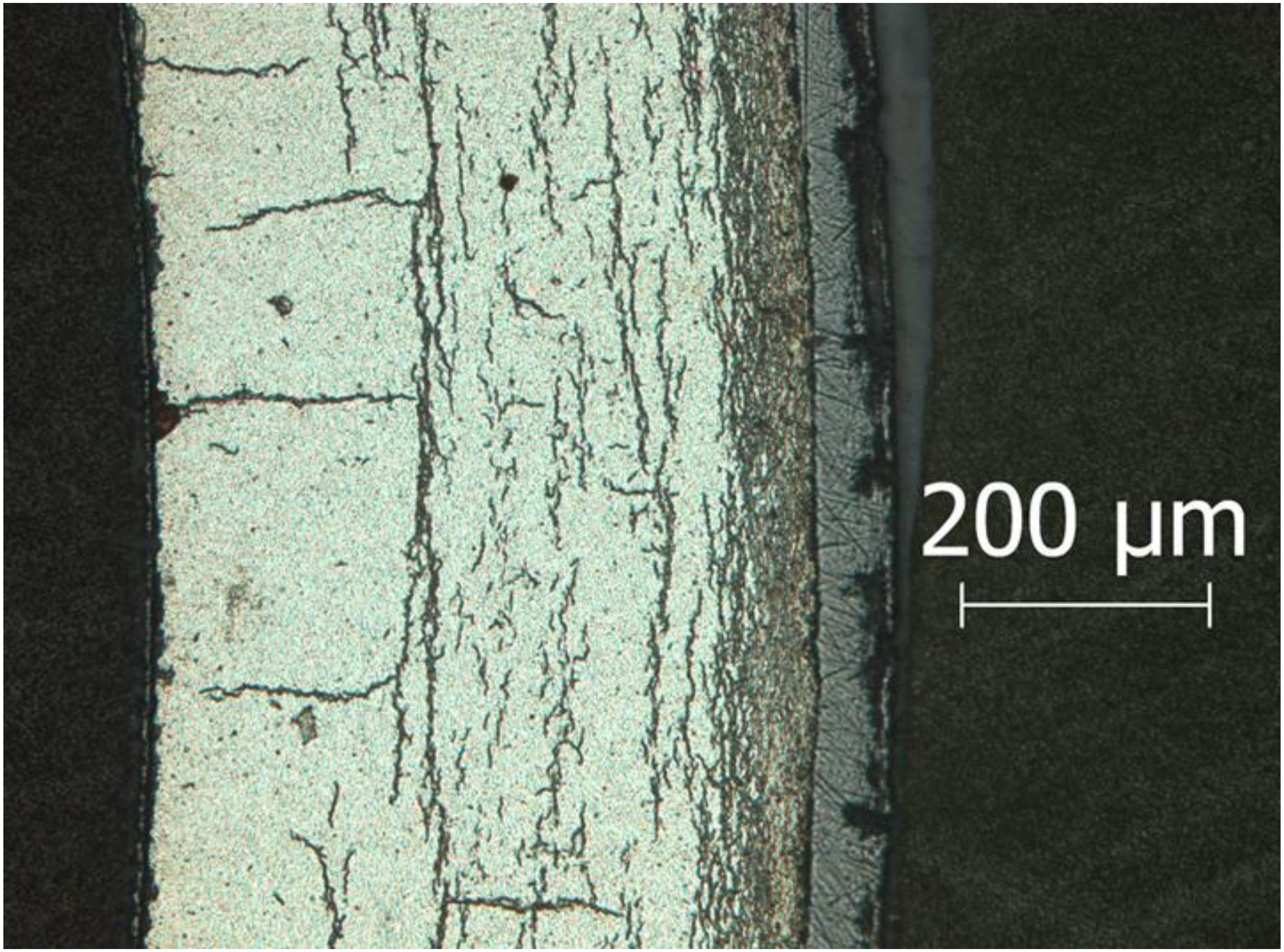

Figure A.13: Image (100X) of ZIRLO™ sample 105F6 in Area 13 from 1-cycle 350°C rodlet.

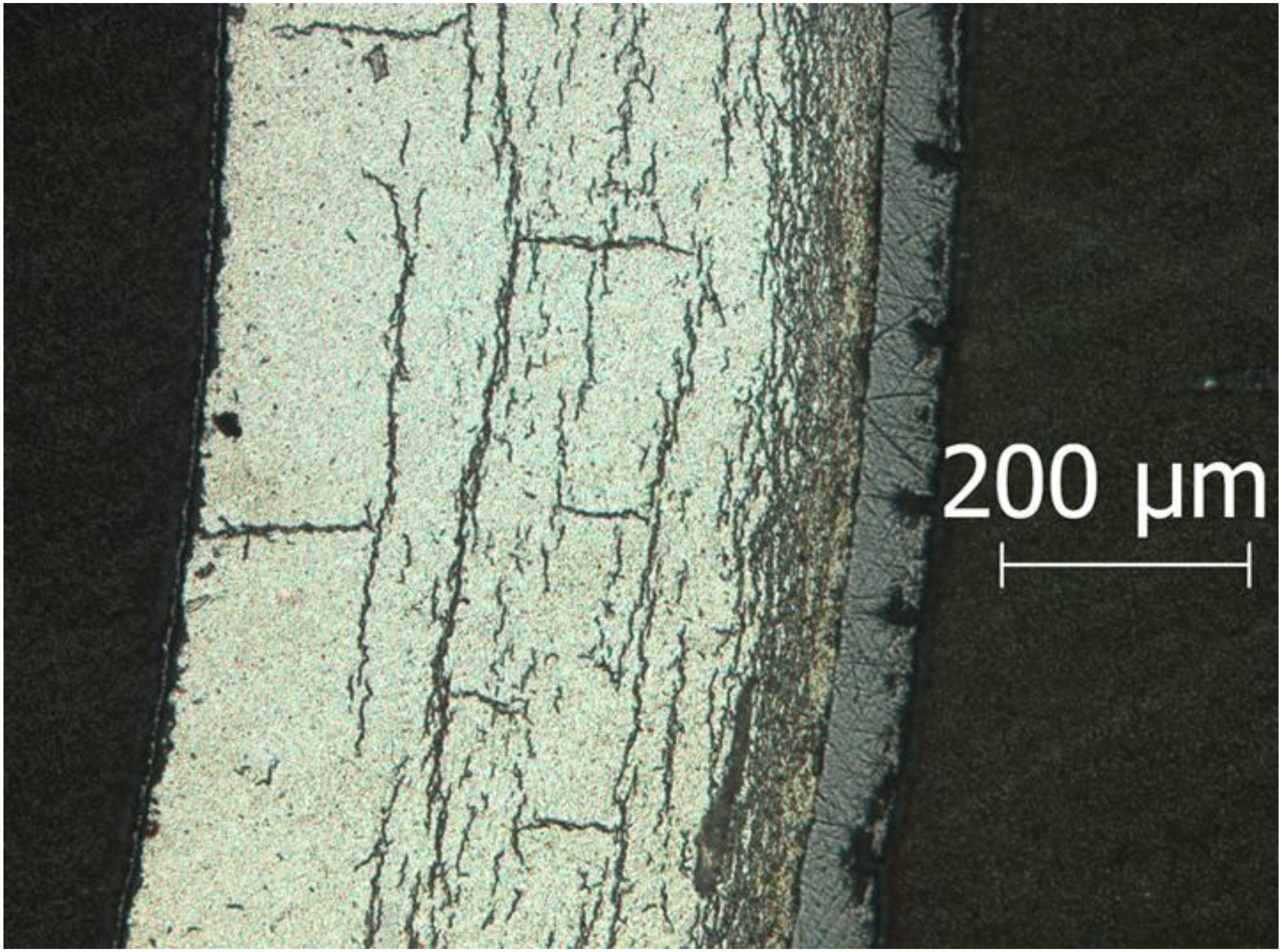

Figure A.14: Image (100X) of ZIRLO™ sample 105F6 in Area 14 from 1-cycle 350°C rodlet.

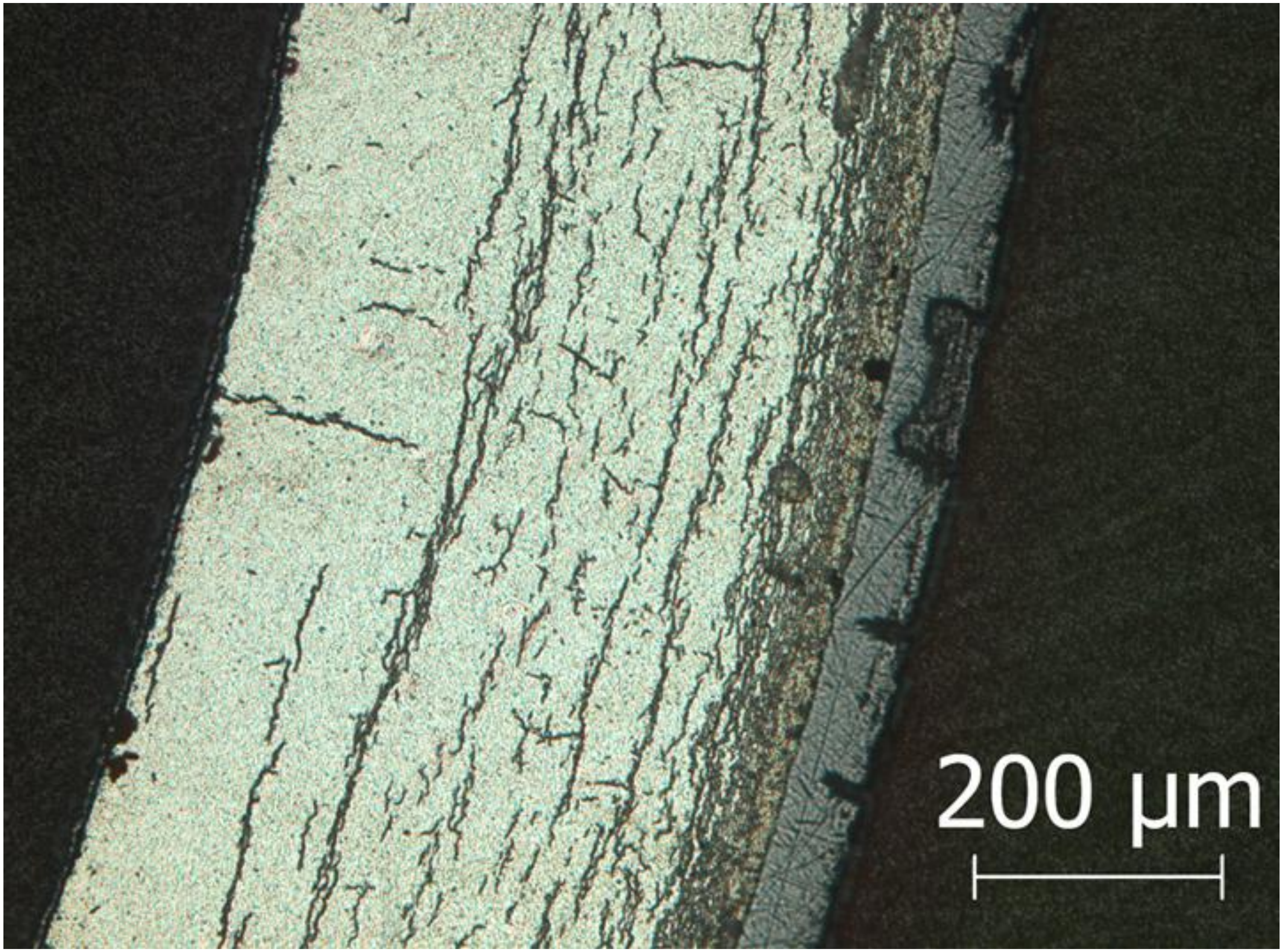

Figure A.15: Image (100X) of ZIRLO™ sample 105F6 in Area 15 from 1-cycle 350°C rodlet.

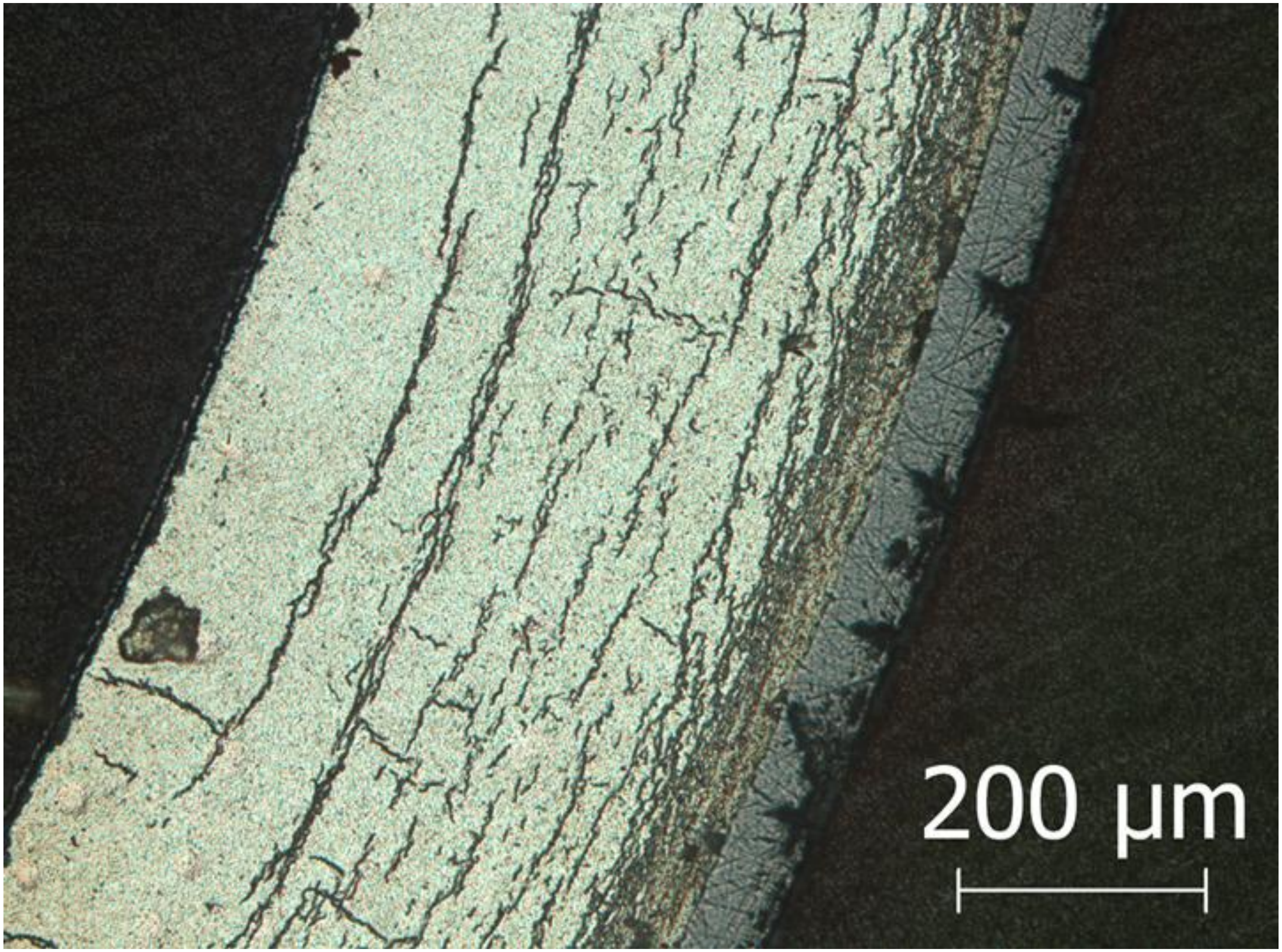

Figure A.16: Image (100X) of ZIRLO™ sample 105F6 in Area 16 from 1-cycle 350°C rodlet.

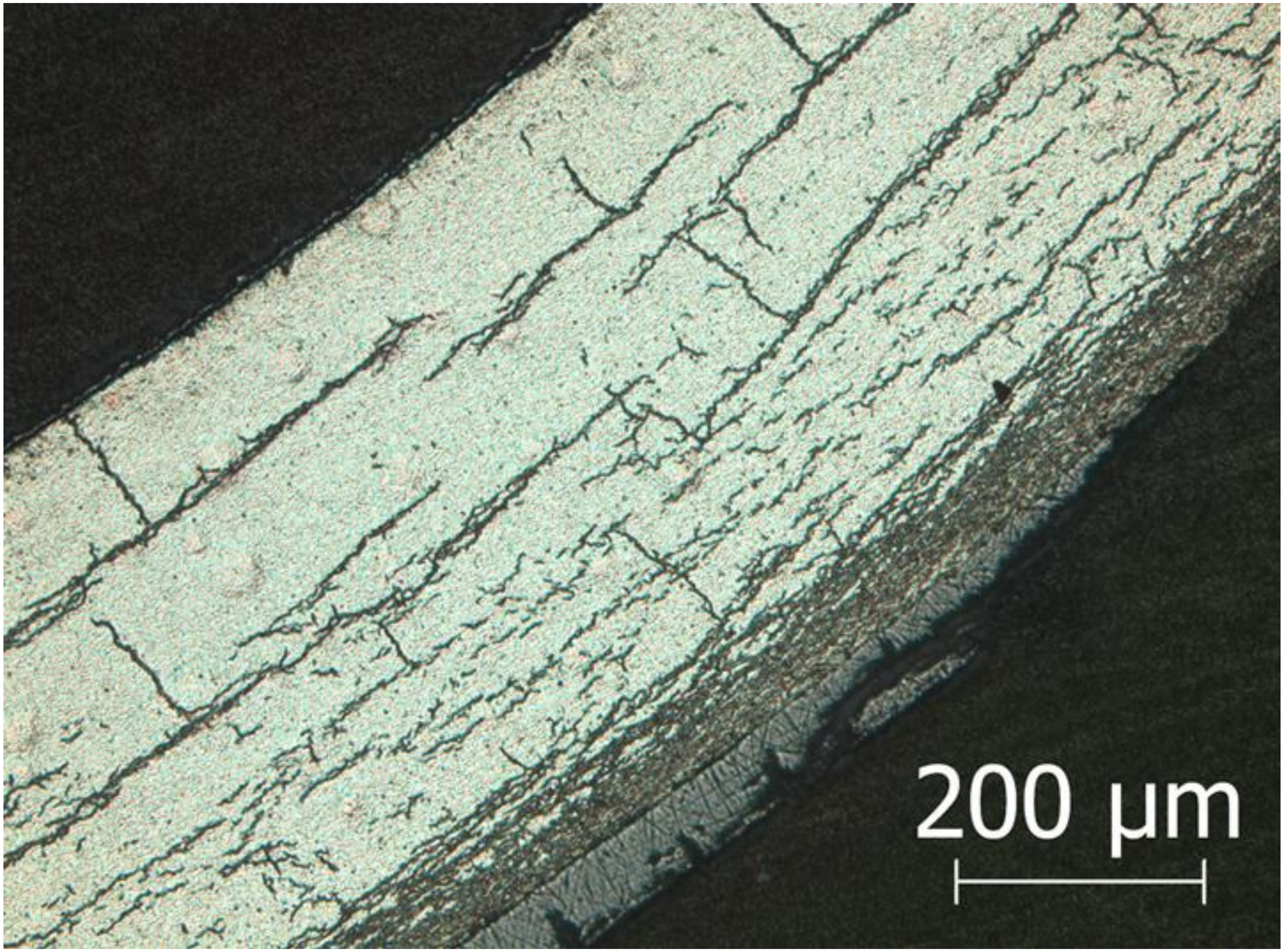

Figure A.17: Image (100X) of ZIRLO™ sample 105F6 in Area 17 from 1-cycle 350°C rodlet.

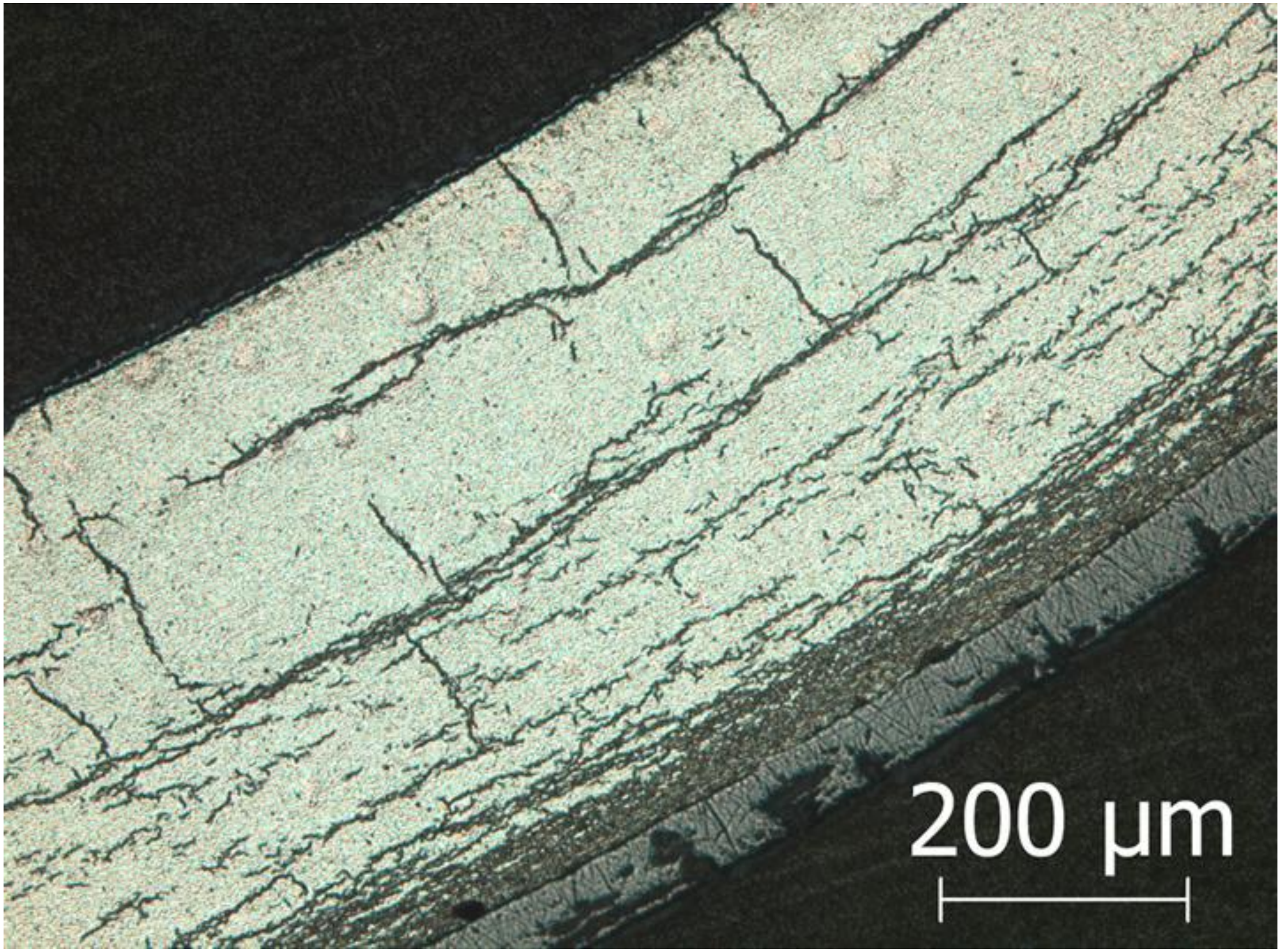

Figure A.18: Image (100X) of ZIRLO™ sample 105F6 in Area 18 from 1-cycle 350°C rodlet.

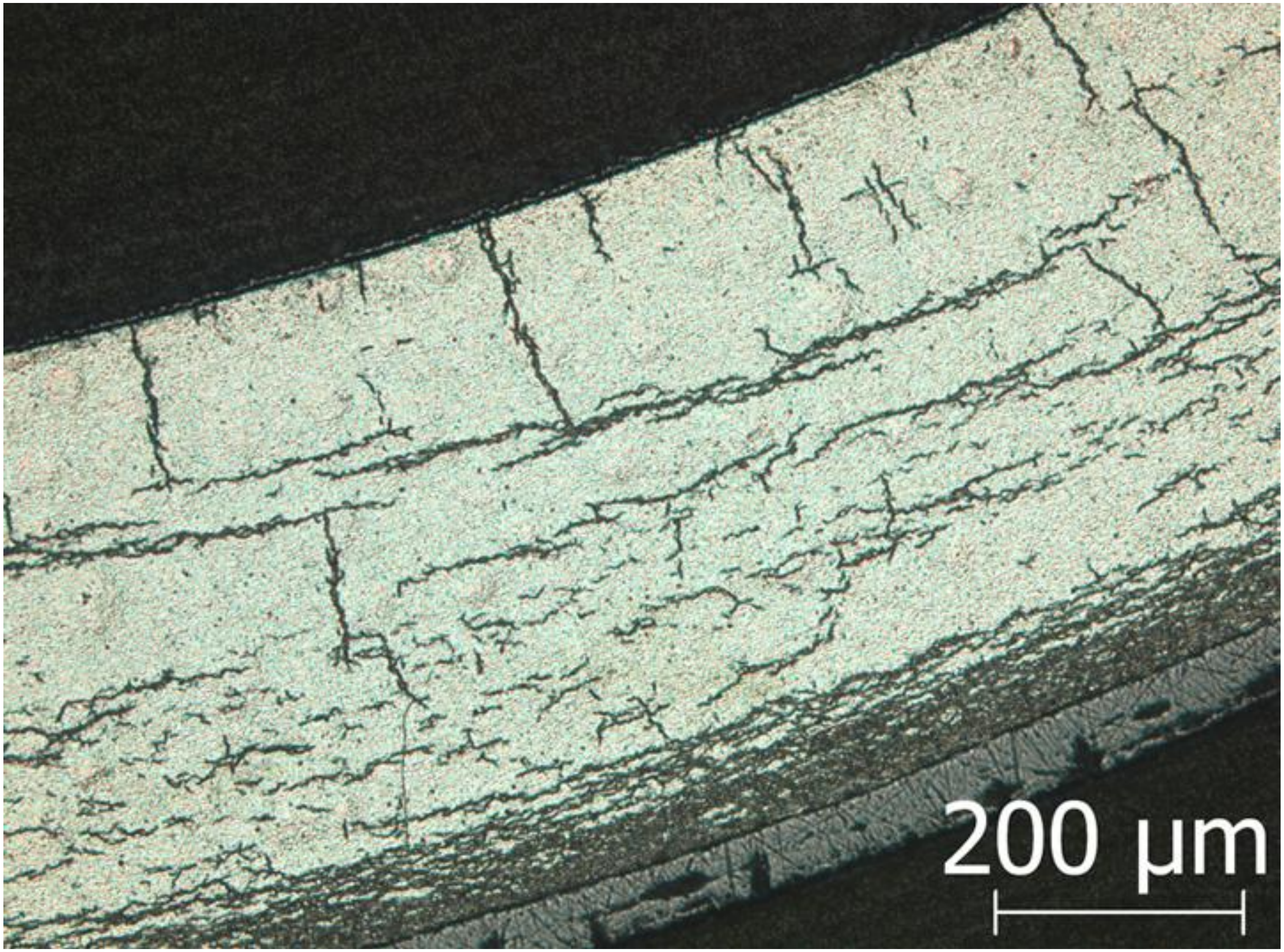

Figure A.19: Image (100X) of ZIRLO™ sample 105F6 in Area 19 from 1-cycle 350°C rodlet.

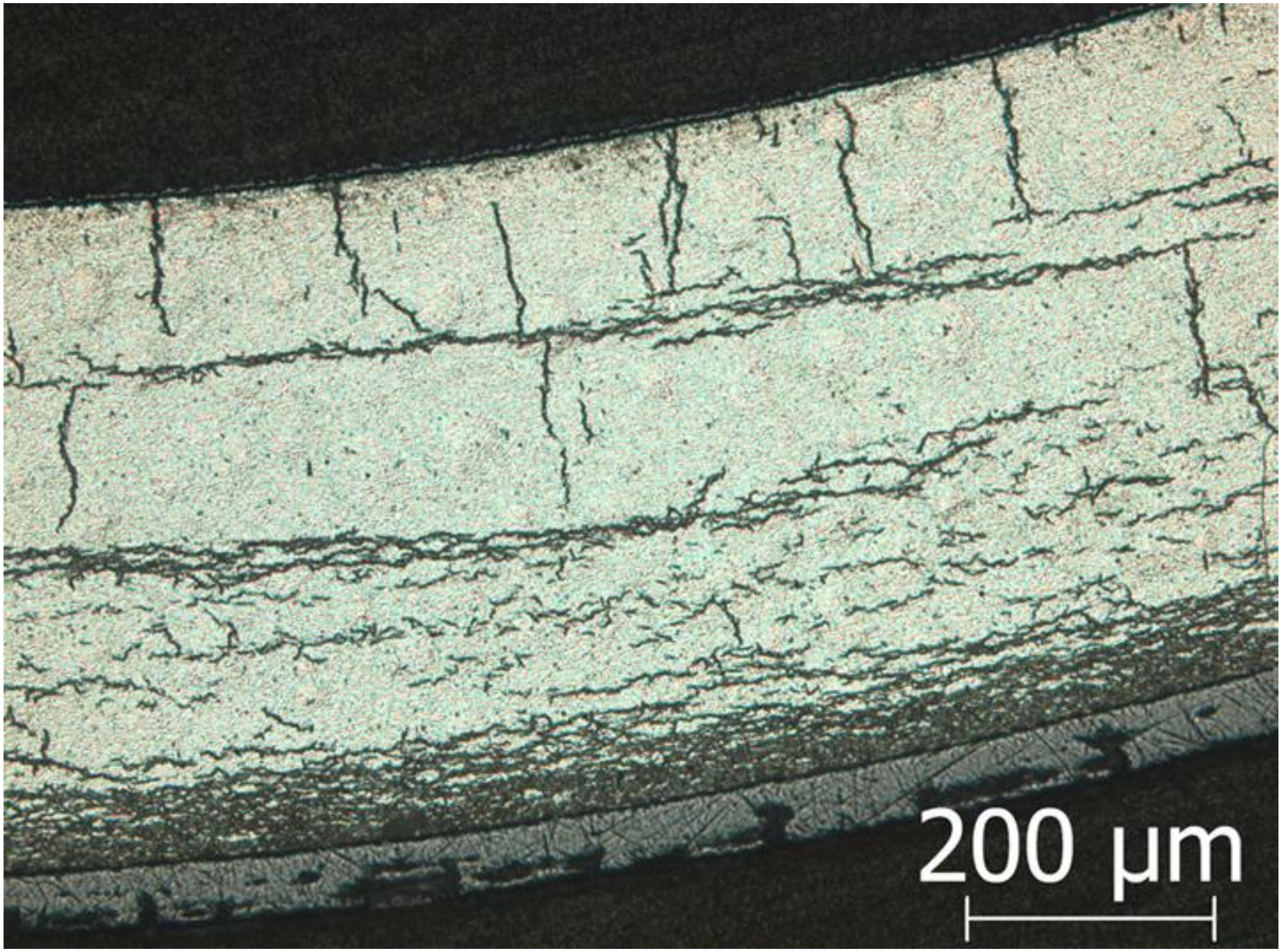

Figure A.20: Image (100X) of ZIRLO™ sample 105F6 in Area 20 from 1-cycle 350°C rodlet.

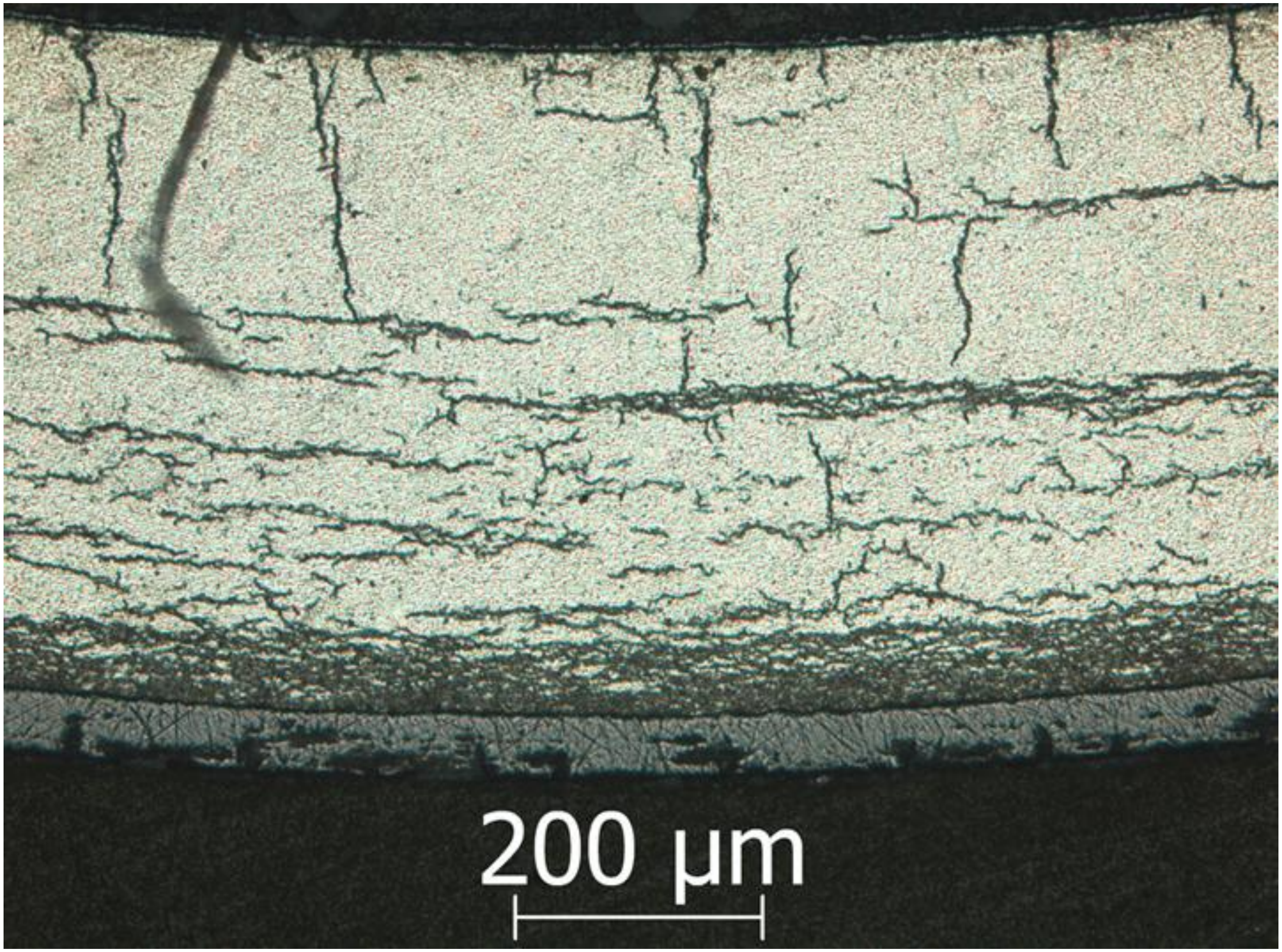

Figure A.21: Image (100X) of ZIRLO™ sample 105F6 in Area 21 from 1-cycle 350°C rodlet.

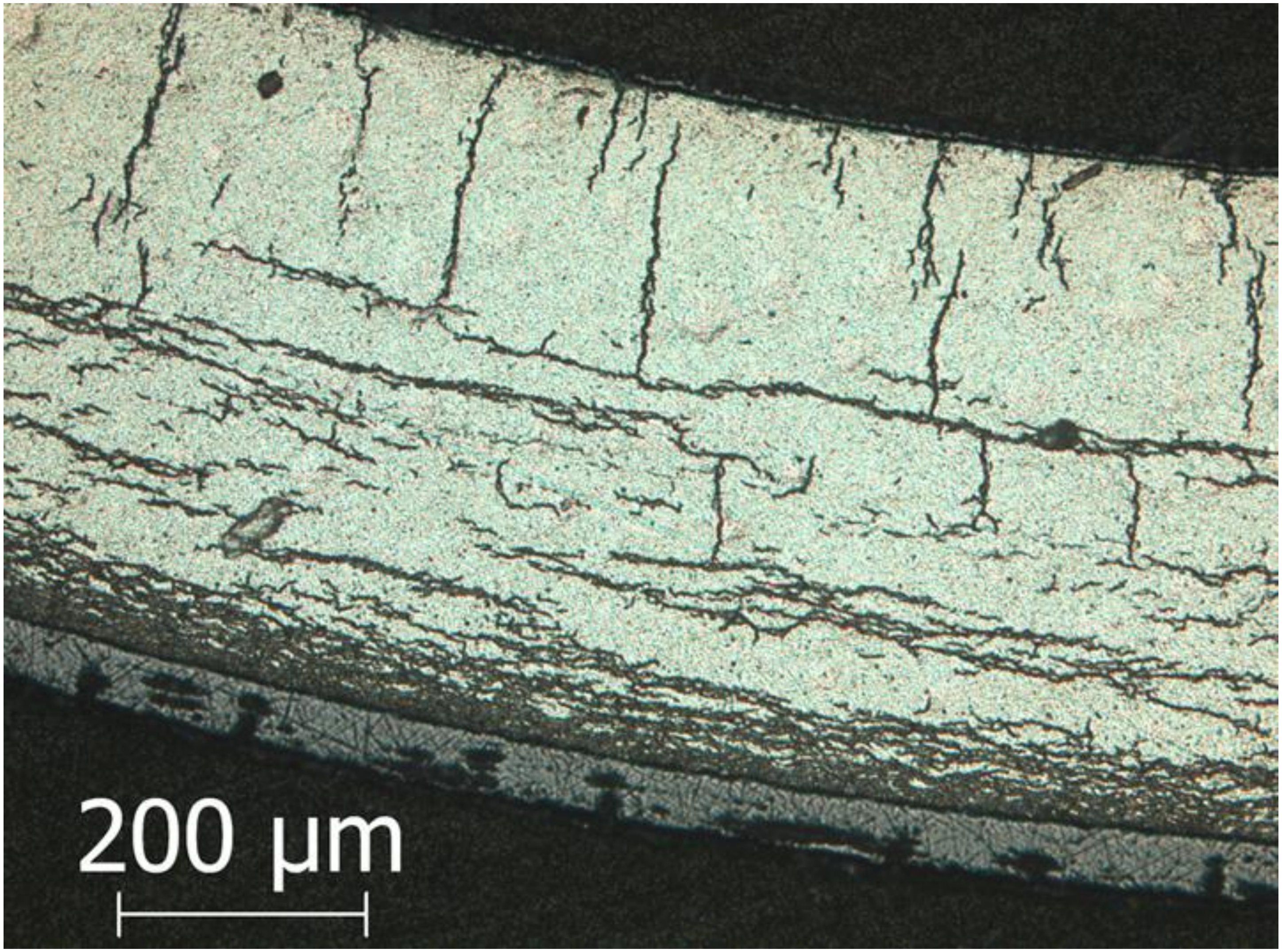

Figure A.22: Image (100X) of ZIRLO™ sample 105F6 in Area 22 from 1-cycle 350°C rodlet.

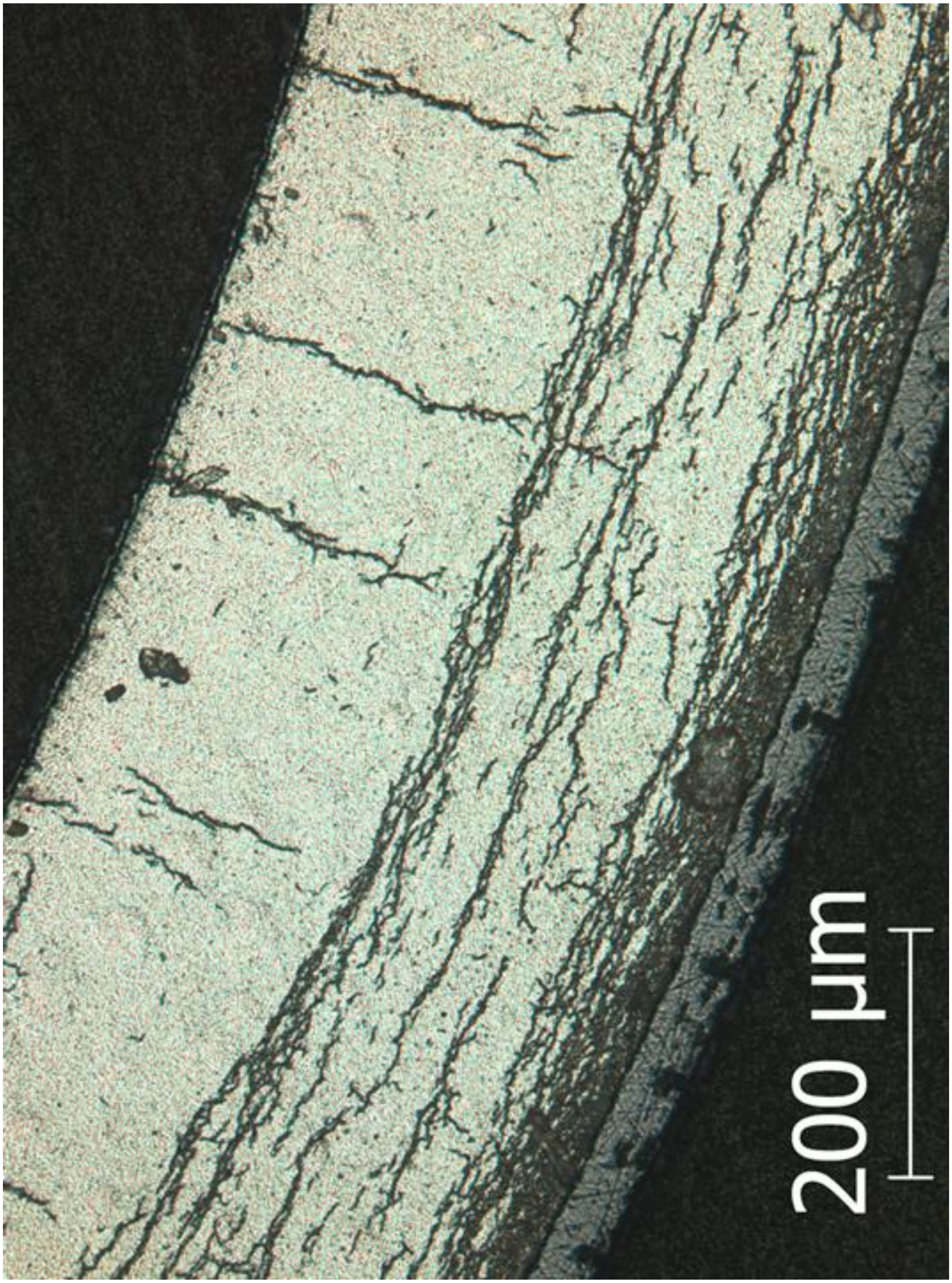

Figure A.23: Image (100X) of ZIRLO™ sample 105F6 in Area 23 from 1-cycle 350°C rodlet.

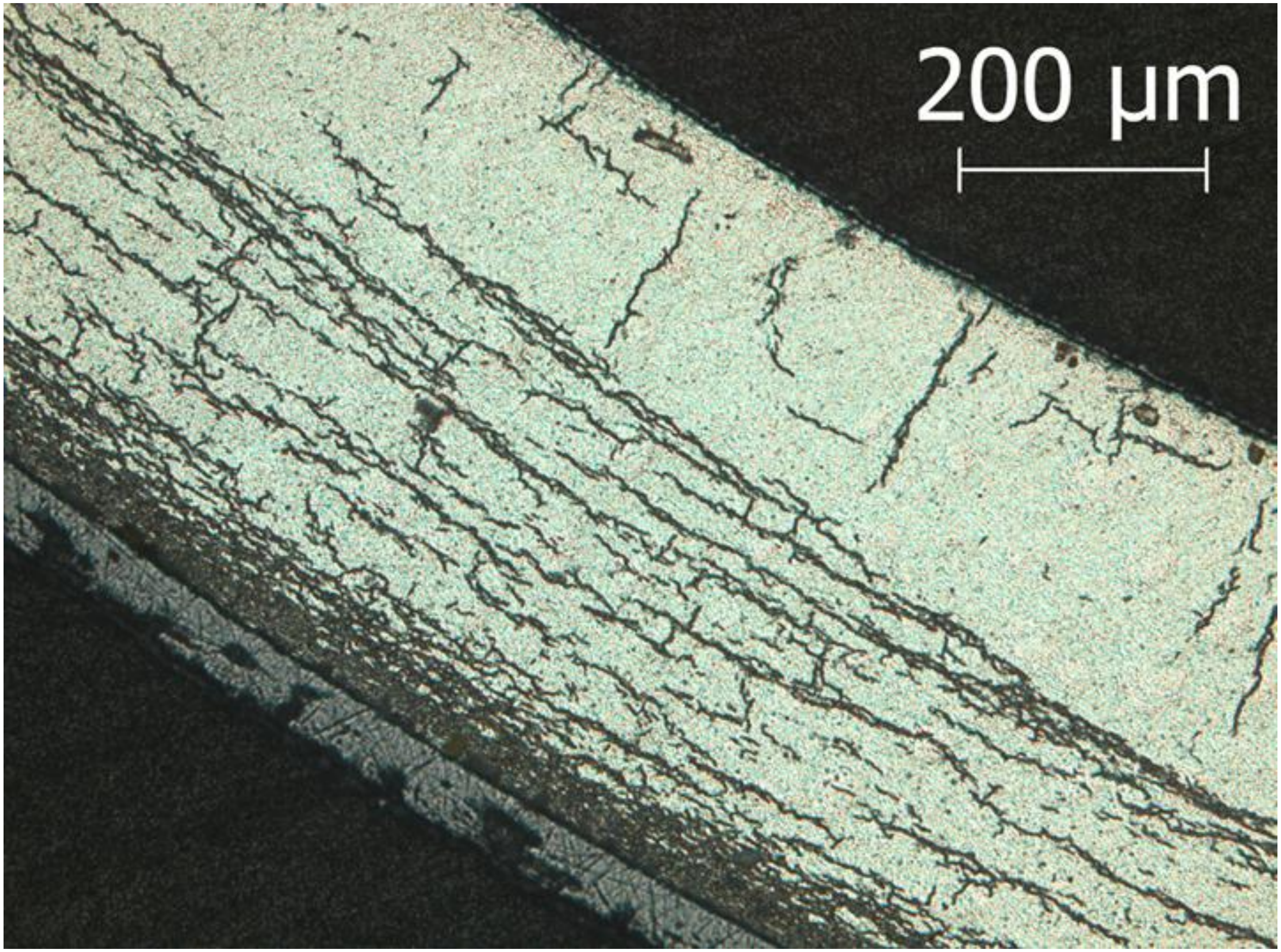

Figure A.24: Image (100X) of ZIRLO™ sample 105F6 in Area 24 from 1-cycle 350°C rodlet.

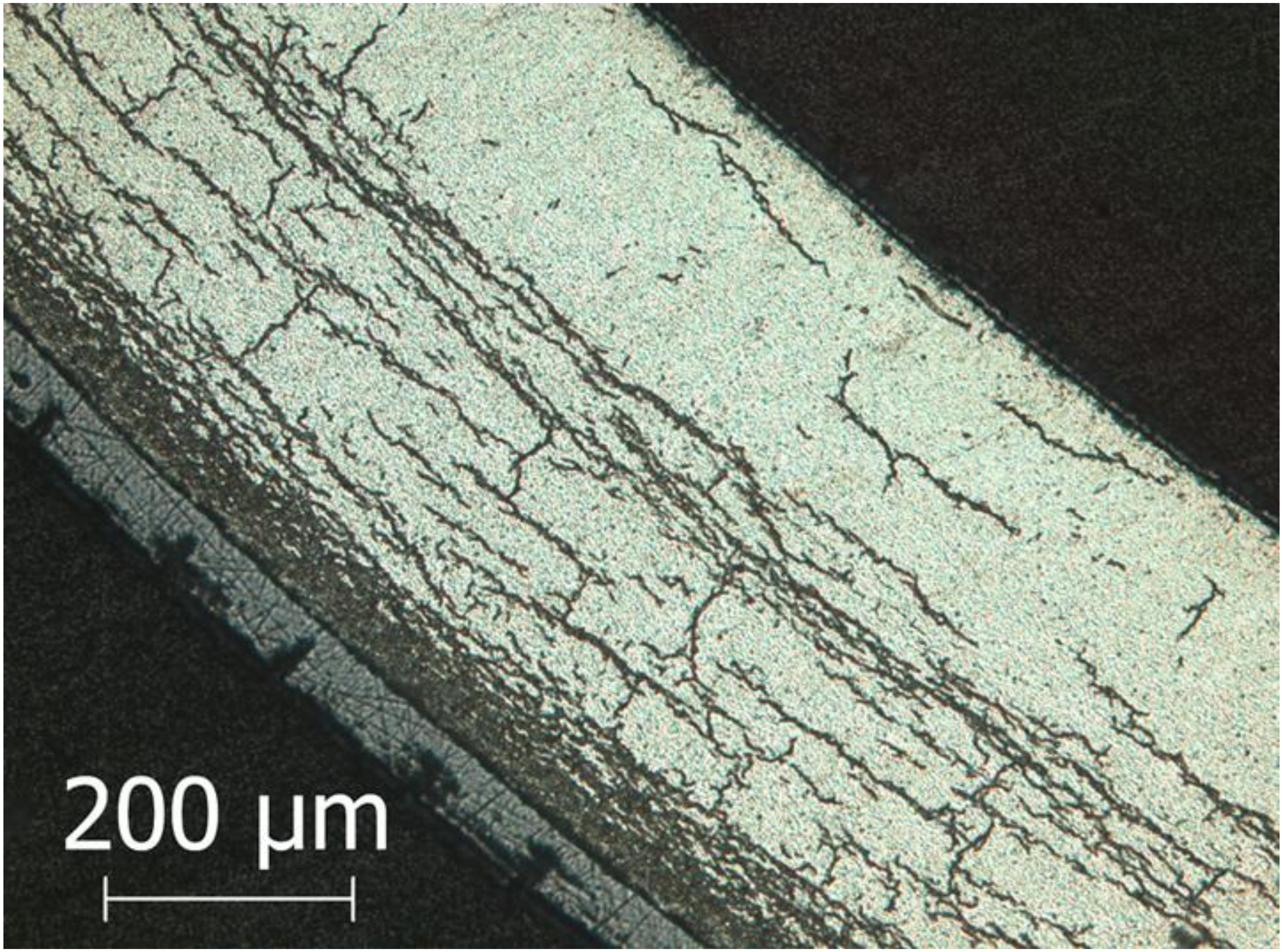

Figure A.25: Image (100X) of ZIRLO™ sample 105F6 in Area 25 from 1-cycle 350°C rodlet.

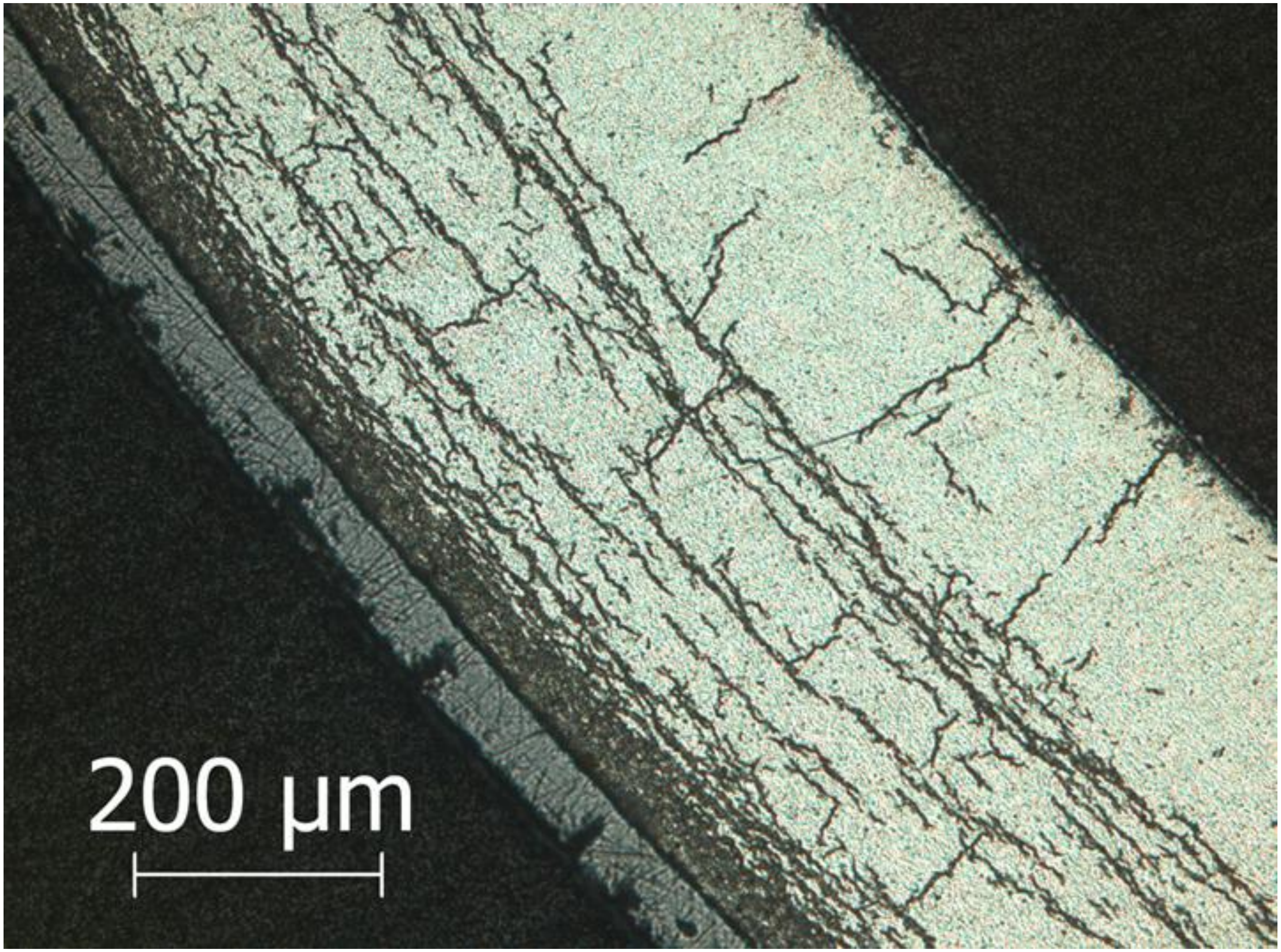

Figure A.26: Image (100X) of ZIRLO™ sample 105F6 in Area 26 from 1-cycle 350°C rodlet.

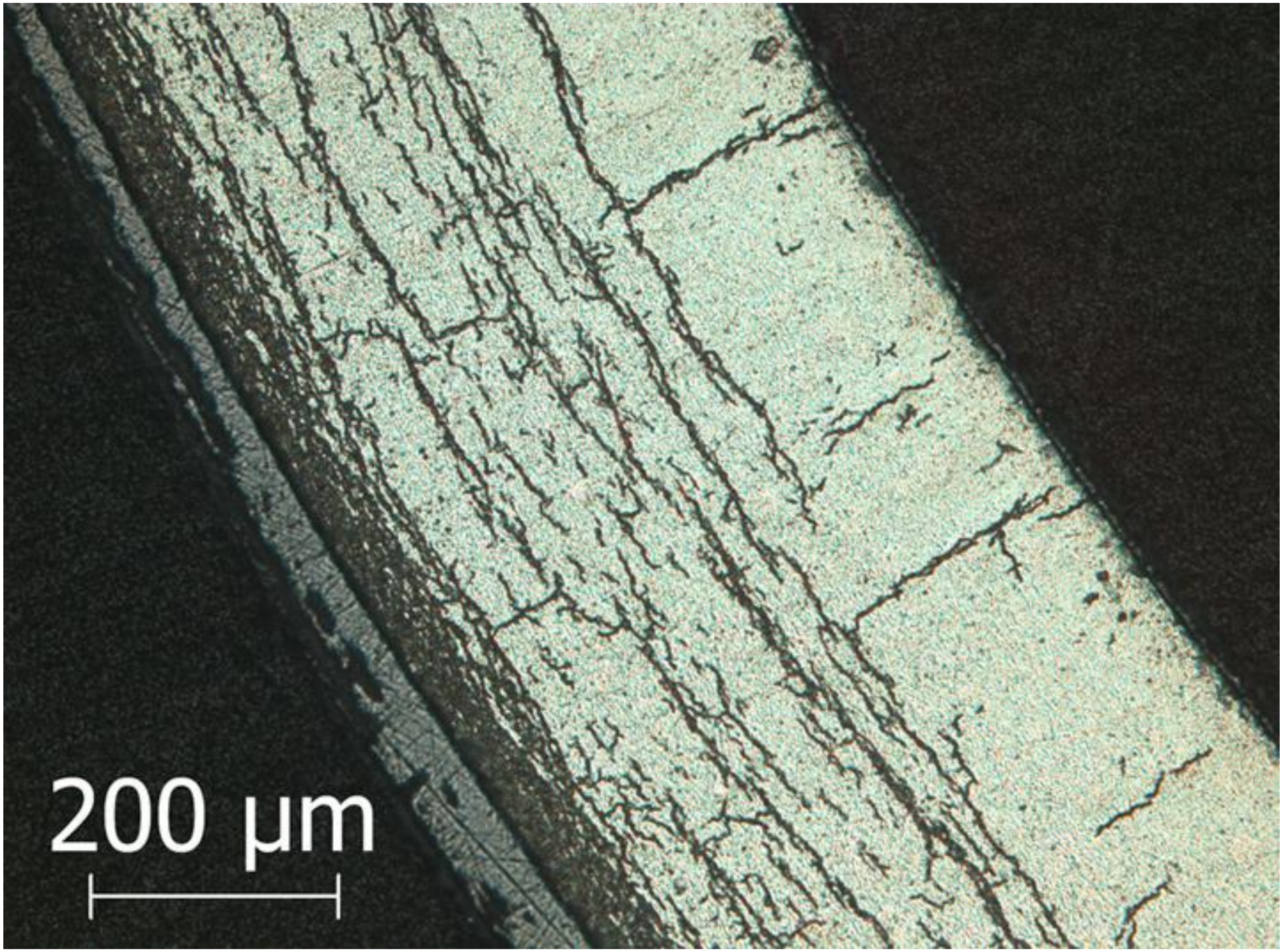

Figure A.27: Image (100X) of ZIRLO™ sample 105F6 in Area 27 from 1-cycle 350°C rodlet.

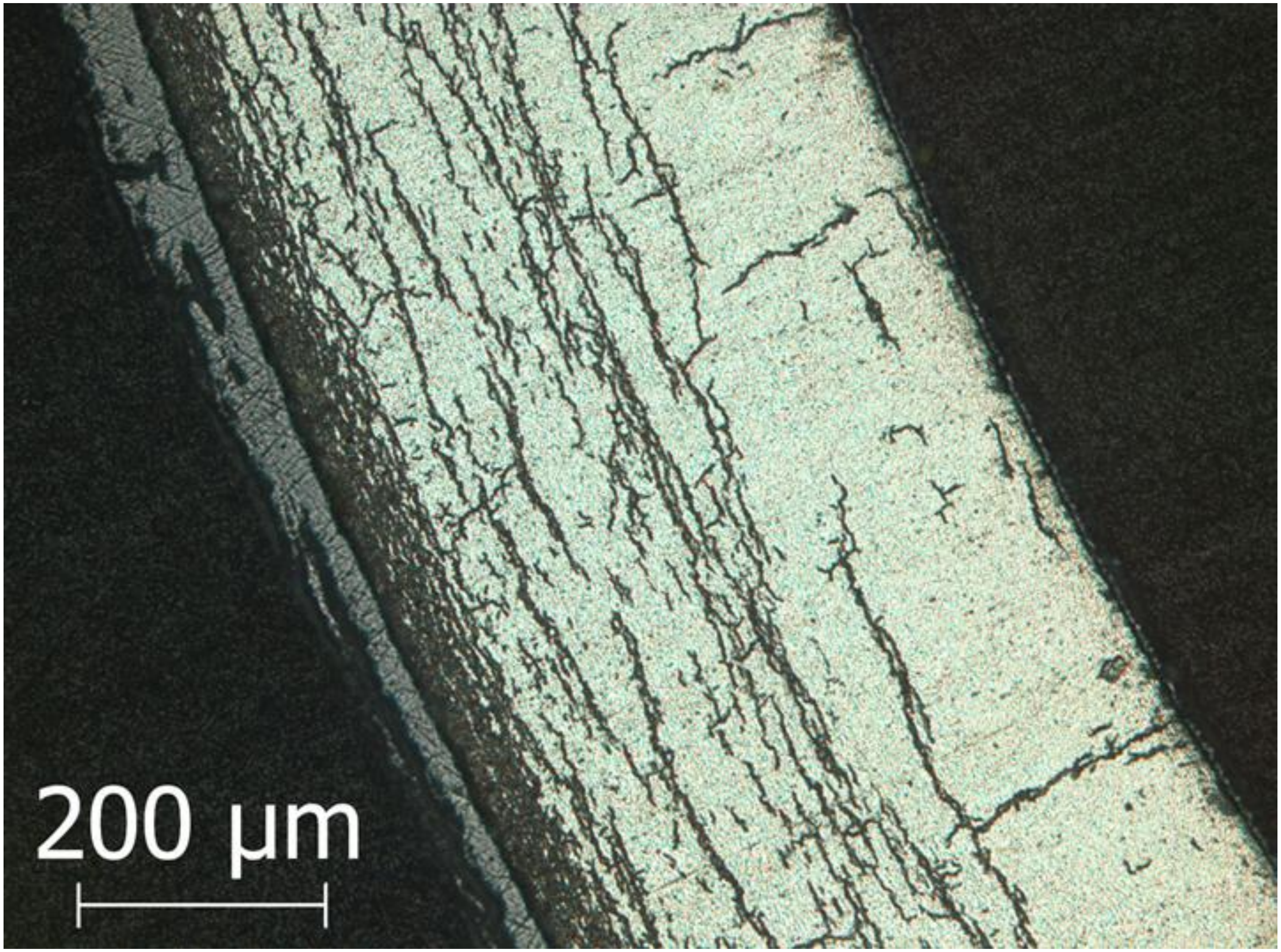

Figure A.28: Image (100X) of ZIRLO™ sample 105F6 in Area 28 from 1-cycle 350°C rodlet.

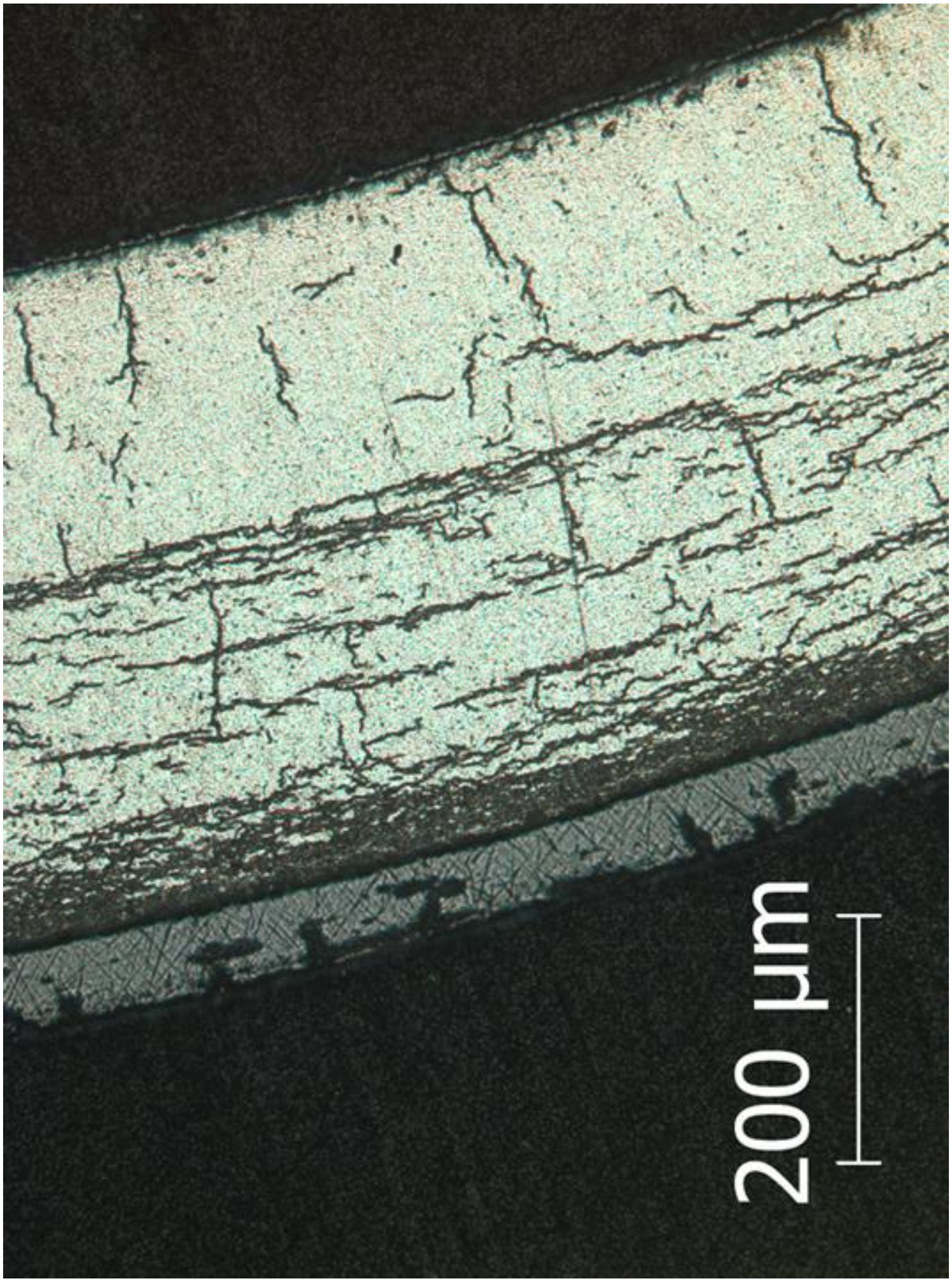

Figure A.29: Image (100X) of ZIRLO™ sample 105F6 in Area 29 from 1-cycle 350°C rodlet.

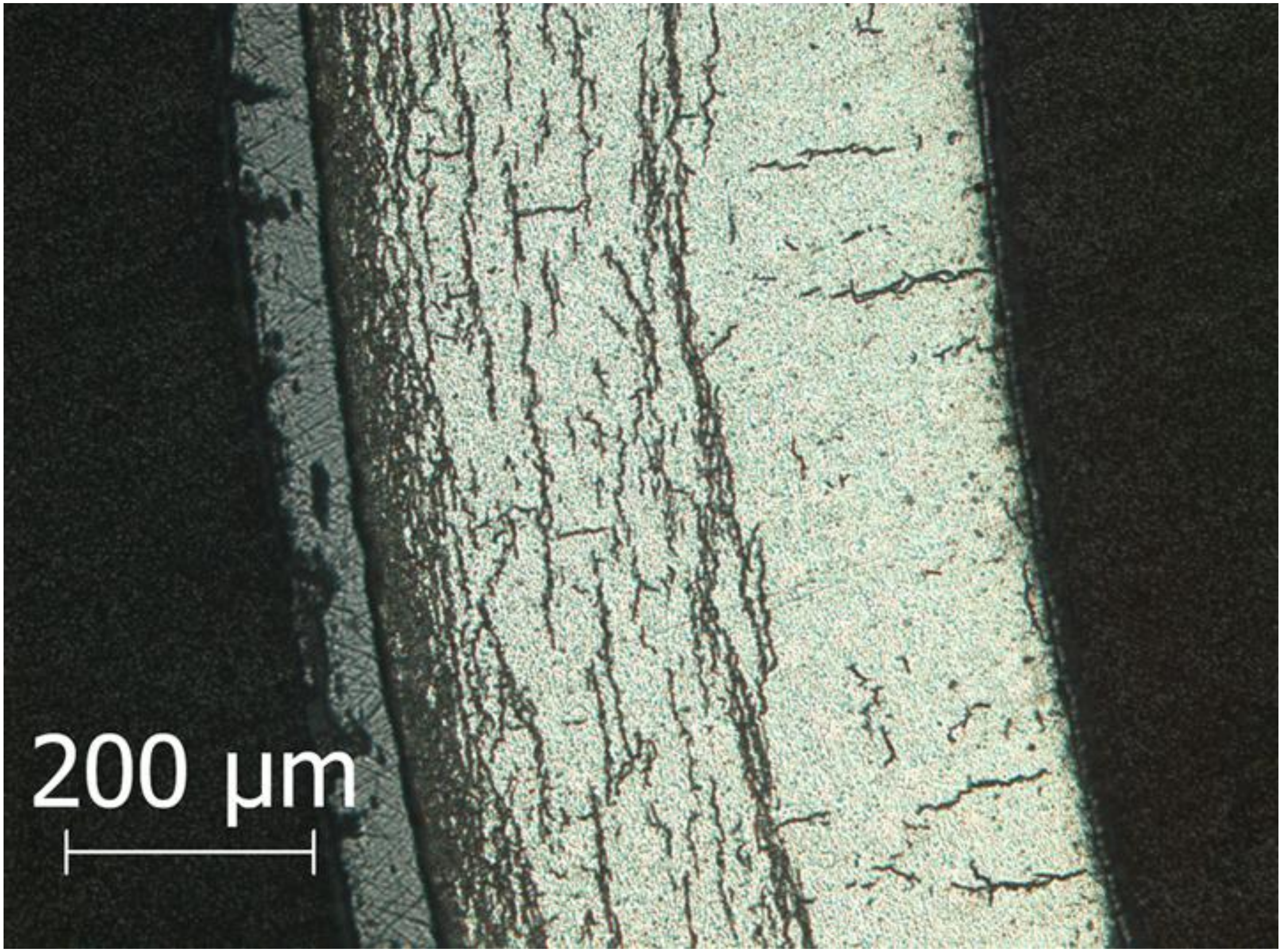

Figure A.30: Image (100X) of ZIRLO™ sample 105F6 in Area 30 from 1-cycle 350°C rodlet.

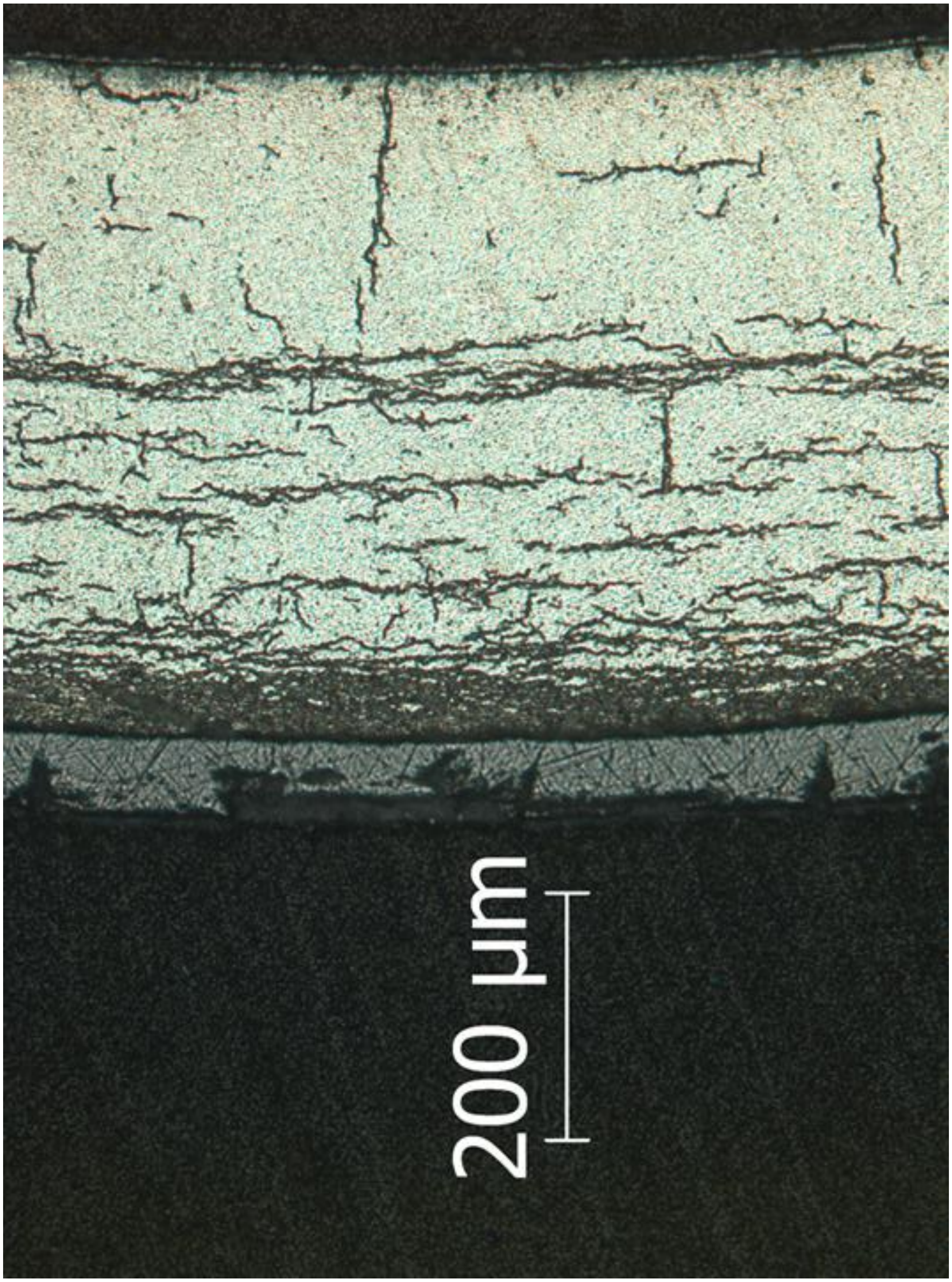

Figure A.31: Image (100X) of ZIRLO™ sample 105F6 in Area 31 from 1-cycle 350°C rodlet.

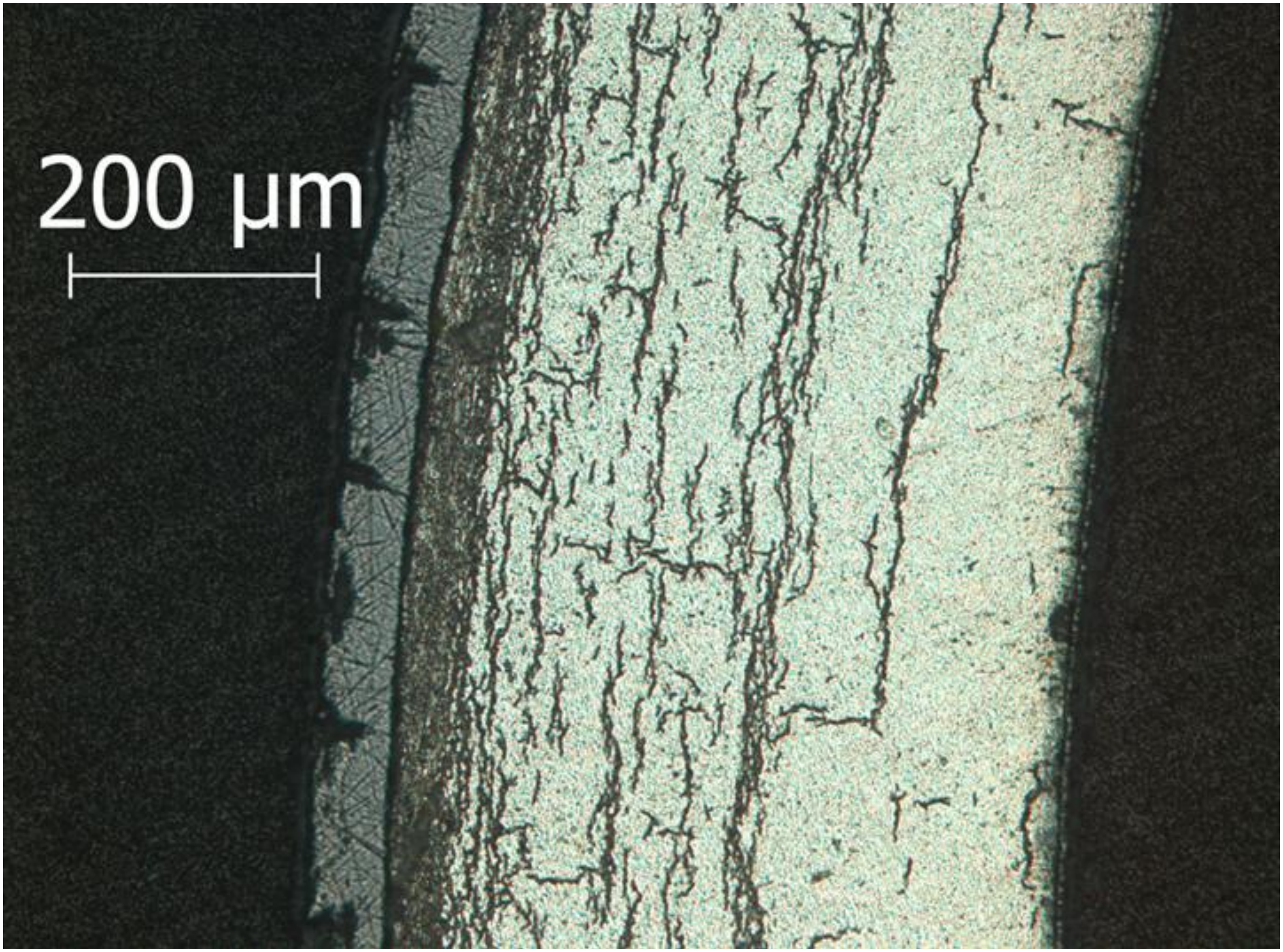

Figure A.32: Image (100X) of ZIRLO™ sample 105F6 in Area 32 from 1-cycle 350°C rodlet.

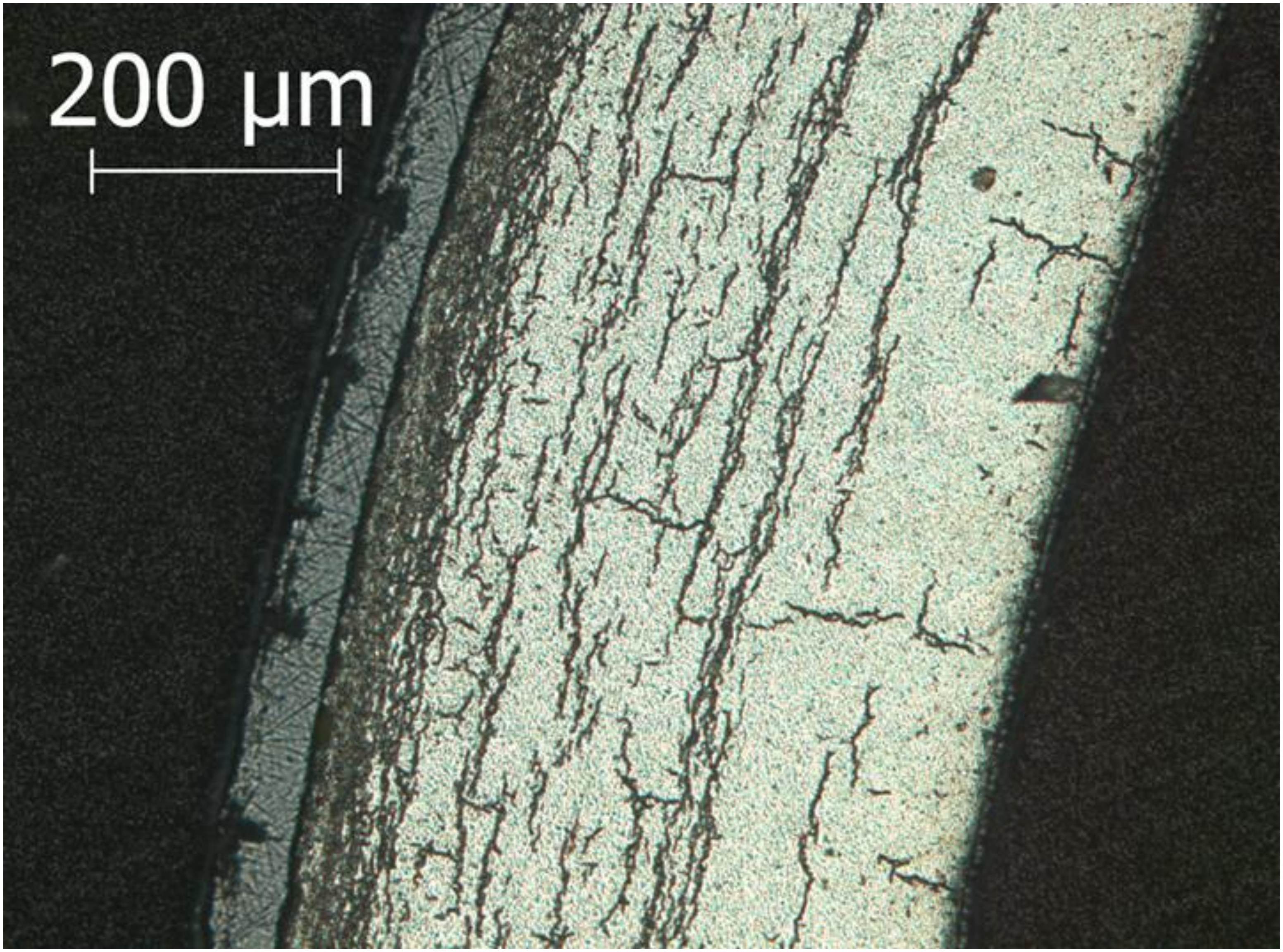

Figure A.33: Image (100X) of ZIRLO™ sample 105F6 in Area 33 from 1-cycle 350°C rodlet.

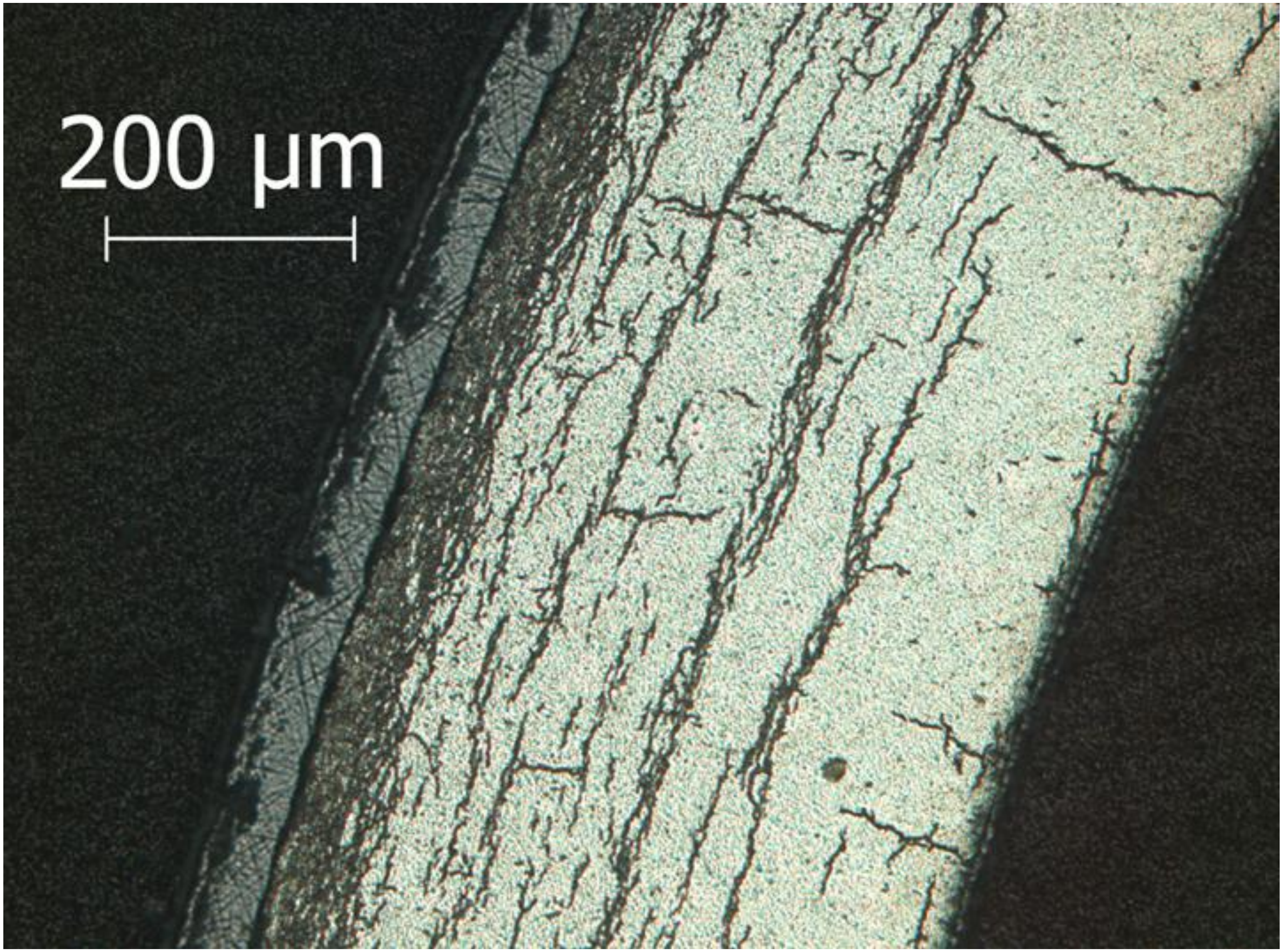

Figure A.34: Image (100X) of ZIRLO™ sample 105F6 in Area from 1-cycle 350°C rodlet.

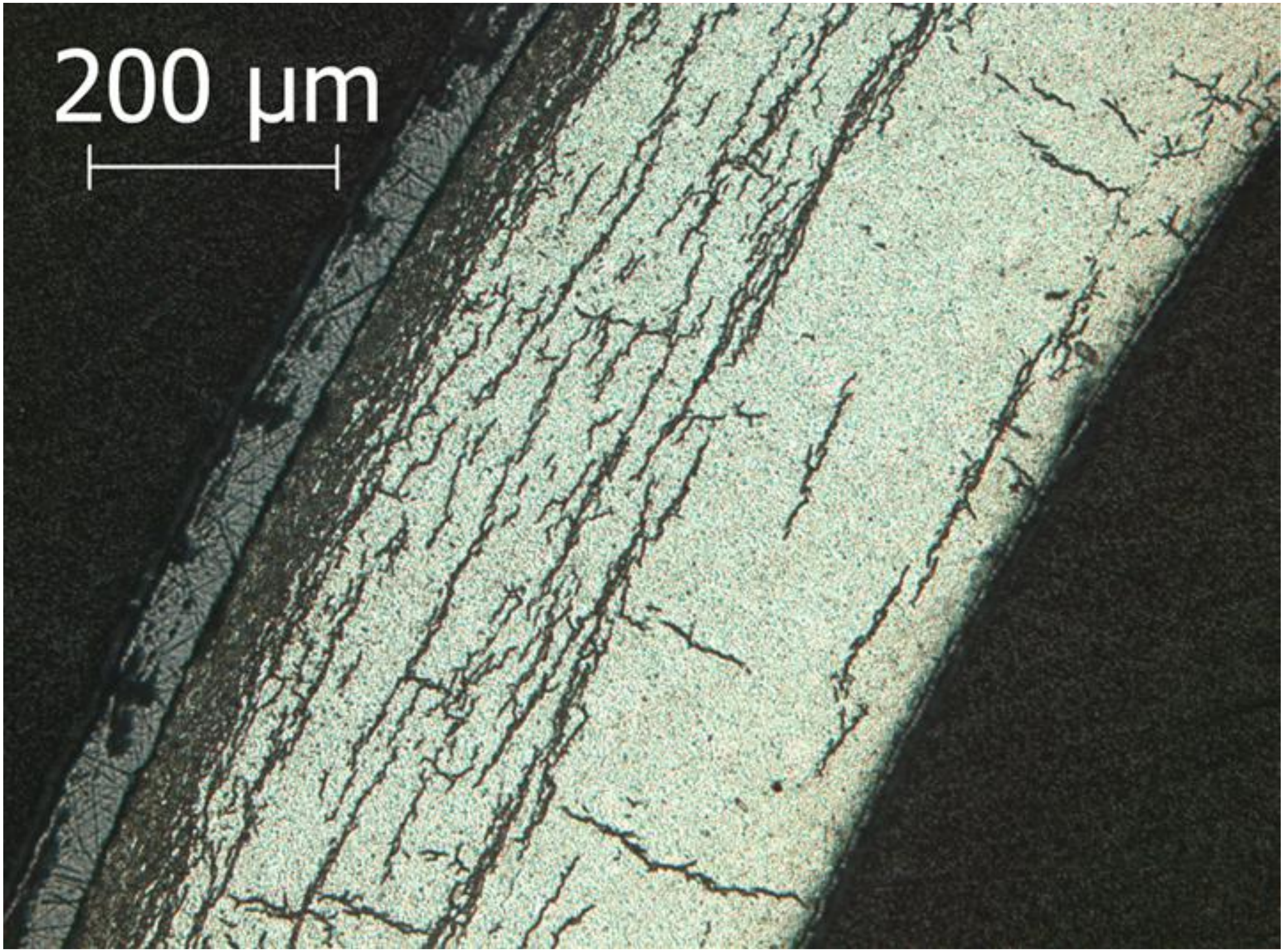

Figure A.35: Image (100X) of ZIRLO™ sample 105F6 in Area 35 from 1-cycle 350°C rodlet.

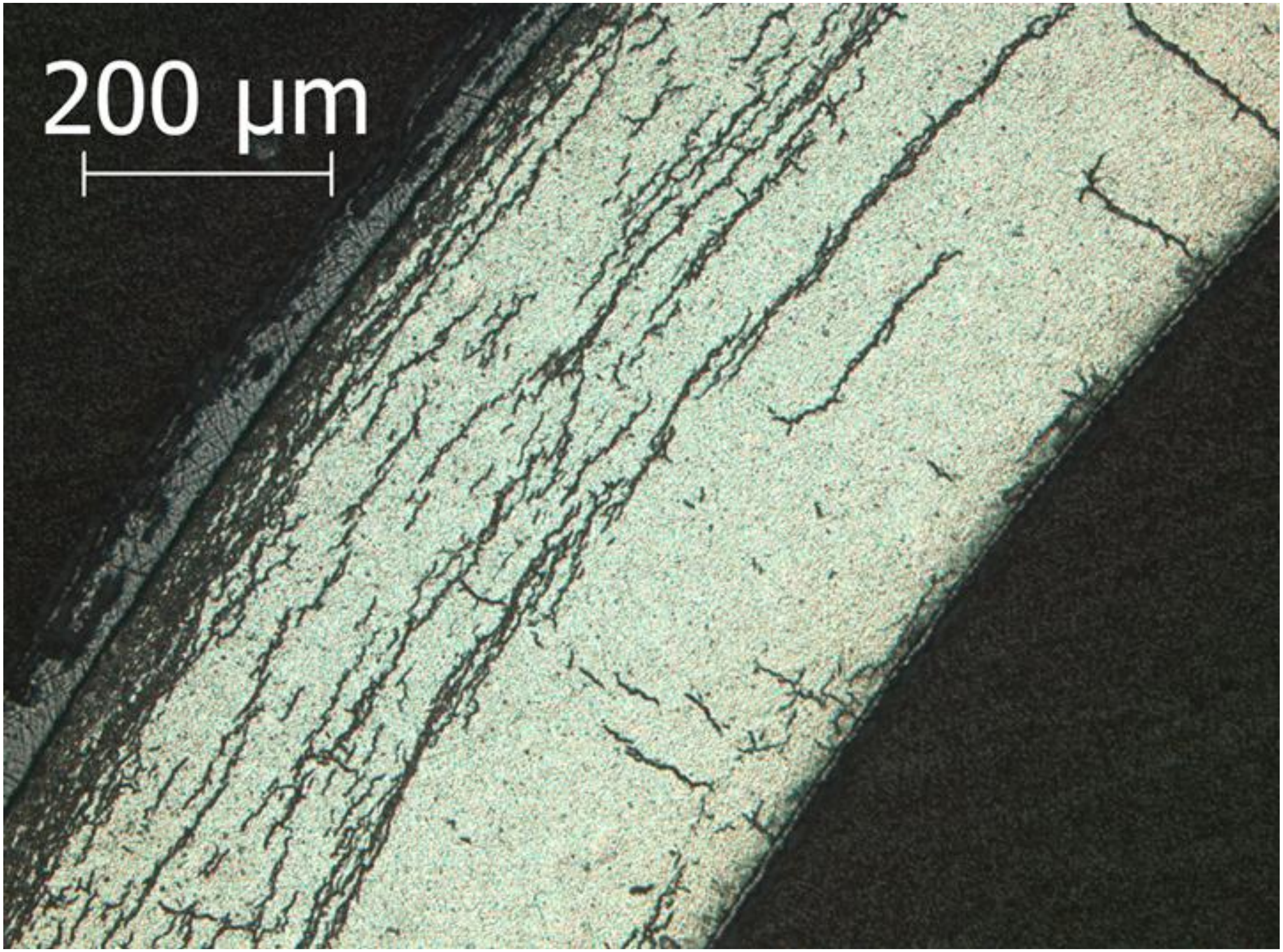

Figure A.36: Image (100X) of ZIRLO™ sample 105F6 in Area 36 from 1-cycle 350°C rodlet.

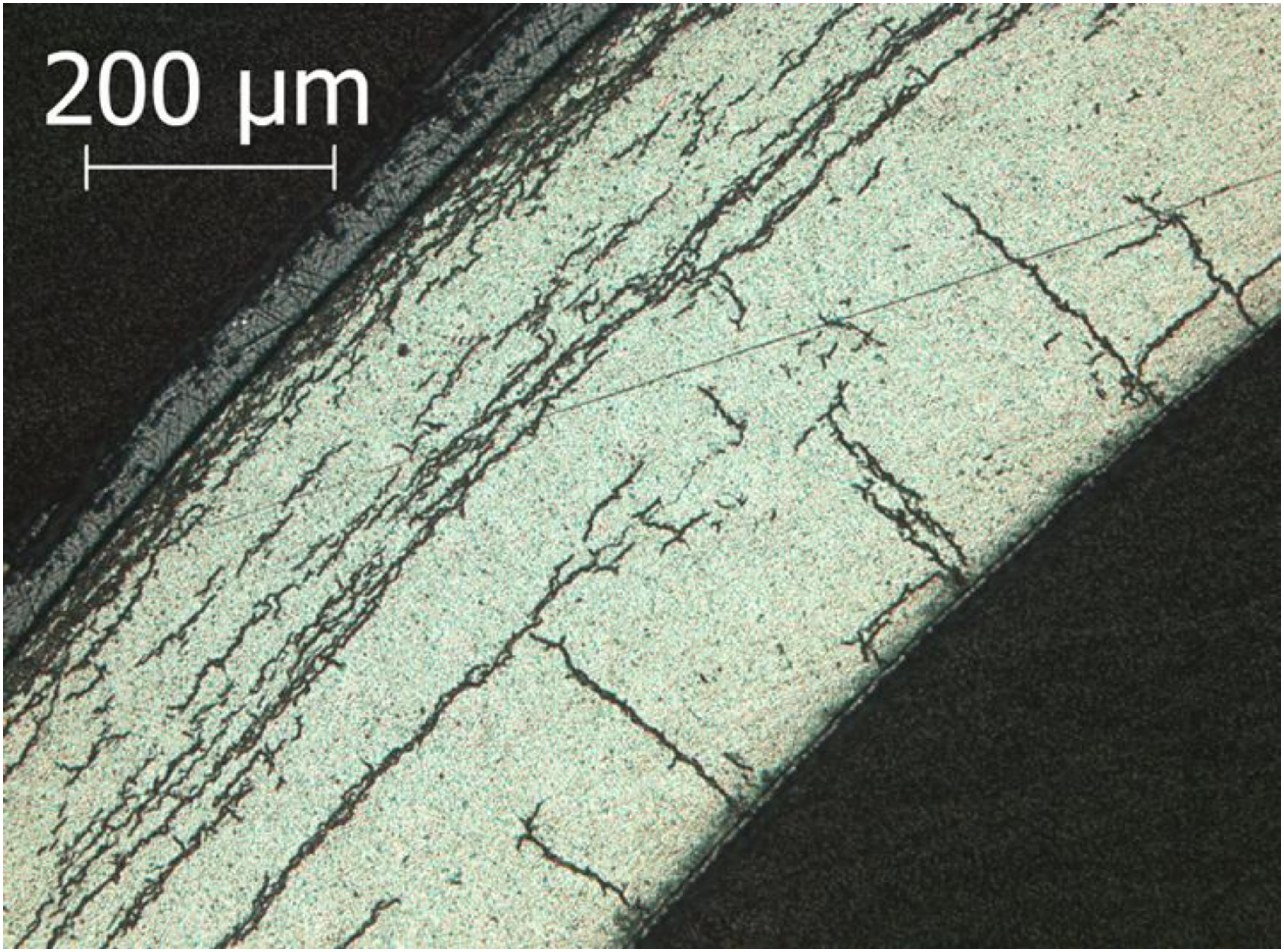

Figure A.37: Image (100X) of ZIRLO™ sample 105F6 in Area 37 from 1-cycle 350°C rodlet.

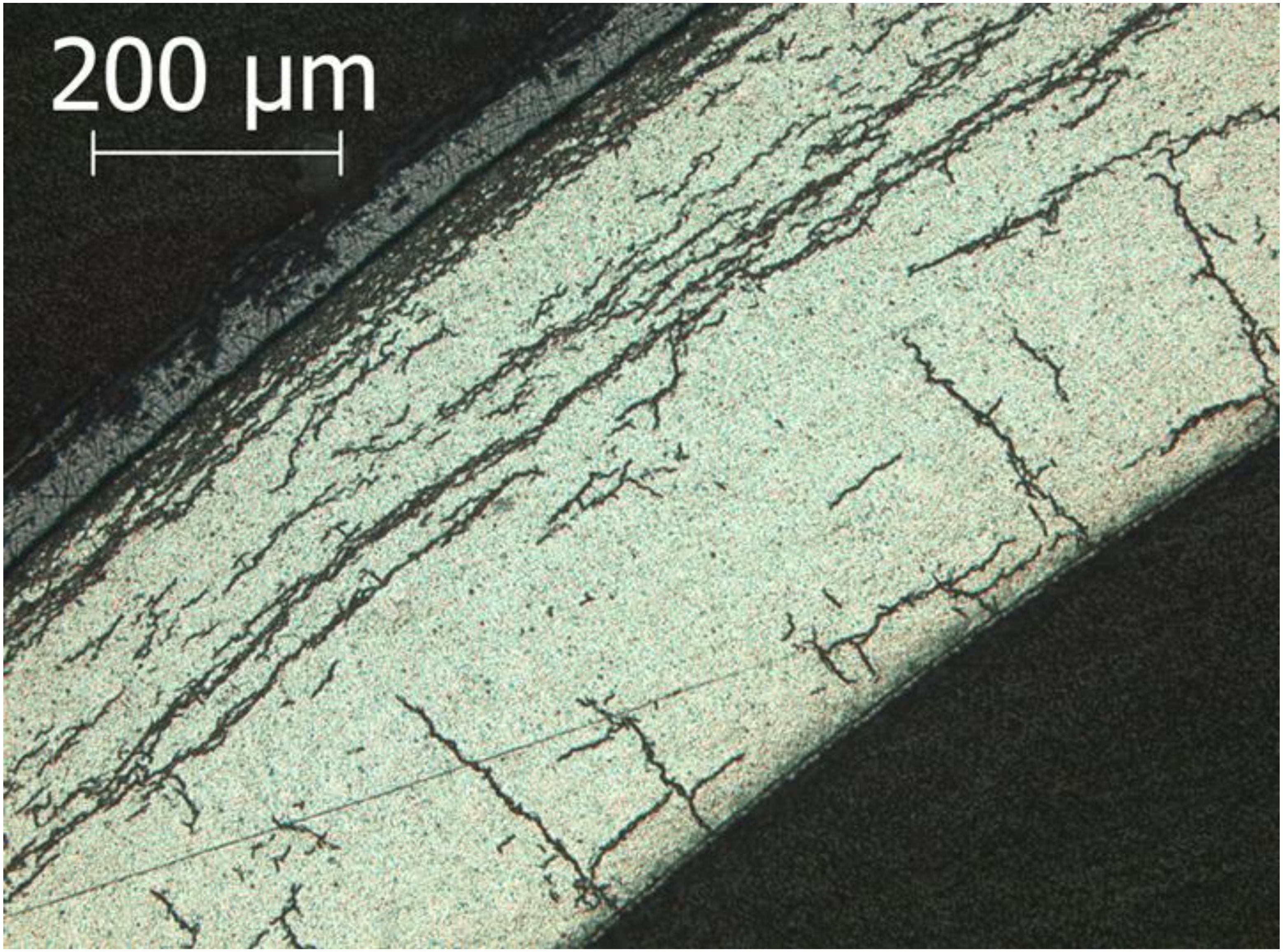

Figure A.38: Image (100X) of ZIRLO™ sample 105F6 in Area 38 from 1-cycle 350°C rodlet.

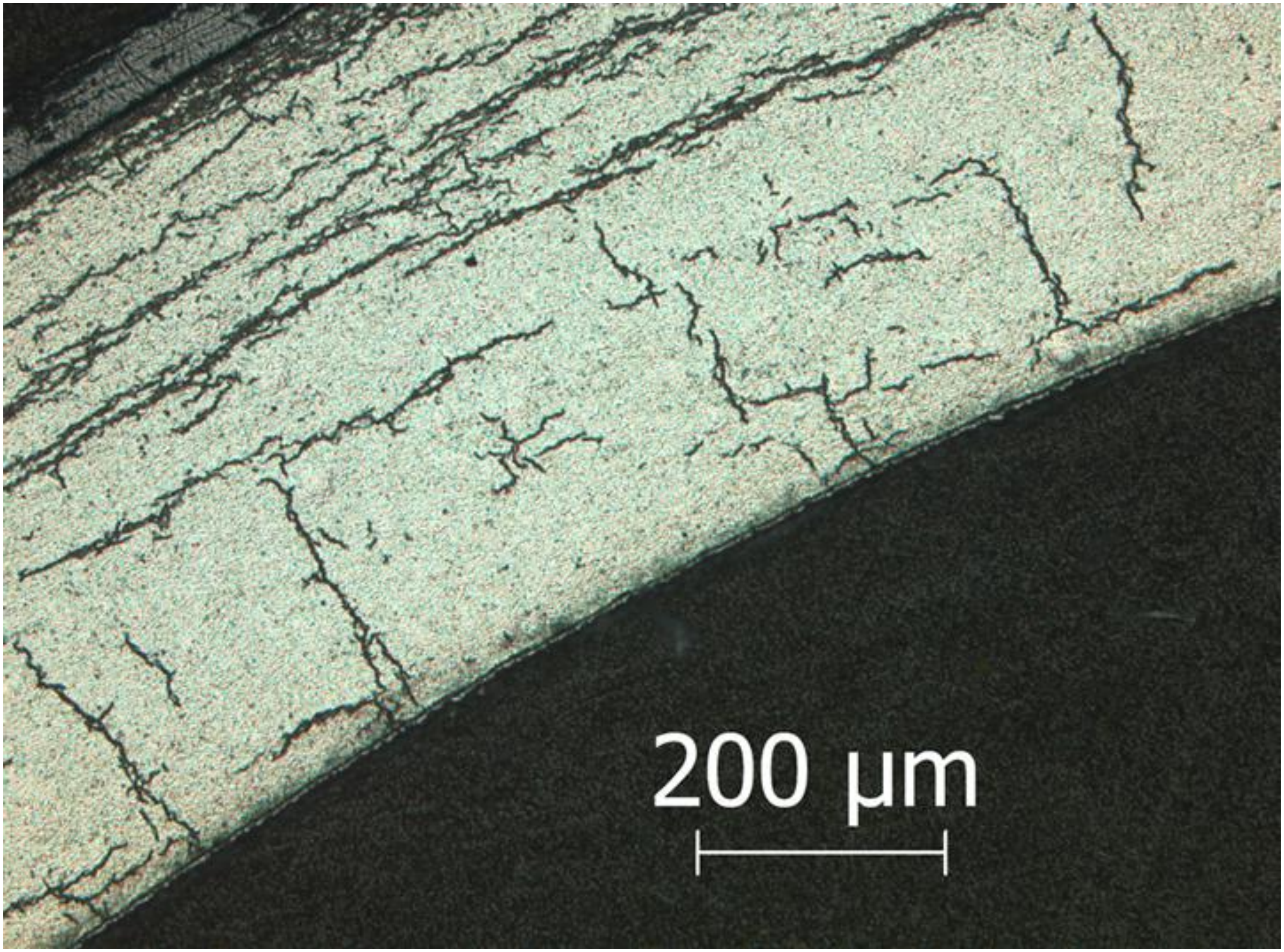

Figure A.39: Image (100X) of ZIRLO™ sample 105F6 in Area 39 from 1-cycle 350°C rodlet.

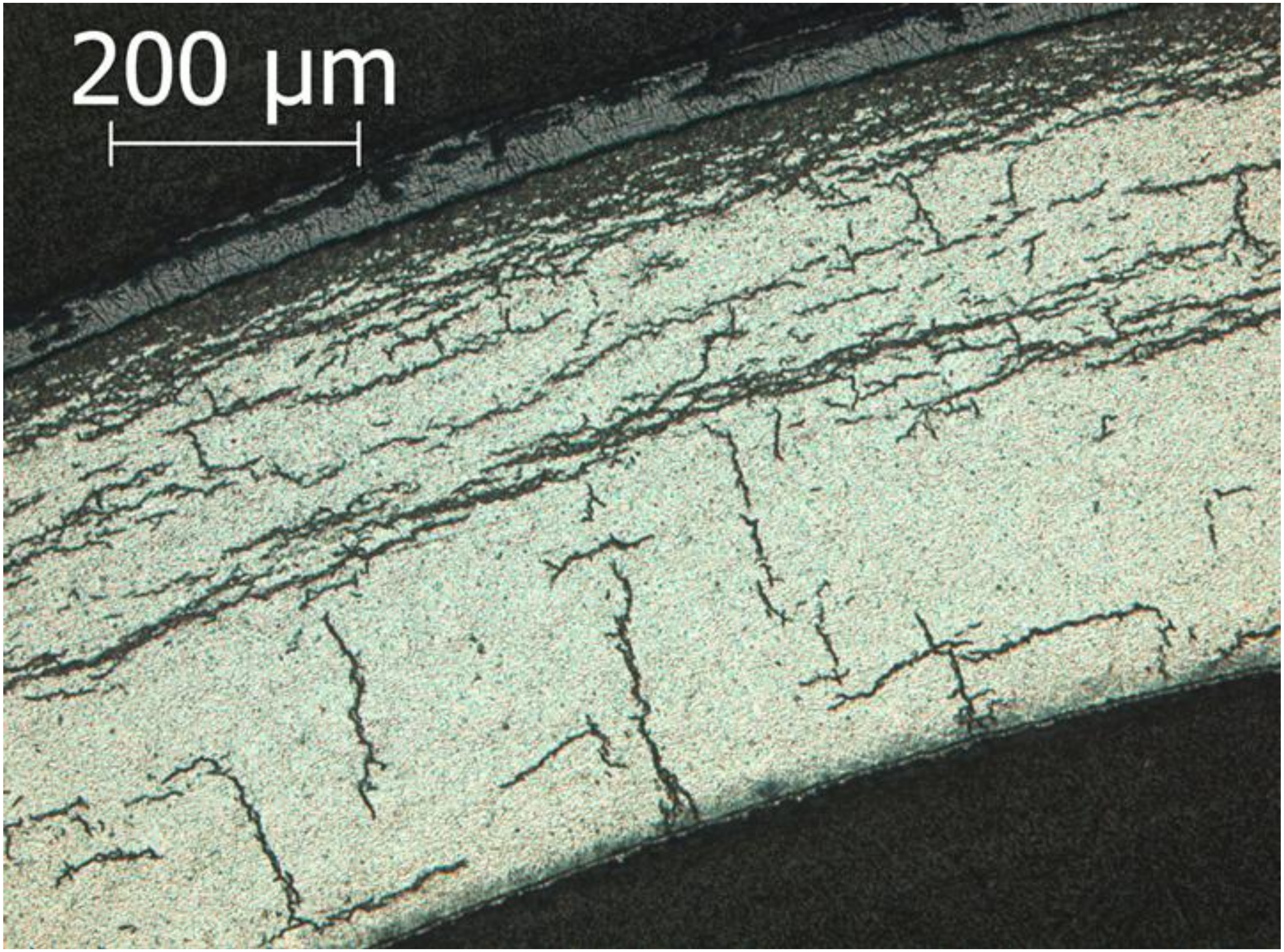

Figure A.40: Image (100X) of ZIRLO™ sample 105F6 in Area 40 from 1-cycle 350°C rodlet.

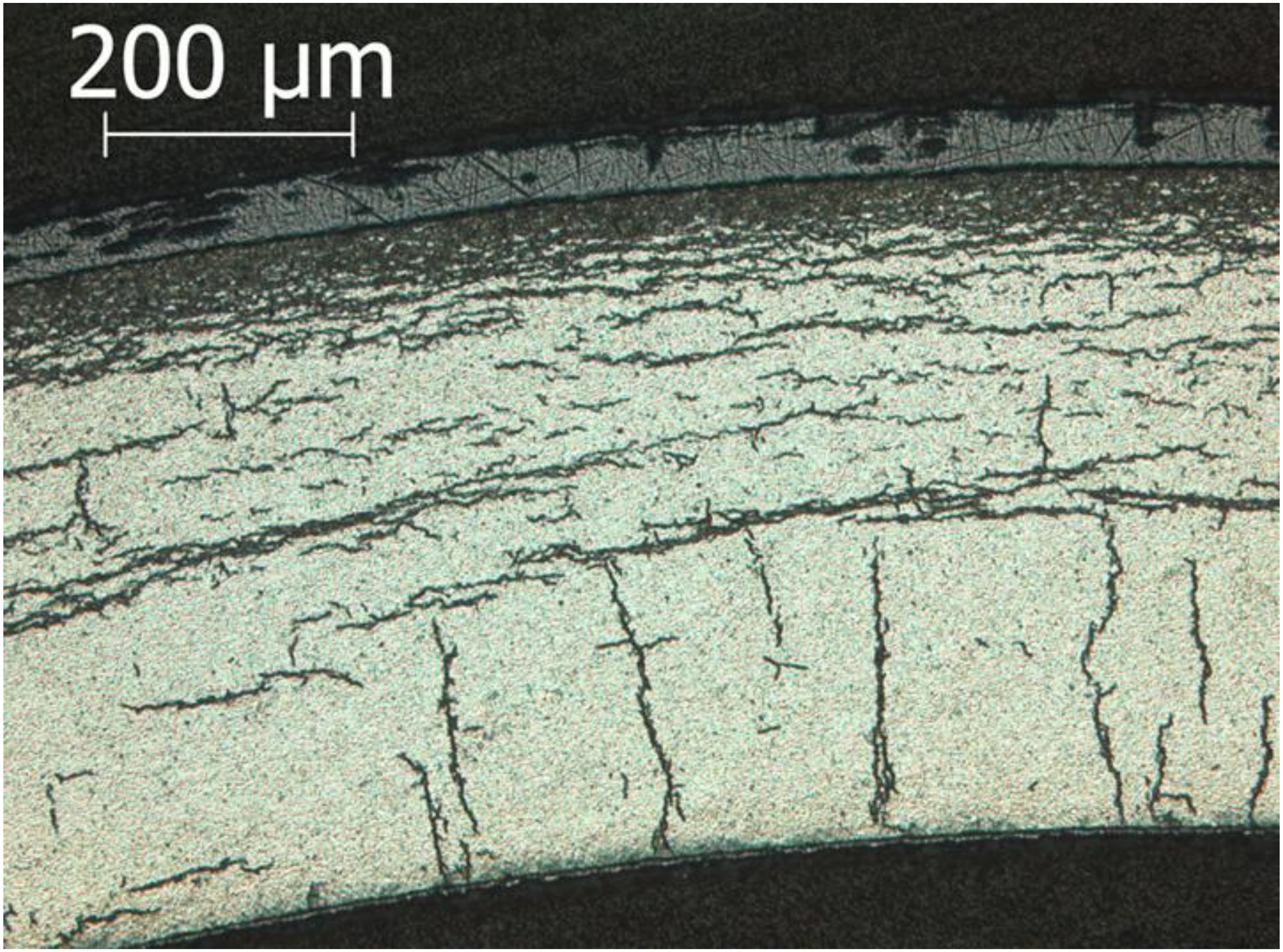

Figure A.41: Image (100X) of ZIRLO™ sample 105F6 in Area 41 from 1-cycle 350°C rodlet.

Page intentionally blank